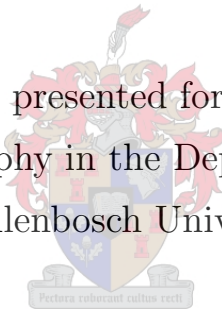


Multiple chiral bands in ^{193}Tl

Joram Ndayishimye

Dissertation presented for the degree of
Doctor of Philosophy in the Department of Physics
Stellenbosch University



Promotor: Prof. Shaun M. Wyngaardt

Co-promotor: Dr. Elena A. Lawrie

March, 2016

Declaration

By submitting this thesis electronically, I declare that the entirety of the work contained therein is my own, original work, that I am the sole author thereof (save to the extent explicitly otherwise stated), that reproduction and publication thereof by Stellenbosch University will not infringe any third party rights and that I have not previously in its entirety or in part submitted it for obtaining any qualification.

Joram Ndayishimye

March, 2016

Abstract

In order to extend knowledge about chirality in $A \sim 190$ mass region, experiments were performed at iThemba LABS for γ -spectroscopy studies in $^{192,193}\text{Tl}$. Previous level scheme of ^{193}Tl was considerably modified and extended. Level scheme of ^{192}Tl was also significantly extended. Spins and parities were assigned to most of the levels. The yrast band in ^{192}Tl is associated with $\pi h_{9/2} \otimes \nu i_{13/2}$ configuration which is suitable for chiral symmetry. A side band with close excitation energies was observed, suggesting that the two bands in ^{192}Tl might form a chiral pair. More interestingly three bands in ^{193}Tl have similar properties and were associated with the same $\pi h_{9/2} \otimes \nu i_{13/2}^2$. These bands might represent a multiplet of chiral bands in ^{193}Tl . Theoretical calculations using the Cranked Nilsson-Strutinsky (CNS) model, the multi-particle rotor (MPR) model, and the two-quasiparticle-plus-triaxial rotor model (TQPRM) support the presence of chiral symmetry in $^{192,193}\text{Tl}$.

Opsomming

Ten einde kennis oor chiraliteit in die ~ 190 massa streek in te win, was eksperimente uitgevoer by iThemba LABS vir γ -spektroskopie studies in $^{192,193}\text{Tl}$. Die vorige vlak skema van ^{193}Tl was aansienlik verander en uitgebrei. Die vlak skema van ^{192}Tl was ook aansienlik uitgebrei. Spin en pariteit was toegeken aan die meeste van die vlakke. Die yrast band in ^{192}Tl word geassosieer met die $\pi h_{9/2} \otimes \nu i_{13/2}$ konfigurasie wat geskik is vir chirale simmetrie. Sy band met noue opwekkings energie is waargeneem, wat aanduiding gee dat die twee bands in ^{192}Tl dalk 'n chirale paar vorm. Meer interessant is dat die drie bande in ^{193}Tl soortgelyke eienskappe het en was geassosieer met die dieselfde $\pi h_{9/2} \otimes \nu i_{13/2}^2$ konfigurasie, wat geskik is vir chiraliteit. Hierdie bande mag dalk 'n multiplet van chirale bande in ^{193}Tl verteenwoordig. Teoretiese berekeninge met behulp van die "Cranked Nilsson-Strutinsky (CNS)" model, die multi-deeltjie rotor (MPR) model en die twee-quasideeltjie-plus-triakiaale rotor model (TQPRM) ondersteun die teenwoordigheid van chirale simmetrie in $^{192,193}\text{Tl}$.

Acknowledgments

I would like to thank the following people and institutions for the role they played in making this thesis possible:

Prof. S. M. Wyngaardt for his support, helpful discussions, suggestions and kind encouragement.

Dr. E. A. Lawrie for her unvaluable guidance, suggestions, support and being patient with me during this PhD project.

Mr. J. Easton for his enthusiastic assistance in the experimental setup, the data collection and sorting.

Dr. O. Shirinda for his indispensable discussions and support in my calculations.

My wife Mrs S. Antetere for her special assistance, patience and encouragement to overcome challenges.

All postgraduate students and staff members of iThemba LABS for a friendly atmosphere and their support in different ways.

iThemba LABS, Rwanda Education Board (REB), NRF and Stellenbosch University for financial support.

I am very grateful for any kind of support from different people, may God bless you all.

Contents

1	Introduction	1
1.1	Chirality in nuclei	1
1.1.1	Historical point of view	1
1.1.2	Definition	1
1.1.3	Theoretical fingerprints of chirality in nuclei	2
1.1.4	Suggested chiral candidates in nuclei	3
1.2	Motivation of this study	5
1.3	Outline of thesis	6
2	Model description of nuclear structure	7
2.1	Introduction	7
2.2	Nuclear surface deformations	7
2.3	Shell model	11
2.4	Nilsson Model	13
2.4.1	Nilsson diagrams	14
2.5	Collective Models	15

2.5.1	Nuclear rotations	15
2.5.2	Nuclear Vibrations	18
2.5.3	Collective rotation in the body-fixed frame: Cranked Shell Model (CSM)	18
2.5.4	Calculation of potential energy surface applicable to experimental data	23
2.5.5	Particle-Rotor Model	24
2.5.6	Multi-particle rotor (MPR) model	26
3	Experimental techniques and tools	29
3.1	Nuclear reaction	29
3.2	Interaction of gamma rays with matter	32
3.2.1	Photoelectric effect	32
3.2.2	Compton scattering	34
3.2.3	Pair production	35
3.3	Detection and measurements of γ -rays	38
3.3.1	Semiconductor detectors	38
3.4	High purity germanium (HPGe) clover detectors	39
3.4.1	Compton suppression	41
3.4.2	Absorbers	43
3.4.3	HPGe detector arrays	44
3.5	AFRODITE array	45
3.6	Basic ideas of electronics	47

3.6.1	Analog electronics	48
3.6.2	Digital electronics	49
3.6.3	Threshold and pole zero adjustment	52
3.6.4	Time window and trigger condition	52
3.7	Data analysis procedures	53
3.7.1	Set of programs for data analysis	53
3.7.2	Energy calibration and gain matching	53
3.7.3	Doppler shift correction	54
3.7.4	Gain drift correction of the energies	55
3.7.5	HPGe clovers and add-back procedure	55
3.7.6	$\gamma - \gamma$ matrix construction	56
3.7.7	Gating	56
3.7.8	Spin and parity measurements	58
3.7.9	Measurement of γ -ray relative intensities	62
3.7.10	Identification of isomers using the Recoil Shadow Anisotropy Method (RSAM)	63
4	Experimental details, results and discussion	68
4.1	Introduction	68
4.2	Experimental details	68
4.3	Experimental results	70
4.3.1	Level scheme of ^{193}Tl	70

4.4	Rotational bands and other structures of ^{193}Tl	76
4.4.1	Band 1	76
4.4.2	Band 2	78
4.4.3	Band 3	81
4.4.4	Band 4 and its decay paths	82
4.4.5	Band 5	89
4.4.6	Other sequences	92
4.5	^{192}Tl Level scheme	92
4.6	^{192}Tl bands and spectra	96
4.6.1	Band 1	96
4.6.2	Band 2	97
4.6.3	Band 3	99
4.6.4	Band 4	99
4.6.5	Band 5	99
4.7	Discussion	105
4.7.1	Nucleon configurations of ^{193}Tl	106
4.7.2	Nucleon configurations of ^{192}Tl	111
4.8	Possible multiplet of chiral bands in ^{193}Tl	114
4.9	Chiral symmetry in ^{192}Tl	122
5	Conclusions	127

List of Tables

3.1	Description details for abbreviations used in Fig. 3.13	46
4.1	List of the energies, total γ -ray intensities, angular distribution ratios, linear polarization anisotropy, γ -ray intensities, energy of the initial levels and corresponding assignments for γ -transitions in ^{193}Tl	72
4.2	Measured total intensities for the transitions below the $25/2^-$ state measured in a spectrum gated on the 269.0 keV transition. The star sign (*) labels the multipolarity of the 96.0 keV γ -ray that was deduced.	81
4.3	Illustration of the analysis of the total intensities showing that the 107.8 keV and the 47.5 keV transitions are stretched electric dipoles. The star signs (*) labels the multipolarities that were deduced.	86
4.4	Some energy transitions from the coincidence spectra gated on 161.7, 316.8 and 125.9 keV and the corresponding percentage of the RSAM anisotropy parameter A denoted respectively by $A_{g161.8}$, $A_{g316.7}$ and $A_{g125.9}$. A_{av} shows the weighted average for the obtained A values for each transition. The star sign (*) labels the A values for transitions below the $17/2^+$ state.	87
4.5	List of the energies, total intensities, R_{AD} ratios, linear polarization anisotropies, γ -ray intensities, energies of the initial levels and corresponding assignments for γ -transitions in ^{192}Tl	94

List of Figures

1.1	Illustration of the nuclear chiral symmetry with left and right-handed systems for a triaxially deformed odd-odd nucleus. The symbols \vec{J} , \vec{R} , \vec{j}_ν , and \vec{j}_π denote respectively the total angular momentum, the angular momenta of rotor, neutron, and proton.	2
2.1	Diagram representation of the nuclear shape in β_2 and γ plane with $\lambda = 2$. Figure taken from [82].	10
2.2	Plot illustrating a comparison between one-dimensional harmonic oscillator potential, square well potential and Woods-Saxon potential.	12
2.3	Plots of the energy levels for neutrons ($82 \leq N \leq 126$) as a function of ε_2 ($\varepsilon_4 = \varepsilon_2^2/6$) in a prolate ($\varepsilon_2 > 0$) and oblate ($\varepsilon_2 < 0$) nucleus. The quantum numbers $\Omega(Nn_zm_l)$ label the states. Solid and dashed lines indicate the states with positive and negative parity respectively [83,84].	16
2.4	Plots of the energy levels for protons ($50 \leq P \leq 82$) as a function of ε_2 ($\varepsilon_4 = \varepsilon_2^2/6$) in a prolate ($\varepsilon_2 > 0$) and oblate ($\varepsilon_2 < 0$) nucleus. The quantum numbers $\Omega(Nn_zm_l)$ label the states. Solid and dashed lines indicate the states with positive and negative parity respectively [83,84].	17
2.5	Diagram showing the lowest three vibrational modes of a nucleus.	19
2.6	Schematic illustration of the deformation alignment (top panel) and rotation alignment (bottom panel).	27

3.1	Schematic illustration of heavy-ion fusion evaporation reaction showing consecutive phases up to the ground state of the residual nucleus [99].	30
3.2	Schematic illustration of the excitation energy states as a function of the nuclear spin (angular momentum) I for heavy-ion induced fusion evaporation reaction.	31
3.3	Plot for the $^{181}\text{Ta}(^{18}\text{O}, xn)$ reaction cross-section as calculated with the PACE program. A large cross-section from $^{181}\text{Ta}(^{18}\text{O}, 6n)$ to study ^{193}Tl could be obtained using the beam energy of $E_{lab} = 105$ MeV.	33
3.4	Schematic illustration of photoelectric effect.	34
3.5	Schematic illustration of Compton scattering.	35
3.6	Schematic illustration of pair production.	36
3.7	Plot of γ -ray cross-sections for germanium. The Compton scattering covers a wide range of energies. The photoelectric effect takes place mainly at low energies [103].	37
3.8	Diagram showing different bands of a Ge semiconductor.	39
3.9	Illustration of the depletion region.	40
3.10	Schematic representation of a clover germanium detector. Figure taken from [106] and modified.	42
3.11	Diagram showing a BGO shield around a clover germanium detector [108].	43
3.12	Schematic illustration of the experimental facilities at iThemba LABS [111].	45
3.13	AFRODITE array with HPGe clover detectors and LEPS.	47
3.14	Illustration of the pulse splitting using the CFD [114].	48
3.15	Illustration of the fast trapezoidal filter for arrival time (bottom panel) and the slow trapezoidal filter for the γ -ray energy (top panel). Modified figure that was taken from [115].	51

3.16 Schematic representation of the detector opening angle and the recoil velocity causing the Doppler broadening of the detected γ -rays. Figure taken from [58].	55
3.17 Plot of γ - γ matrix illustrating the coincidence events on X and Y-axis. Dots illustrate counts being incremented on Z-axis [119].	57
3.18 Example of a simple level scheme.	58
3.19 Plot illustrating the angular distribution function $W(\theta)$ as a function of the angle θ for $I \rightarrow I - 1$ dipole transition (solid line) and $I \rightarrow I - 2$ quadrupole transition (dashed line). $\theta = 0^\circ$ corresponds to the positive x-axis. Figure taken from [58].	60
3.20 Compton scattering in a clover detector for stretched electric (left panel) and magnetic (right panel) dipole transition.	61
3.21 Schematic illustration of the intensity measurement with normalization correction. Intensity is measured from above at the gate on the energy transition E_g	63
3.22 Plot of the detector efficiency of the AFRODITE array as a function of energy obtained with ^{152}Eu and ^{133}Ba sources in our experiment.	64
3.23 Schematic illustration of geometry of the AFRODITE clover detectors showing collimator shadow effect on the detectors located at 85° and 135° for the delayed transition.	66
3.24 Calibration anisotropy curve and the experimental data for the 12^+ (3.5 ns) and 7^- (5.25 ns) isomers in ^{196}Hg from Ref. [125].	67
4.1 Total level scheme of ^{193}Tl as constructed in this work.	71
4.2 Spectra gated on 716.4 and 791.0 keV transitions. The star signs (*) show the transitions placed in Band 1. The new linking transitions to Band 2 are labeled with +.	77

4.3	Spectra illustrating the coincidence relationships of the transitions in Band 2. Peaks that belong to Band 2 are marked with \$. The spectrum in the insert is gated on 477.0 keV and shows that the 477.0 keV transition is in coincidence with the 478.0 keV γ -ray.	79
4.4	Illustration of the coincidence data for Band 2. Gate on 672.5 keV shows the transitions marked with * that belong to Band 2, including the new low-energy transitions 85.0 and 96.0 keV. The transitions labeled with & in the 735.9 keV gate were placed in Band 4.	80
4.5	Gates on 810.9 and 369.0 keV illustrating the coincidence data for Band 3. The two linking transitions are visible in the 369.0 keV gated spectrum and are marked with *. The same gate shows that 369.0 keV is a doublet and the two members are in coincidence. The dollar sign (\$) labels the transitions that were placed in Band 3. Transitions marked with @ belong to ^{194}Tl . . .	83
4.6	Spectra gated on the 125.9, 696.8 and 47.5 keV transitions respectively. The transitions placed in Band 4 are marked with *. The low energy transition (47.5 [keV]) is marked with #.	85
4.7	Spectra showing the transitions as placed in Band 4. The \$ sign shows that the 97.0 keV transition is also in coincidence with the 406.6 keV transition. The plus sign (+) in the insert at the top shows the change of placement for the 478.5 keV transition since it is in coincidence with the 316.7 keV ($27/2^+ \rightarrow 25/2^+$) transition. The 316.7 keV peak is marked with # as it appears twice and is in anti-coincidence with the 633.4 keV transition. The other transitions placed in Band 4 are marked with *.	88
4.8	Spectra gated on the 866.0 and 929.0 keV transitions illustrating the coincidence relationships in Band 5. The star sign (*) labels the transitions that were placed in Band 5.	90
4.9	Illustration of the coincidence data in Band 5. The star sign (*) labels the transitions placed in this band. The three linking transitions are visible in the spectrum gated on 238.5 keV.	91

4.10	The level scheme of ^{192}Tl , built in the present work.	93
4.11	Illustration of the transitions placed in Band 1 of ^{192}Tl . The star sign (*) labels the transitions belonging to ^{192}Tl , while & corresponds to some transitions of ^{193}Tl . The 538.3 keV cross-over of 262.0 keV and 276.3 keV appears strongly in the 458.2 keV gate but is not seen in the 276.3 keV gate. Similarly the 766.9 keV and 773.2 keV peaks are visible in the 276.3 keV gate, but disappear in the 458.2 keV gate, since they are placed in parallel to the 458.2 keV transition.	98
4.12	Partial decay scheme of the yrast bands in ^{190}Tl [129], ^{194}Tl [58], ^{196}Tl [130] and ^{198}Tl [131]. The plot at the bottom right illustrates the systematics of the energies of the dipole transitions in the yrast bands in the odd-odd $^{190-198}\text{Tl}$ isotopes.	100
4.13	Coincidence spectra for Band 2 of ^{192}Tl level scheme. All transitions marked with a star sign (*) were placed in this band. One observes an enhancement of the 296.7 keV peak in the 145.0 keV gate compared to the 296.6 keV gate since the doublet (296.6 and 296.7 keV) is in coincidence with the 145.0 keV transition while the 296.7 keV gate sees only the 296.6 keV transition. The transitions placed in the group of levels below the 11^- state are also visible in both gates.	101
4.14	Gated spectra illustrating transitions placed in Band 3 of ^{192}Tl . The dollar sign (\$) labels the transitions placed in Band 3. Transitions marked with # are in coincidence with Band 3 and are placed below the 13^- level. Transitions marked with & belong to ^{193}Tl	102
4.15	Gated spectra showing transitions of Band 4 in ^{192}Tl . The star sign (*) labels the transitions placed in this band, while the dollar sign (\$) marks transitions placed in Band 1. One observes that the 123.2 keV peak is seen in the 949.2 keV gate but disappears in the 773.2 keV gate. Similarly, the observed 299.2 keV peak in the 773.2 keV gate is not visible in the 949.2 keV gate.	103

4.16	Illustration of the transitions placed in Band 5 of ^{192}Tl . The star sign (*) labels the transitions placed in Band 5. Transitions marked with # are placed in Band 1. Since the 221.5 keV is a doublet, the dollar sign (\$) labels the transitions in coincidence with 221.0 keV that was placed in Band 4. Transitions labelled with & belong to ^{193}Tl	104
4.17	Alignments of Bands 2, 3 and 5 built on the $\pi h_{9/2} \otimes \nu i_{13/2}^2$ configuration in ^{193}Tl compared with those of the $\nu i_{13/2}^2$ band in the ^{192}Hg isotone and the $\pi h_{9/2}$ band in ^{193}Tl . Harris parameters of $J_0 = 8\hbar^2/\text{MeV}$ and $J_1 = 40\hbar^4/\text{MeV}^3$ were used. The dashed blue line indicates the alignment of the $\nu i_{13/2}^2$ band in ^{192}Hg increased by $2.1 \hbar$, a value that corresponds to the approximate alignment of the odd $h_{9/2}$ proton.	107
4.18	Experimental excitation energies of Band 2, 3 and 5 in ^{193}Tl	109
4.19	Experimentally measured $B(M1)/B(E2)$ reduced transition probability ratios for Band 2, 3 and 5 in ^{193}Tl	110
4.20	Alignments of Bands 1 and 5 built on the $\pi h_{9/2} \otimes \nu i_{13/2}$ configuration in ^{192}Tl compared with those of the $\nu i_{13/2}$ band in the ^{191}Hg isotone and the $\pi h_{9/2}$ band in ^{193}Tl . Harris parameters of $J_0 = 8\hbar^2/\text{MeV}$ and $J_1 = 40\hbar^4/\text{MeV}^3$ were used. The dashed blue line indicates the alignment of the $\nu i_{13/2}$ band in ^{191}Hg increased by $2.1 \hbar$, a value that corresponds to the approximate alignment of the odd $h_{9/2}$ proton.	112
4.21	Experimental excitation energies of Band 1 and 5 in ^{192}Tl	113
4.22	Partial level scheme of ^{193}Tl showing the three bands with close-similarity.	116
4.23	Potential energy surfaces for the negative parity bands ^{193}Tl as a function of the nuclear deformation for three different values of the spin.	117
4.24	Experimental (left panel) and theoretical (right panel) excitation energies in ^{193}Tl	118

4.25	Plot of the components for the angular momenta of the core (R), the protons (p) and the neutrons (n) in ^{193}Tl as produced with calculations using the MPR model.	119
4.26	Plot of the components for the total angular momentum in ^{193}Tl as produced with calculations using the MPR model.	120
4.27	Experimental (left panel) and theoretical (right panel) $B(M1)/B(E2)$ values of ^{193}Tl	121
4.28	Potential energy surface as a function of spin in ^{192}Tl illustrating the absolute minima with respect to the nuclear deformation.	123
4.29	Experimental (left panel) and theoretical (right panel) excitation energies in ^{192}Tl	124
4.30	Plot of the components for the angular momenta of the core (R), the protons (p) and the neutrons (n) in ^{192}Tl as produced with calculations using the TQPRM.	125
4.31	Plot of the components for the total angular momentum in ^{192}Tl as produced with TQPRM calculations.	126

Chapter 1

Introduction

1.1 Chirality in nuclei

1.1.1 Historical point of view

Chiral symmetry was first defined in molecules (see [1] and references therein). It was also pointed out that this symmetry plays a key role in many aspects of life-plants and animals, and is important in many agricultural, pharmaceutical and chemical industries [1]. It was introduced in nuclear physics in 1997 [2].

1.1.2 Definition

Chirality refers to an object or a system which is not identical to its mirror image. Macroscopically, chiral symmetry exists in space and corresponds to a structural feature of the system. In the nuclear realm, it is impossible to identify chiral features with respect to the spatial matter distribution. Chirality in nuclei could be defined in angular momentum space [2]. A simple case of the nuclear chiral symmetry refers to a triaxially deformed odd-odd nucleus where the collective rotational angular momentum favours alignment along the intermediate axis, while the odd proton and odd neutron (having particle and hole nature respectively), favour alignments along the nuclear short and long axes respectively (see Fig. 1.1). For this system, the total angular momentum is aplanar, i.e. it is out of the plane defined by any two individual angular momenta. The system can be transformed

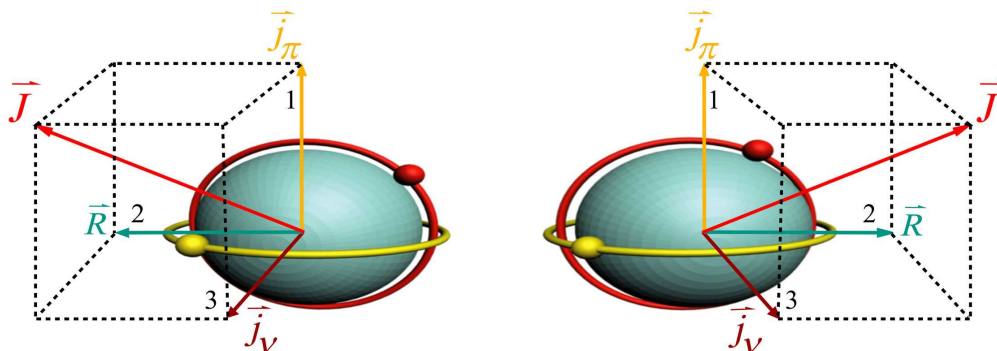


FIG. 1.1. Illustration of the nuclear chiral symmetry with left and right-handed systems for a triaxially deformed odd-odd nucleus. The symbols \vec{J} , \vec{R} , \vec{j}_ν , and \vec{j}_π denote respectively the total angular momentum, the angular momenta of rotor, neutron, and proton.

into its mirror image by a chiral operator of the form $\chi = TR(\pi)$, where $R(\pi)$ corresponds to a rotation of 180° , while T is the time reversal and therefore changes to opposite the directions of all angular momentum vectors.

In the laboratory frame, the nuclear chiral system shows two degenerate bands called chiral doublet bands. In the ideal case all measurable properties of the partner bands are degenerate. In practice chiral bands are never degenerate, but show similar properties. It was suggested that chiral symmetry could be identified if similarities between the specific bands are observed.

1.1.3 Theoretical fingerprints of chirality in nuclei

For ideal chiral symmetry all properties of chiral doublet bands such as energies, $B(M1)$ and $B(E2)$ values, moment of inertia, and alignments should be identical [2,3]. Such perfect degeneracy is not found in any of the suggested chiral candidates. Experimentally chiral pairs show close similarity, which differs from one nucleus to another. For instance the observed chiral doublet bands show a difference of up to ~ 500 keV in the excitation energy [4-36]. Calculations showed that chiral bands in real case can have a difference of excitation energy up to several hundreds keV, which is not possible for the ideal chiral symmetry. This may apply to other chiral features [37]. There are not many chiral nuclei for which lifetimes were measured and $B(M1)$ and $B(E2)$ values were extracted. A few of

the best chiral candidates to date are briefly described in the next subsection.

Apart from the similarity of the partner bands other features were suggested as fingerprints of chirality. It was proposed that the chiral pair shows a smooth dependence of the energy staggering parameter $S(I)$ with spin, where

$$S(I) = \frac{E(I) - E(I - 1)}{2I}, \quad (1.1)$$

because the particle and the hole orbital angular momenta are both perpendicular to the core rotation [38-40]. However, this is not a necessary requirement for all chiral bands [41, 42]. Indeed, an aplanar orientation of the total angular momentum is needed in order to form a chiral system [2], but the individual angular momenta of the particles and rotational core may not necessarily be orthogonal. It was pointed out that energy staggering criteria is not reliable for identifying chiral bands [41, 42] since a relatively large staggering can be obtained for realistic chiral systems and vanishing staggering may exist also for non-chiral systems.

It was suggested that for a symmetric configuration involving a particle and a hole in the same high-j shell (i.e. $\pi h_{11/2} \otimes \nu h_{11/2}$) in the $A \sim 130$ mass region, and for a non-axial shape with $\gamma = 30^\circ$ there should be staggering in opposite phase in the intra- and inter-band $B(M1)$ reduced transition probabilities [43]. Moreover the $B(M1)$ reduced transition probabilities should have the same phase of staggering in both chiral partner bands. For the $\pi h_{11/2} \otimes \nu h_{11/2}$ configuration, the intra-band $B(M1)$ transition probabilities should be high for even values of I and low for odd values of I . However, it was found in other calculations that this characteristic staggering is not necessarily observed if $\gamma \neq 30^\circ$ or the proton and the neutron do not occupy exactly the bottom and the top of the same j-shell [44]. In another work, it was shown that the $B(M1)$ staggering has a complex origin and its presence or absence can not be used for a reliable identification of chiral symmetry [41, 42].

1.1.4 Suggested chiral candidates in nuclei

For a strongly broken ideal chiral symmetry, a pair of degenerate $\Delta I = 1$ rotational bands should be observed [2]. Currently, the known chiral candidates show similar properties

rather than degeneracy. Pairs of $\Delta I = 1$ rotational bands were observed and suggested as chiral candidates in $A \sim 80, 100, 130,$ and 190 mass regions [4-36]. They are characterized by two or three quasiparticle configurations and most of the side bands are linked with the yrast bands via mixed $M1/E2$ and $E2$ transitions. Majority of the chiral candidates belongs to the $A \sim 130$ and 100 mass regions. A few cases in $A \sim 190$ have been studied so far.

Apart from degeneracy of the excitation energies of the partner bands, which is an important indication of strongly broken chiral symmetry, the chiral doublet bands should exhibit the same electromagnetic transition probabilities. Therefore experimental lifetime measurements are needed in order to deduce the electromagnetic transitions rates. However, lifetime measurements have been performed for a very few nuclei among these chiral candidates (^{102}Rh [45], $^{103,104}\text{Rh}$ [43], ^{106}Ag [46,47], $^{126,128}\text{Cs}$ [48,49], ^{130}Cs [50], ^{132}La [49, 51,52], ^{134}Pr [53,54], ^{135}Nd [55], ^{136}Nd [56], and ^{194}Tl [57,58]).

Two excellent candidates in $A \sim 130$ are $^{126,128}\text{Cs}$ [59,60], with approximately constant excitation energies in the partner bands, $\Delta E \sim 200$ keV, and the same alignments and moments of inertia, while the ratios of the $B(M1)/B(E2)$ and individual $B(M1)$ and $B(E2)$ transition probabilities are similar for most levels of the partner bands.

In the $A \sim 100$ mass region, ^{104}Rh nucleus is suggested as the best chiral candidate. The partner bands show a decreasing trend of the relative excitation energy from $\Delta E = 413$ keV at $I = 11$, to an almost completely vanishing value of $\Delta E = -1$ keV at $I = 17$. The alignments of the partner bands differ by about $1.5 \hbar$. The $B(M1)$ and $B(E2)$ reduced electromagnetic transition probabilities were measured only for a few levels in the yrast band [37].

Perhaps the best chiral candidate known to date was found in $A \sim 190$, in ^{194}Tl [57,58]. The bands are built on 2-quasiparticle configuration, which is followed through a band crossing and into a 4-quasiparticle configuration. The 4-quasiparticle bands have exceptionally good near-degeneracy in the excitation energies, with ΔE not larger than 110 keV, and a close similarity in the alignments, moments of inertia and $B(M1)/B(E2)$ ratios. Lifetime measurements were also performed for 9 states of the yrast band and 6 states of the side band. The obtained $B(M1)$ and $B(E2)$ values show a close similarity [57,58].

It was also predicted that possible multiple pairs of chiral bands can exist in a single nucleus [59-64]. Evidence for this phenomenon was found in ^{133}Ce [65], ^{103}Rh [66], and possibly in ^{194}Tl [67].

1.2 Motivation of this study

In order to extend the knowledge about chiral doublet bands in the $A \sim 190$ mass region, γ -spectroscopy studies have been performed at iThemba LABS in the thallium isotopes [57,68,69] using the AFRODITE detector facility. Most importantly, these investigations showed that ^{194}Tl is perhaps the best chiral candidate to date. Thus, the aim of this work is to study the neighbours of ^{194}Tl , that is $^{192,193}\text{Tl}$.

The present level scheme of ^{193}Tl [70] has one band (Band 2) that is assigned a $\pi h_{9/2} \times \nu i_{13/2}^2$ configuration. This configuration is suitable for a chiral coupling. A side band (Band 3) was also observed, however, no spin and parity were assigned to Band 3 [70], thus its nature remained unresolved.

The ground state band of ^{192}Tl [71] is associated with $\pi h_{9/2} \otimes \nu i_{13/2}$ configuration, which is a suitable configuration for chirality, because it involves one proton with a particle nature and one neutron with a hole nature. However, no partner band had been found in this nucleus.

This work aimed to extend the level scheme of ^{193}Tl and search for chiral partner of the $\pi h_{9/2} \times \nu i_{13/2}^2$ band. In addition, it aimed at γ -spectroscopy studies for ^{192}Tl in order to search for $\pi h_{9/2} \otimes \nu i_{13/2}$ chiral partner bands. Experiments with codes PR175 and PR299 were performed at iThemba LABS for this project.

The previous level scheme of ^{193}Tl [70] was considerably modified and extended. Spins and parities were assigned to most levels including those of Band 3. Three negative parity bands of ^{193}Tl show close-similarity in excitation energies, alignments and $B(M1)/B(E2)$ reduced transition probability ratios. A near-degeneracy found in these three bands sug-

gests that there might be a multiplet of chiral systems in ^{193}Tl . Partial results on ^{193}Tl from this work were published (see Ref. [72]). The level scheme of ^{192}Tl was significantly extended with respect to Ref. [71]. Part of the $\gamma - \gamma$ coincidence analysis was a topic of a MSc project [73]. Analysis to determine the spin and parity of the levels of ^{192}Tl was performed. A partner was found to the $\pi h_{9/2} \otimes \nu i_{13/2}$ band. These bands might exhibit chiral symmetry in ^{192}Tl .

1.3 Outline of thesis

The rest of this thesis has been organized in the following way: A few of theoretical models and terminology relevant to our experimental results are briefly introduced in the second chapter. Chapter 3 describes the experimental techniques and tools as used in this work. Experimental results and corresponding interpretation are given in chapter 4. Conclusions are presented in chapter 5.

Chapter 2

Model description of nuclear structure

2.1 Introduction

The atomic nucleus is composed of protons and neutrons. The force responsible for holding the nucleons together is complex, which makes it difficult to develop an accurate mathematical description of the nucleus. To date various nuclear models have been proposed, but none of them can describe all features exhibited by all nuclei. Every nuclear model has its own limitations. The use of any nuclear model depends on how it is related to the properties of interest. This chapter contains some theoretical models and terminology relevant to our experimental results. The nuclear shape is briefly described. The shell model and a few associated models such as the Nilsson Model, the Cranked shell model (CSM), the Particle-Rotor model, and the Multi-particle rotor (MPR) model are introduced.

2.2 Nuclear surface deformations

The vast majority of nuclei are deformed. The nuclear surface deformation can be described in the geometrical collective model first proposed by Bohr and Mottelson [74, 75] and elaborated by Faessler and Greiner [76-80]. A coordinate $R(\theta, \phi)$ of a point on the

moving nuclear surface can be expressed in terms of physical harmonics $Y_{\lambda\mu}(\theta, \phi)$, with each spherical harmonic component having an amplitude $\alpha_{\lambda\mu}$, such as

$$R(\theta, \phi) = R_0 \left[1 + \alpha_{00} + \sum_{\lambda=1}^{\infty} \sum_{\mu=-\lambda}^{\lambda} \alpha_{\lambda\mu} Y_{\lambda\mu}(\theta, \phi) \right] \quad (2.1)$$

where R_0 is the radius of the spherical nucleus and λ gives the deformation type of the nucleus. Assuming the nuclear fluid to be incompressible, a case with $\lambda = 0$ is forbidden, because it corresponds to a radial dependence with time, i.e. the nucleus expands and contracts with a certain frequency, which is not possible for incompressible nuclear fluid. Cases with $\lambda = 1, 2, 3$, and 4 correspond respectively to dipole, quadrupole, octupole and hexadecapole deformations. Next discussions on the collective model description will focus on the quadrupole deformation (case of $\lambda = 2$).

The nuclear radius $R(\theta, \phi)$ must be real as it should be invariant under a reflection and a rotation of the coordinate system, i.e.

$$R(\theta, \phi) = R^*(\theta, \phi). \quad (2.2)$$

Applying (2.2) to (2.1) and using the property of the spherical harmonics

$$Y_{\lambda\mu}^*(\theta, \phi) = (-1)^\mu Y_{\lambda-\mu}(\theta, \phi) \quad (2.3)$$

one finds that the $\alpha_{\lambda\mu}$ have to fulfill the condition

$$\alpha_{\lambda\mu}^* = (-1)^\mu \alpha_{\lambda-\mu}. \quad (2.4)$$

For the case of pure quadrupole deformation ($\lambda = 2$), (2.4) can be written as

$$\alpha_{2\mu} = (-1)^\mu \alpha_{2-\mu}^*. \quad (2.5)$$

Since $\alpha_{20} = \alpha_{20}^*$, we are left with α_{20} and the real and the imaginary parts of α_{21} and α_{22} , i.e. five independent real degrees of freedom.

Expressing this in Cartesian coordinates by rewriting the spherical harmonics in terms of the Cartesian components in the direction (θ, ϕ) , and a proper rotation of the principal axis system by Euler angles $\Omega(\Omega_1, \Omega_2, \Omega_3)$, the five coefficients reduce to two independent

variables α_{20} and $\alpha_{22} = \alpha_{2-2}$ ($\alpha_{21} = \alpha_{2-1} = 0$). The system is completely described with the two coefficients indicating the variation of axes together with the three Euler angles $\Omega(\Omega_1, \Omega_2, \Omega_3)$ determining the orientation of axes.

Another set of parameters was introduced where α_{20} and α_{22} are expressed as function of the Hill-Wheeler [81] coordinates β_2, γ ($\beta_2 > 0$) such as

$$\alpha_{20} = \beta_2 \cos \gamma \quad (2.6)$$

$$\alpha_{22} = \frac{1}{\sqrt{2}} \beta_2 \sin \gamma \quad (2.7)$$

with

$$\sum_{\mu} |\alpha_{2\mu}|^2 = \alpha_{20}^2 + 2\alpha_{22}^2 = \beta_2^2. \quad (2.8)$$

It is sufficient to use the two parameters (β_2, γ) to describe the nuclear system. The stretching of the axes can be expressed as

$$\delta R_k(\theta, \phi) = \sqrt{\frac{5}{4\pi}} \beta_2 \cos\left(\gamma - \frac{2\pi k}{3}\right), \quad (2.9)$$

where $k = 1, 2, 3$ refer to the principal axes of the nucleus.

At $\gamma = 0^\circ$ the nucleus is elongated along the Z axis while X and Y are equal. This results in a symmetric type of shape called prolate. As γ increases, the X axis grows at the expense of Y and Z axes through a triaxial shape region with three unequal axes. A symmetric shape is reached again at $\gamma = 60^\circ$, but now the Z and X axes become equal in length. This symmetric shape is called oblate. Every 60° this pattern is repeated where the prolate and the oblate shapes alternate. The quadrupole shapes are shown in Fig. 2.1. This parameterization with β_2 and γ is suitable when the nuclear potential is of Woods-Saxon type. It is used in Cranked Shell Model (CSM) and Total Routhian Surface (TRS) calculations.

Another parameterization is expressed in terms of the quadrupole deformation parameters ε_2 and γ , which is often referred to as Nilsson parameterization. It is used when describing a nuclear system with the harmonic oscillator potential. The three harmonic oscillator

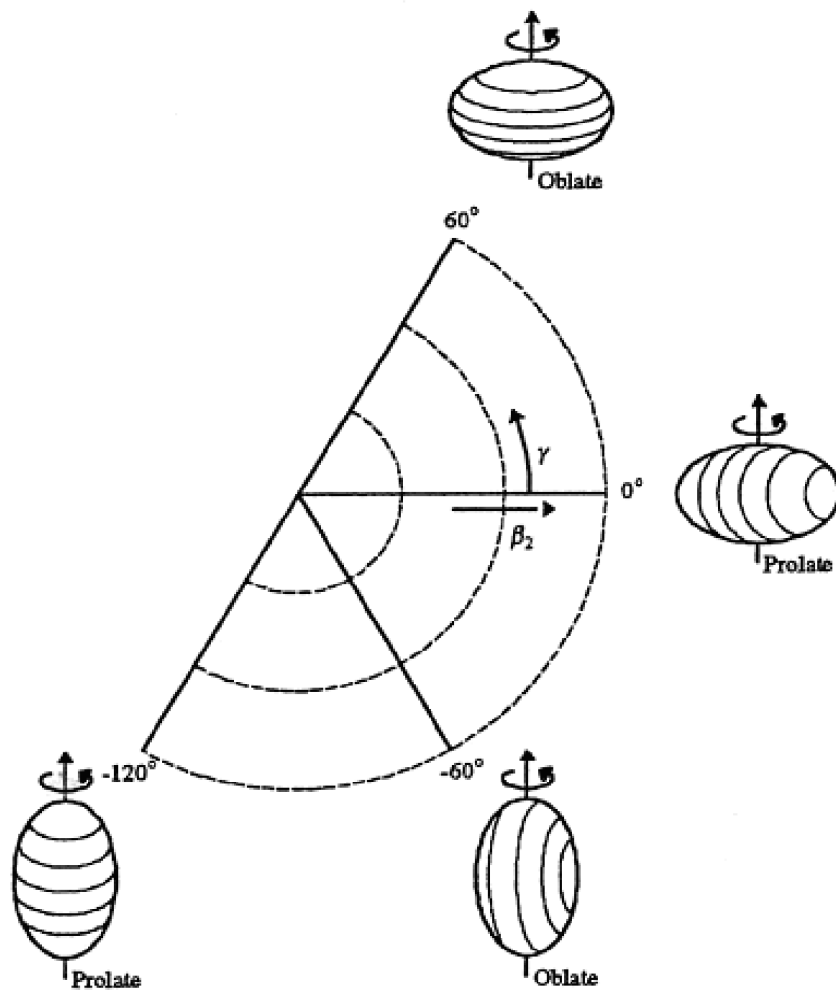


FIG. 2.1. Diagram representation of the nuclear shape in β_2 and γ plane with $\lambda = 2$. Figure taken from [82].

frequencies which correspond to motions of the nucleon along the three axes (labeled 1, 2, and 3), are expressed as

$$\begin{aligned}\omega_1(\varepsilon_2, \gamma) &= \omega_0 \left\{ 1 + \frac{1}{3}\varepsilon_2 \cos \gamma + \frac{1}{\sqrt{3}}\varepsilon_2 \sin \gamma \right\} \\ \omega_2(\varepsilon_2, \gamma) &= \omega_0 \left\{ 1 + \frac{1}{3}\varepsilon_2 \cos \gamma - \frac{1}{\sqrt{3}}\varepsilon_2 \sin \gamma \right\} \\ \omega_3(\varepsilon_2, \gamma) &= \omega_0 \left\{ 1 - \frac{1}{3}\varepsilon_2 \cos \gamma \right\}\end{aligned}\quad (2.10)$$

where ω_0 is the oscillator frequency of an harmonic motion of the particle in a spherical potential.

Both (ε_2, γ) and (β_2, γ) parameterizations are similar and their use is determined by convenience. Only the elongation parameters are not the same with $\beta_2 \sim 0.96 \varepsilon_2$. The role and the value of γ are the same in both parameterizations.

2.3 Shell model

Nuclear physicists used the theory of the atomic model which is known as shell model in order to tackle the problem of the nuclear structure. The shell model forms a basis of many nuclear models. Similarly to the arrangement of electrons in atomic shells, the nucleons are assumed to move independently in an average potential and the energies are filled from the lowest energy to the highest. A sudden and discontinuous behaviour in nuclear properties remarked at certain proton or neutron numbers (Z or $N=2, 8, 20, 28, 50, 82$ and 126) corresponds to the filled major nuclear shells. For any shell theory to be successful the existence of shell closures at those occupation numbers must be reproduced.

In developing the shell model, it is most important to choose an optimal average potential. In order to reproduce the experimental observed magic numbers, the nuclear potential should include a spin-orbit term. For the radial term of the potential one can consider a simple case of finite or infinite square well, which has sharp edges (see Fig. 2.2) and do not approximate the shape of the nuclear matter. It is defined by:

$$V_o(\vec{r}) = \begin{cases} -V_o, & r \leq R \\ 0, & r > R \end{cases}\quad (2.11)$$

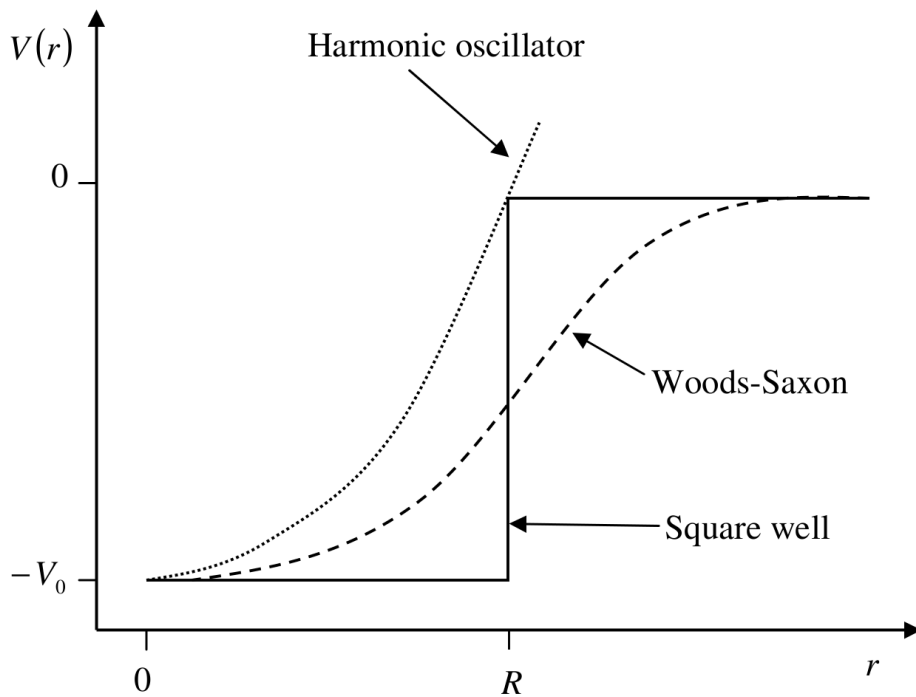


FIG. 2.2. Plot illustrating a comparison between one-dimensional harmonic oscillator potential, square well potential and Woods-Saxon potential.

where V_o is of the order of several MeV and $R \approx r_o A^{\frac{1}{3}}$ fm, with A being the mass number and $r_o \approx 1.2$ fm being the nuclear radius parameter.

Another approximation of the nuclear potential is the harmonic oscillator potential (see Fig. 2.2) defined by:

$$V_o(r) = -V_o + \frac{1}{2}M\omega^2 r^2 \quad (2.12)$$

where V_o is the well depth, M is the mass of the nucleon, and ω is the oscillator frequency of a harmonic motion of the particle in a spherical potential. The harmonic oscillator potential gives an unrealistic shape of the nucleus as it tends to infinity for the large distance r .

The Wood Saxon potential (see Fig. 2.2) described as:

$$V_{WS} = -V_o f(r, R, a) \quad (2.13)$$

where

$$f(r, R, a) = \frac{1}{1 + \exp\left\{\frac{r-R}{a}\right\}}, \quad (2.14)$$

with a being the diffuseness of the potential, describes best the nuclear density. It is coupled with spin-orbit term and Coulomb potential (for protons) to form a realistic potential given by:

$$V(r) = V_c(r) - V_o f(r, R_n, a_n) - V_{s.o} \left(\frac{\hbar}{m_\pi c}\right)^2 \frac{1}{r} \frac{d}{dr} f(r, R_{s.o}, a_{s.o}) \vec{l} \cdot \vec{s} \quad (2.15)$$

with $V_o \approx 50$ MeV, $V_{s.o} \approx 5$ MeV, and typically $R_n \approx R_{s.o} \approx 1.2A^{1/3}$ fm and $a_n \approx a_{s.o} \approx 0.70$ fm [83].

2.4 Nilsson Model

Since some nuclei are deformed in their ground state, it was suggested that a shell model for which the central potential is no longer spherically symmetric. Such potential was developed in the Nilsson Model, proposing employment of the single particle Hamiltonian

$$H = H_o + Cl.s + Dl^2, \quad (2.16)$$

where H_o is an anisotropic harmonic oscillator Hamiltonian, and

$$H_o = -\frac{\hbar^2}{2m} \nabla^2 + \frac{1}{2}m(\omega_x^2 x^2 + \omega_y^2 y^2 + \omega_z^2 z^2), \quad (2.17)$$

$l.s$ is the usual spin-orbit coupling term of the spherical shell model, l^2 is a term meant to simulate a flattening of the oscillator potential and to make it closer to the real potential. The constants C and D can be determined by adjustment to the experimental results.

Assuming the axial symmetry of deformed nuclei with z-axis as the symmetry axis, we can write

$$\begin{aligned} \omega_x^2 = \omega_y^2 &= \omega_o^2 \left(1 + \frac{2}{3}\delta\right) \\ \omega_z^2 &= \omega_o^2 \left(1 - \frac{4}{3}\delta\right) \end{aligned} \quad (2.18)$$

where the frequencies are expressed as function of two parameters (ω_o and δ) and are made to fulfill the condition of conservation of the nuclear volume. This condition requires that $\omega_x\omega_y\omega_z=\varpi_o^3=\text{Constant}$, where ϖ_o is the frequency for a zero deformation. Thus,

$$\omega_o(\delta) = \varpi_o \left(1 - \frac{4}{3}\delta^2 - \frac{16}{27}\delta^3 \right)^{-1/6} \quad (2.19)$$

is a relationship left with a single parameter, called the deformation parameter δ . The energy is calculated by diagonalization of the Hamiltonian as a function of δ [85,86]. Illustrations of the numerical solutions for protons and neutrons are displayed in the Nilsson diagrams shown in Fig.2.3 and Fig.2.4.

2.4.1 Nilsson diagrams

The Nilsson diagrams describe the particle energy levels for a deformed nucleus, with the valence nucleon thought of as a particle orbiting in a mean field potential generated by the bulk of the nucleus. The energy levels depend on the spatial orientation of the orbit and the nuclear deformation. For the total angular momentum oriented nearly perpendicular to the symmetry axis of the core, the total projection Ω onto the symmetry axis is small and the energy corresponding to such projection is low. For a prolate nucleus, the orbital with the smallest projection has the lowest energy, while it is opposite for an oblate nucleus.

The energy levels (after Ω -splitting) are two-fold degenerate due to the reflection symmetry of the nucleus. The orbit with the same $|\Omega|$ (i.e. $\pm\Omega$) are equivalent and are characterized by the same energy. For example a state with $j = 5/2$ in a prolate nucleus will have three distinct energy levels with $|\Omega|=1/2, 3/2, 5/2$, where the $|\Omega|=1/2$ level has the lowest energy and the $|\Omega|=5/2$ has the highest.

The degree of Ω -splitting can be expressed by

$$\theta = \sin^{-1} \frac{\Omega}{j}. \quad (2.20)$$

Thus, the energy splitting between adjacent Ω values is large for large values of Ω and smaller for small values of Ω . For example for $j=5/2$, the spacing between the $|\Omega|=1/2$ and $|\Omega|=3/2$ levels is smaller than that between $|\Omega|=3/2$ and $|\Omega|=5/2$.

The energy levels are altered by the mixing of two levels with the same quantum numbers Ω and parity π . Since such two levels cannot cross due to the Pauli exclusion principle, as they approach each other in energy, they mix strongly, and the states repel. This repulsion refers to the apparent bending of states observed in the Nilsson diagrams.

This energy level description accounts for the ground state and the first few excited states in the nuclei, where the single particle motion and the rotation of the core can be considered separately. In the case of fast rotation of the core, the effects of the nuclear rotation on the states are no longer negligible and the Nilsson single particle energies need correction.

2.5 Collective Models

It is postulated in the independent particle model that the nuclear properties are mainly determined by the extra or missing nucleons at either side of the shell closure. However there are general properties which are common to all nuclei and can reasonably be identified not only with the motion of a few valence nucleons but the entire nucleus. This is known as nuclear collective motion where many nucleons contribute cooperatively to the nuclear properties. Illustrations to the nuclear collective motion can be interpreted in terms of vibrations of the nuclear surface and rotations.

2.5.1 Nuclear rotations

Nuclei with nonspherical equilibrium shapes exhibit a structure more characteristic of a rotational motion. These nuclei are called deformed, as they are found to have a substantial permanent distortions from spherical shape. For nuclei with spherical shapes, it is not possible to observe the collective rotation about an axis of symmetry, since the different orientations of the nucleus are quantum mechanically indistinguishable.

The deformed nuclei rotate about an axis perpendicular to the symmetry axis. Assuming the nuclear moment of inertia \mathfrak{S} to be constant and equivalent to the rigid body value for

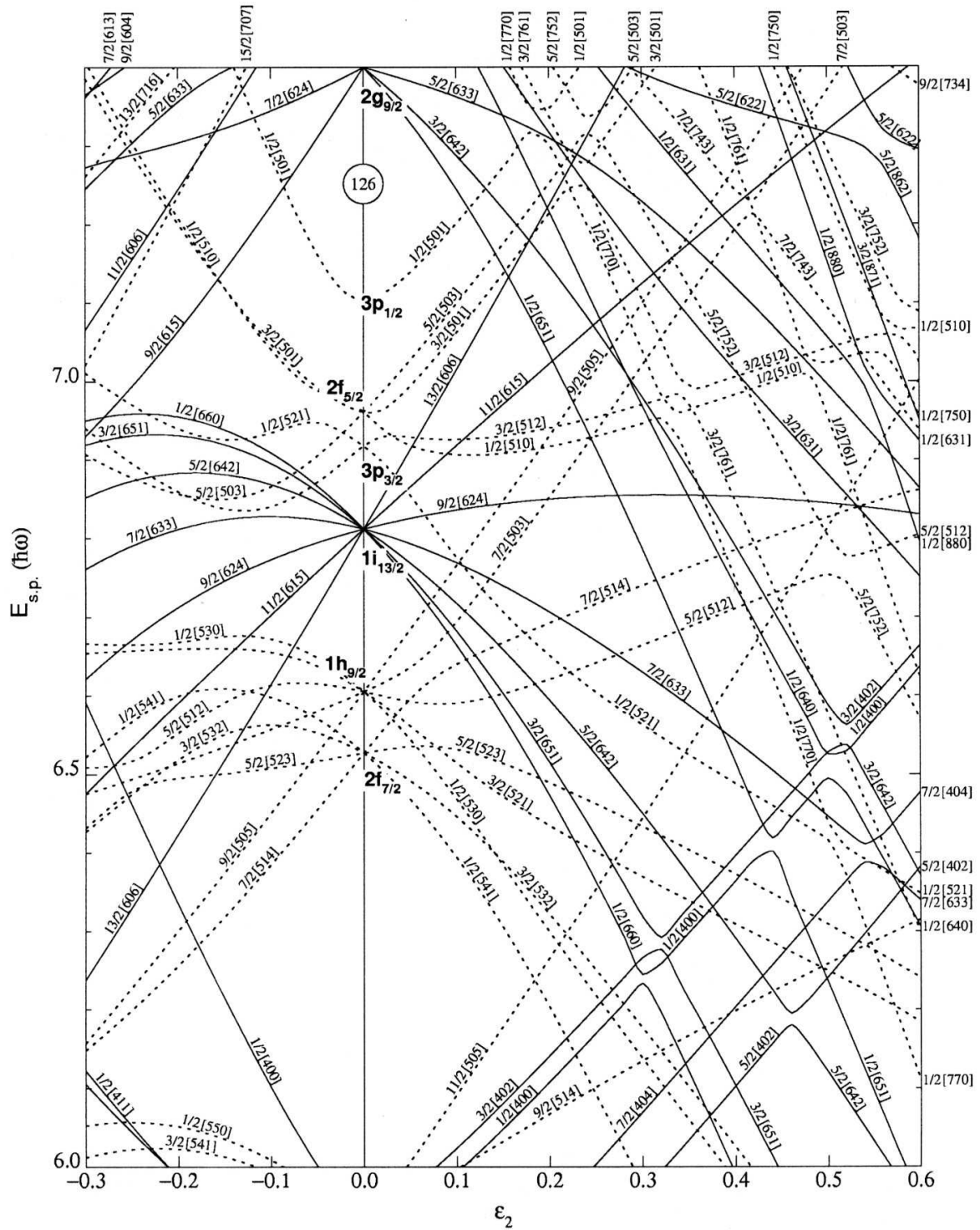


FIG. 2.3. Plots of the energy levels for neutrons ($82 \leq N \leq 126$) as a function of ϵ_2 ($\epsilon_4 = \epsilon_2^2/6$) in a prolate ($\epsilon_2 > 0$) and oblate ($\epsilon_2 < 0$) nucleus. The quantum numbers $\Omega(Nn_z m_i)$ label the states. Solid and dashed lines indicate the states with positive and negative parity respectively [83,84].

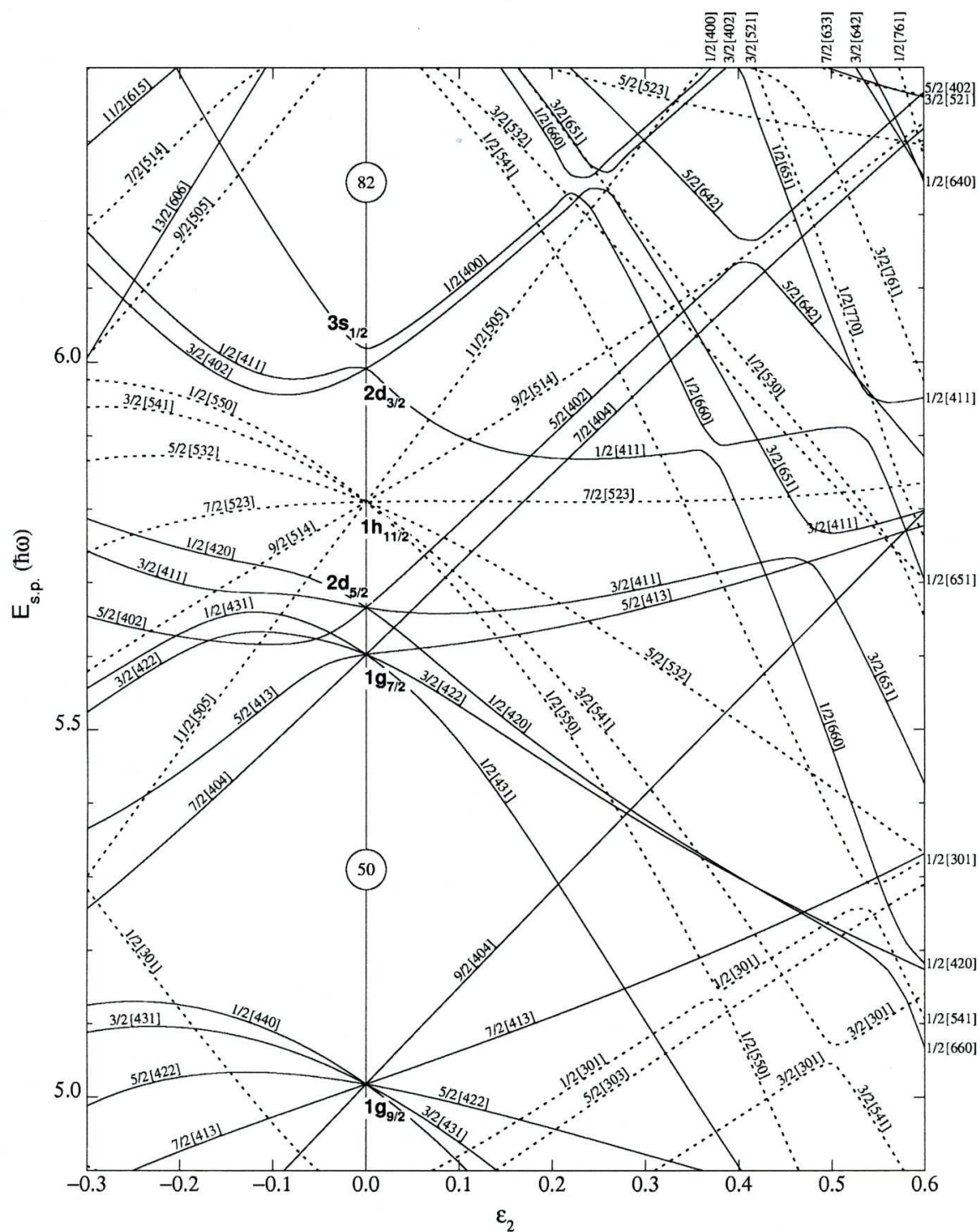


FIG. 2.4. Plots of the energy levels for protons ($50 \leq P \leq 82$) as a function of ϵ_2 ($\epsilon_4 = \epsilon_2^2/6$) in a prolate ($\epsilon_2 > 0$) and oblate ($\epsilon_2 < 0$) nucleus. The quantum numbers $\Omega(Nn_z m_l)$ label the states. Solid and dashed lines indicate the states with positive and negative parity respectively [83,84].

an ideal rotor, the kinetic energy E is expressed by:

$$E = \frac{1}{2\mathfrak{I}}R^2 \quad (2.21)$$

where R is the rotational angular momentum.

Letting I represent the total angular momentum quantum number with I^2 equivalent to $I(I+1)\hbar^2$, the energies of a rotating body in quantum mechanics are given by

$$E(I) = \frac{\hbar^2}{2\mathfrak{I}}I(I+1). \quad (2.22)$$

Thus, increasing the quantum number I results in a sequence of nuclear excitation energies or a rotational band. This is a good approximation for many nuclei.

2.5.2 Nuclear Vibrations

The nuclear vibrations are compared to a liquid drop where vibrational quanta called "phonons" are generated. Based on description of the nuclear surface in terms of spherical harmonics, possible modes of vibrations are identified. Mode with $\lambda=0$ is forbidden since the nuclear matter is highly incompressible, and mode with $\lambda=1$ is also forbidden as it will produce a net displacement of the centre of mass, which is not possible in the absence of external forces. For $\lambda \geq 2$, the resulting energy spectra are equally spaced with separation energy

$$\Delta E_l = \hbar \sqrt{\frac{C_l}{B_l}} \quad (2.23)$$

where B_l and C_l are the inertia and spring constants respectively. The lowest energy vibration quanta correspond to $\lambda=2$, where a single unit is equivalent to a quadrupole phonon. The $\lambda=2$ phonon is assigned a positive parity $(-1)^\lambda = +1$. An even-even nucleus in the ground state has $I^\pi = 0^+$. Adding two $\lambda = 2$ phonons gives $0^+, 2^+, 4^+$ states. Mode with $\lambda = 3$ produces octupole vibrations (see Fig. 2.5) of $\lambda = 3$ phonons resulting in bands with negative parity [85].

2.5.3 Collective rotation in the body-fixed frame: Cranked Shell Model (CSM)

At very high spin, the Coriolis and centrifugal forces can modify the nucleon orbits in a nucleus. The cranked shell model which was first proposed by Inglis [86,87] is one of the

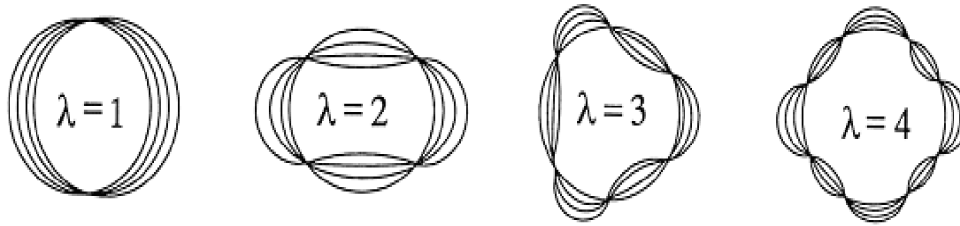


FIG. 2.5. Diagram showing the lowest three vibrational modes of a nucleus.

most often used models giving a microscopic description of the influence of rotation on the single-particle motion. In this model, it is suggested that independent particles move in a non-axial shell potential, which is rotating with the nucleus. The time-dependant Schrödinger equation is transformed from the space-fixed coordinate axes to the axes fixed with the rotating body. The single-particle cranking Hamiltonian called Routhian in the intrinsic coordinates of the rotating system is defined by:

$$h^\omega = h - \hbar\omega j_x \quad (2.24)$$

where h is the Hamiltonian in the laboratory system, j_x is the projection of the single-particle angular momentum onto the rotational axis and ω is the rotational frequency [88]. The term $-\hbar\omega j_x$ is classically equivalent to the Coriolis and centrifugal forces. The total cranking Hamiltonian can be obtained from the sum of h^ω for all the independent particles:

$$H^\omega = \sum_v h^\omega = H - \hbar\omega I_x \quad (2.25)$$

where I_x is the sum over all occupied states of the expectation values of the individual nucleon angular momenta along the rotational axis and v denotes the occupied orbitals.

$$I_x = \sum_v j_x. \quad (2.26)$$

The eigenvalues for H^ω are equivalent to

$$E^\omega = \sum_v e^\omega \quad (2.27)$$

or

$$E^\omega = E - \hbar\omega I_x. \quad (2.28)$$

The lowest eigenstate E_ω corresponds to a yrast state and the sequence of these states for higher frequencies ω constitutes the yrast line.

It is essential to study the symmetries in the cranked single particle Hamiltonian in order to determine the quantum numbers which are used to describe a rotational state in a nucleus. For a Hamiltonian h describing the non-rotating nuclear system, there are symmetries related to the invariance with respect to space and time inversion. The space inversion gives the parity quantum number, whereas the time inversion yields the two-fold degeneracy of nuclear levels, called Kramer's degeneracy.

Depending on the nuclear shape, an invariance of the nuclear potential with respect to the rotations of 180° around the three axes of the system can occur. The corresponding rotation operators are given by:

$$R_k = e^{-i\pi j_k} \quad (2.29)$$

where k denotes the three principal axes 1, 2, and 3, and j_k the projection of the single particle angular momentum onto the k axis.

In the case of the cranking Hamiltonian h^ω , the time reversal symmetry is broken when the system is constrained to rotate. Thus, the Kramer's degeneracy is broken and another additional quantum number is needed to describe the system. In addition, the invariance of the nuclear potential with respect to the rotation operators R_k is not valid in all cases, because of the rotation of the coordinate basis. It is particularly broken for the R_2 and R_3 operators as they do not commute with the operator j_1 . However, the invariance still holds true for R_1 and therefore one can introduce an additional quantum number, r , called signature, as an eigenvalue of this operator. Often, another quantum number, α , is used. It is related to r by:

$$r = e^{-i\pi\alpha}. \quad (2.30)$$

The operator R_1^2 is equivalent to a rotation of the system through an angle 2π . Applying it to an anti-symmetric total wavefunction, ($R_1\psi = -\psi$) for an odd-mass system, one finds that $r = \pm i$, corresponding to $\alpha = \pm 1/2$. Similarly the symmetric wavefunction for an even-mass system gives $r = \pm 1$, corresponding to $\alpha = 0$ and $\alpha = 1$ respectively. The total

nuclear spin I can be related to α as [89]:

$$\begin{aligned}
 I &= 0, 2, 4, 6, \dots, r = 1, \alpha = 0 \\
 I &= 1, 3, 5, 7, \dots, r = -1, \alpha = 1 \\
 I &= 1/2, 5/2, 9/2, \dots, r = -i, \alpha = 1/2 \\
 I &= 3/2, 7/2, 11/2, \dots, r = i, \alpha = -1/2.
 \end{aligned}
 \tag{2.31}$$

In summary, one can write:

$$I = \alpha, \alpha + 2, \alpha + 4, \dots \tag{2.32}$$

It is then important in the high-spin region to classify the rotational spectra in terms of signature as a quantum number. For instance, a band classified by the projection K of the intrinsic spin onto the symmetry axis at low spin, separates in two bands at higher spin, with a different value of signature α for each band.

2.4.3.1 Experimental observables in the rotating basis

In order to compare the calculated values with the experimental observables, the level energies and spins which are measured in the laboratory frame, are transformed to the rotating frame, instead of converting the calculated values to the laboratory frame. A sequence of nuclear states forms a rotational band, which is related to a certain configuration of quasi-particles and thus to certain Routhians. A simple relation between the total signature α of a state and its total angular momentum is given in equation (2.31).

The aligned angular momentum I_x along the rotational axis for the state with spin I is defined as:

$$I_x(I) = \sqrt{I(I+1) - K^2} \sim \sqrt{(I+1/2)^2 - K^2}, \tag{2.33}$$

for a nucleus decaying from a state with spin $I+1$ to a state with spin $I-1$. The experimental rotational frequency is defined at the discrete intermediate spin value I as:

$$\hbar\omega(I) = \frac{dE}{dI_x} = \frac{E(I+1) - E(I-1)}{I_x(I+1) - I_x(I-1)}. \tag{2.34}$$

If the angular momentum projection K , on the symmetry axis is sufficiently conserved, it may be obtained from the bandhead spin. The sequence of discrete points $I_x(\omega(I))$ can

be connected by interpolation to the continuous function $I_x(\omega)$.

The Routhian E^ω , is defined as:

$$E^\omega = \frac{1}{2} [E(I+1) + E(I-1)] - \hbar(I)I_x(I). \quad (2.35)$$

For comparisons with the CSM quantities, one needs first to define the experimental energies E^ω and the aligned angular momentum I_x relative to a reference rotational band

$$\begin{aligned} i^\omega &= I_x^\omega - I_{xref}^\omega \\ e^\omega &= E^\omega - E_{ref}^\omega. \end{aligned} \quad (2.36)$$

Often, the ground-state rotational band or the first excited band are used as a reference. It is also possible to use a band belonging to an adjacent core nucleus. The reference functions can be calculated by parameterization with respect to the Harris expansion up to the first two terms [90]:

$$I_{xref}^\omega = \hbar^{-1}\omega J_{ref}^{(1)} = \hbar^{-1} (J_0\omega + J_1\omega^3) + i, \quad (2.37)$$

where $i = 0$, when the ground band is used as a reference. The initial aligned angular momentum is equal to i , if the reference is the first excited band. J_0 and J_1 can be obtained by fitting the quantity $\hbar I_{xref}^\omega/\omega$ as a function of ω^2 with a linear function. The reference energy, E_{ref}^ω , is obtained from the differential equation:

$$\frac{dE_{ref}^\omega}{d\omega} = -\hbar I_{xref}^\omega, \quad (2.38)$$

so that:

$$E_{ref}^\omega = -\hbar \int I_{xref}^\omega d\omega = -\frac{1}{2}J_0\omega^2 - \frac{1}{4}J_1\omega^4 + \frac{\hbar^2}{8J_0}. \quad (2.39)$$

The integration constant ensures that the ground state energy $E_{ref}^\omega(I = 0)$ is approximately equal to zero.

Deviations from the rotational behaviour which manifest themselves by irregularities in the smooth increase of the aligned angular momentum I_x as a function of ω , refers to a phenomenon called "backbending effect". For a certain critical frequency, one observes a sudden increase in alignment, whereas the rotational frequency decreases rapidly. The

backbending effect is due to the sudden alignment of the angular momenta of two quasi-particles along the axis of rotation. One notes that as the pairing correlations decrease at higher spins and the exact dependence is not known, different approximations are used in the literature.

2.5.4 Calculation of potential energy surface applicable to experimental data

Theoretical calculations for the potential energy surface corresponding to $^{192,193}\text{Tl}$ were performed using the Cranked Nilsson Strutinsky (CNS) codes [91-93], with standard parameters for the Nilsson potential and a configuration involving one proton in the $h_{9/2}$ shell and 7 (8) neutrons in the $i_{13/2}$ shell for ^{192}Tl (^{193}Tl). The CNS codes have been developed to calculate properties of nuclei at high spin such that pairing can be neglected or is of minor importance. The minimum total energy of the nucleus is calculated as a function of its deformation and frequency.

Based on the Cranked Woods-Saxon Bogolyubov-Strutinsky approach, the total Routhian $E^\omega(Z, N, \hat{\epsilon})$ at frequency ω and deformation $\hat{\epsilon}$ is equal to the sum of the macroscopic liquid-drop energy and the shell correction energy:

$$E_{tot}(Z, N, \hat{\epsilon}) = E_{LD}^\omega(Z, N, \hat{\epsilon}) + E_{shell}^\omega(Z, N, \hat{\epsilon}), \quad (2.40)$$

where the standard liquid-drop mass formula is used for the liquid-drop macroscopic term [63]. The moment of inertia has the value of the rigid rotor with $R = 1.16 A^{1/3} fm$. The shape is described as a function of the quadrupole ε_2 and hexadecapole ε_4 degrees of freedom including the non-axial deformation γ , $\hat{\epsilon} = (\varepsilon_2, \gamma, \varepsilon_4)$.

Calculations are carried out in a mesh in $(\varepsilon_2, \gamma, \varepsilon_4)$. For a given configuration and each spin, the total energy of a nucleus is determined by a minimisation in the shape degrees of freedom. Then, the total energy and the shape trajectory as a function of the spin are obtained.

The primary deformation lattice is transformed into Cartesian coordinates, $X = \varepsilon_2 \cos(\gamma + 30)$ and $Y = \varepsilon_2 \sin(\gamma + 30)$ and has 15×18 points in the (X, Y) plane, starting from $X = 0.0$

and $Y = 0.28$ with step length of 0.04. The calculations were performed at five different hexadecapole deformations with step of 0.03 and for 16 different rotational frequencies. The minimization was performed in the way that for a fixed configuration the total Routhian was first minimized at each (ε_2, γ) grid point with respect to ε_4 and in a second step the equilibrium deformation was obtained by minimizing over the whole grid.

2.5.5 Particle-Rotor Model

In the particle plus rotor model [94-96], the motion of the valence particles and the motion of the remaining particles confined in the collective rotor, combine to determine the nuclear properties. In an odd-mass nucleus the unpaired nucleon is coupled to an even-even core. If the nucleus is slowly rotating as compared to the valence nucleon motion, it can be described by separating its motion into intrinsic and rotation parts, with no coupling between these two degrees of freedom. The total angular momentum of the system is given by the sum of the collective angular momentum of the core R and the intrinsic angular momentum of the valence particle j :

$$I = R + j. \quad (2.41)$$

Thus, the nuclear Hamiltonian can be expressed as:

$$H = H_{core} + H_{int} = \frac{\hbar^2}{2\mathfrak{I}} R^2 + H_{int}. \quad (2.42)$$

Substituting R by $I - j$, one can write this relation as:

$$H = \frac{\hbar^2}{2\mathfrak{I}} [I^2 + j^2 - 2(I \cdot j)] + H_{int}. \quad (2.43)$$

Assuming the axial symmetry of the rotor, there is no collective rotation around the symmetry axis. Thus, the 3-component of R vanishes and the projection of the total angular momentum along the symmetry axis, $I_3 = K$ comes entirely from the intrinsic part of the angular momentum j_3 . Therefore, the Hamiltonian can be re-written as:

$$H = H_0 + H_c \quad (2.44)$$

where

$$H_0 = \frac{\hbar^2}{2\mathfrak{I}} [I^2 - I_3^2 + (j_1^2 + j_2^2)] + H_{int} \quad (2.45)$$

and

$$H_c = -\frac{\hbar^2}{2\mathfrak{S}} (I \cdot j) = \frac{\hbar^2}{2\mathfrak{S}} (j_+ I_- + j_- I_+). \quad (2.46)$$

The term H_c corresponds to the Coriolis coupling of the intrinsic particle motion with that of the rotating core. The I_+ , I_- and j_+ , j_- are the raising and lowering operators of the total angular momentum and particle angular momentum respectively, with $I_{\pm} = I_1 \pm iI_2$ and $j_{\pm} = j_1 \pm ij_2$. The Coriolis term leads to a mixture of various rotational states with the same I , but different values of K . All the components of the Hamiltonian have different effects depending on the physical situation, where two important limits can be considered:

- a) Deformation alignment (Strong coupling limit)
- b) Rotational alignment (Decoupling limit).

a) Deformation alignment

If the nuclear deformation is large and there are no very high angular momenta I , the Coriolis term is not strong enough to align the spin of the odd particle along the rotational axis. The valence particle angular momentum tends to align with the symmetry axis, where its component K becomes dominant (see Fig. 2.6). This is called strong coupling or deformation alignment since K is a good quantum number. For $I \geq K$ and $K \neq \frac{1}{2}$, the spins $I = K, K + 1, K + 2$ are observed and the corresponding rotational band have level energies:

$$E_{IK} = \frac{\hbar^2}{2\mathfrak{S}} [I(I + 1) - K^2]. \quad (2.47)$$

b) Rotational alignment

In this case, the nuclear deformation is small and the rotational frequency is large enough such that the Coriolis interaction can align the valence particle angular momentum along the rotational axis. In particular, the nucleons from the high- j orbitals which have a large angular momentum projection j_1 along the rotational axis while Ω is short, decouple from the rotational motion of the core (see Fig. 2.6). These nucleons oscillate around the rotational axis and the spin values of the nuclear states are completely determined by j_1 :

$$I = j_1, j_1 + 2, j_1 + 4, \dots, \quad (2.48)$$

where the level energies of the corresponding rotational band follow the exact rotational rule:

$$E = \frac{\hbar^2}{2\mathfrak{I}} (I - j_1) (I - j_1 + 1). \quad (2.49)$$

If $j_1 = j$, the energy is completely pushed down leading to a band which lies at lowest energy. This band has a complete alignment and is called favored band. In rare cases $j_1 = j - 1$, and this corresponds to a band with less alignment which is called unfavored band. This band has a spin sequence of

$$I = j - 1, j + 1, j + 3, \dots \quad (2.50)$$

Rarely this band is seen in heavy-ion induced reaction.

2.5.6 Multi-particle rotor (MPR) model

The fact that chiral doublet bands have been suggested so far in odd-odd, even-even and odd-A nuclei, suggests that a particle rotor model based on n-valence protons and n-valence neutrons is highly desirable. Such model was used for successful calculation of the energy spectra and electromagnetic transition probabilities of the doublet bands in ^{135}Nd [97]. We will apply the multi-particle rotor model of Gillis and Ragnarsson [93] to our study of chiral symmetry in $^{192,193}\text{Tl}$.

The total Hamiltonian is expressed as,

$$\hat{H} = \hat{H}_{coll} + \hat{H}_{intr}, \quad (2.51)$$

where \hat{H}_{coll} stands for the collective rotor Hamiltonian and \hat{H}_{intr} is the intrinsic Hamiltonian for valence nucleons. The first component of \hat{H} is expressed as,

$$\hat{H}_{coll} = \sum_{k=1}^3 \frac{\hat{R}_k^2}{2\mathfrak{I}_k} = \sum_{k=1}^3 \frac{(\hat{I}_k - \hat{j}_k)}{2\mathfrak{I}_k}, \quad (2.52)$$

where $k = 1, 2, 3$ refers to the three principal axes of the body-fixed frame. The quantities $\hat{R}_k, \hat{I}_k, \hat{j}_k$ denote the angular momentum operator for the core, the total angular momentum of the nucleus and the angular momentum of the valence nucleons, respectively. The quantity \mathfrak{I}_k corresponds to the moments of inertia for irrotational flow with

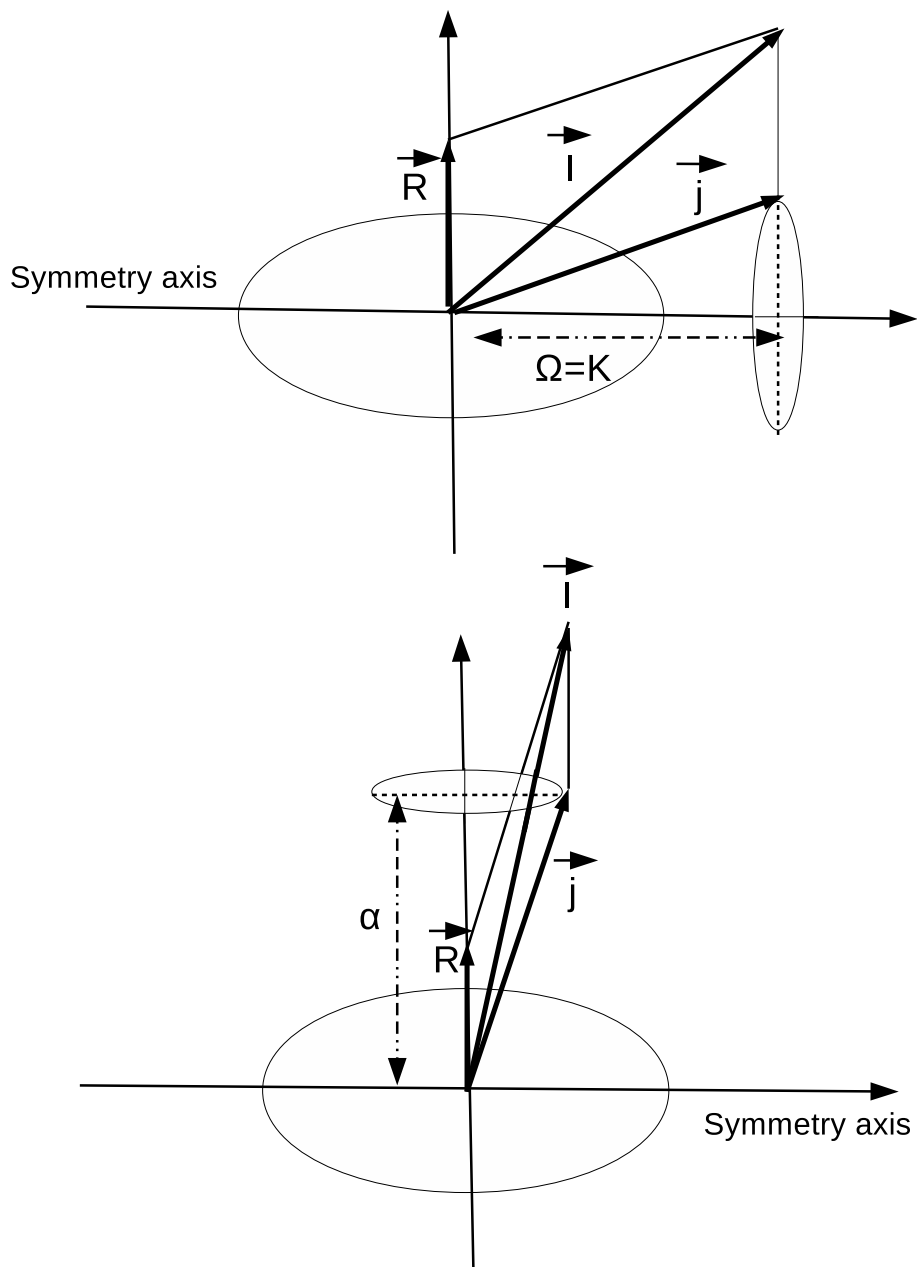


FIG. 2.6. Schematic illustration of the deformation alignment (top panel) and rotation alignment (bottom panel).

$\mathfrak{S}_k = \mathfrak{S}_0 \sin^2(\gamma - 2\pi k/2)$. The intrinsic Hamiltonian \hat{H}_{intr} of the valence nucleons is expressed as

$$\hat{H}_{intr} = \sum_{\nu} \varepsilon_{p,\nu} a_{p,\nu}^+ a_{p,\nu} + \sum_{\nu'} \varepsilon_{n,\nu'} a_{n,\nu'}^+ a_{n,\nu'}, \quad (2.53)$$

where $\varepsilon_{p,\nu}$ and $\varepsilon_{n,\nu'}$ are the single particle energies of the protons and the neutrons. The single particle energies for a simple triaxially deformed single-j shell Hamiltonian are

$$h_{sp} = \pm \frac{1}{2} C \left\{ \cos \gamma \left(\hat{j}_3^2 - \frac{j(j+1)}{3} \right) + \frac{\sin \gamma}{2\sqrt{3}} (\hat{j}_+^2 + \hat{j}_-^2) \right\}, \quad (2.54)$$

where \pm refers to particle or hole, and the coefficient C is proportional to the quadrupole deformation β [97]. The MPR model [93] uses the Nilsson Hamiltonian to calculate the single-particle energies.

The existence of chiral symmetry within this model is exhibited by the angular momenta orientations. One can calculate the expectation values of the squared angular momentum components for the nucleus $I_k = \sqrt{\langle \hat{I}_k^2 \rangle}$, the core $R_k = \sqrt{\langle \hat{R}_k^2 \rangle}$, the valence neutrons $j_{nk} = \sqrt{\langle \hat{j}_{nk}^2 \rangle}$, and the valence protons $j_{pk} = \sqrt{\langle \hat{j}_{pk}^2 \rangle}$. Based on these values of the angular momenta, the forming of the chiral geometry can be illustrated in a plot showing these projections on the short, long and intermediate axes.

Chapter 3

Experimental techniques and tools

Investigations on the nuclear structure at high spins require specific experimental techniques. This chapter contains details about population of high spin states in atomic nuclei, methods of measurements, experimental tools and setup used in this work.

3.1 Nuclear reaction

Nuclei of interest were produced via heavy-ion fusion evaporation reaction. Among the methods to produce nuclei at high angular momentum the heavy-ion fusion evaporation reaction is the most commonly used and efficient. A heavy ion is defined as any projectile of mass $A > 4$ and the accelerators can often produce beams of ions up to ^{238}U at energies of about 1-10 MeV per nucleon [98]. In the fusion reaction a projectile bombards a target at the energy which is chosen to overcome the Coulomb barrier and to maximize the production of high spin states of the nuclei of interest. Below the Coulomb barrier only the Coulomb excitation of the target will take place. One can refer to the classical Coulomb potential energy which is given by

$$U = \frac{1}{4\pi\epsilon_0} \frac{Z_1 Z_2 e^2}{r} \quad (3.1)$$

where Z_1, Z_2 are the atomic numbers of the projectile and the target respectively, e is the elementary charge and r is the total radius expressed as $r = R_1 + R_2$ with $R = 1.22A^{1/3}$ fm. R_1 (R_2) is the radius of the projectile (target). ϵ_0 is the permittivity of free space.

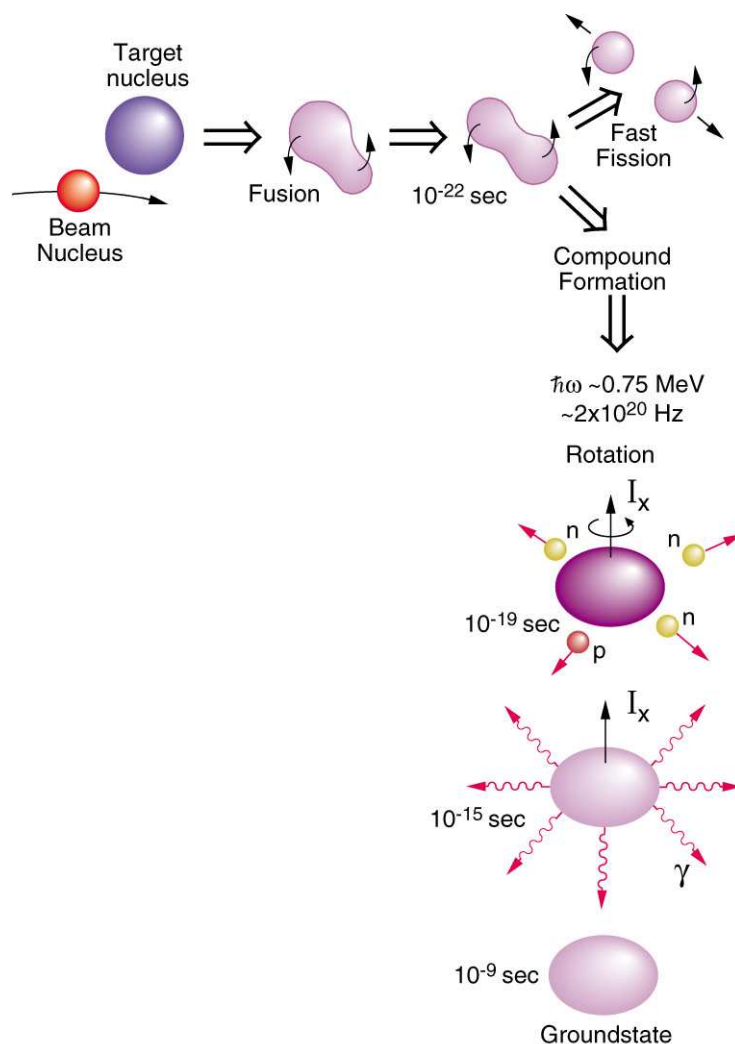


FIG. 3.1. Schematic illustration of heavy-ion fusion evaporation reaction showing consecutive phases up to the ground state of the residual nucleus [99].

The two nuclei (projectile and target) are assumed to be spheres that touch each other at the surface. When the projectile overcomes the Coulomb barrier, it may fuse with the target nucleus forming a compound nucleus, which is often at high excitation energy and angular momentum. If the angular momentum of the compound nucleus is high, which occurs usually for high impact parameters and high momentum of the projectile, the compound nucleus has high probability to fission. Heavy nuclei are particularly unstable with respect to fission. The fusion between the projectile and the target occurs within $\sim 10^{-22}$ - 10^{-20} s. The compound nucleus can be compared to a "hot" deformed liquid drop. The compound system rotates very rapidly, up to 2×10^{20} Hz (see Fig. 3.1.). Kinetic energy

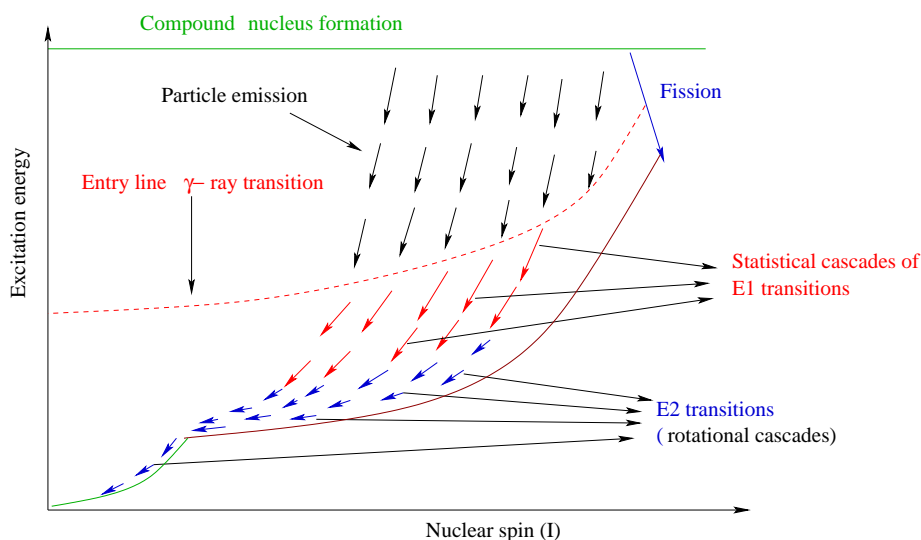


FIG. 3.2. Schematic illustration of the excitation energy states as a function of the nuclear spin (angular momentum) I for heavy-ion induced fusion evaporation reaction.

of the projectile which is not used to overcome the Coulomb barrier, is converted into excitation energy of the compound nucleus and into recoil energy. The excited compound nucleus decays first by emitting particles (such as neutrons, protons and α -particles). For heavier nuclei (e.g. $A > 50$), neutrons are favored over protons and α -particles as they are uncharged and thus insensitive to the Coulomb barrier when ejected from a compound nucleus not far from the stability line. If the compound nucleus is neutron deficient, the probability for proton emission increases. The excited compound nucleus has an angular momentum which is perpendicular to the beam direction. The evaporated particles carry away a small amount of angular momentum and the magnitude of the compound nuclear angular momentum remains almost unchanged. However, through particle evaporation the compound nucleus loses considerable amount of the initial excitation energy, of about 8 MeV of separation energy for an emitted neutron plus its kinetic energy (~ 1 -2 MeV). The kinetic energy of the evaporated particle has statistical distribution due to the very high density of the states in the excited compound system [100]. The particle evaporation ends when the excitation energy of the residual nucleus becomes less than the particle emission threshold. At this stage, the residual nucleus still having a high angular momentum enters the "entry-region" which is about one neutron binding energy above the "Yrast line".

The residual nucleus cools down by emitting statistical γ -rays, mainly E1 γ -ray transi-

tions. These transitions are called quasi-continuum transitions since nuclear level density is very high around the entry-line. The nuclear level density decreases considerably as the nucleus approaches the yrast line. Roughly 2-3 MeV above the yrast line, the decay of the residual nucleus is dominated by a cascade of discrete transitions along the yrast line. For a deformed nucleus, the E2 transitions de-excite the system through many collective bands. The total decay process ends within about 10^{-9} s when the nucleus comes to the ground state (see Fig. 3.2).

Detection of discrete γ -transitions in γ -spectroscopy experiments gives information to study the nuclear structure. In this work the target and the projectile were chosen to produce the nuclei of interest, $^{192,193}\text{Tl}$. PACE [101] (Projected Angular momentum Coupled Evaporation) program was used for a cross section calculation with respect to the beam energy (see Fig. 3.3).

3.2 Interaction of gamma rays with matter

A γ -ray must interact with a detector in order to be detected. As γ -rays pass through matter they interact with atoms through three mechanisms: the photoelectric effect, Compton scattering and pair production. Detection of γ -quanta and different measurements of the γ -ray properties are performed based on these three processes, each of them having a certain probability to occur (see Fig. 3.7).

3.2.1 Photoelectric effect

In this process a γ -photon interacts with and transfers its energy to an atomic electron. This interaction results in the ejection of a photo-electron with kinetic energy equal to the difference between the photon energy and the binding energy of the electron. The photoelectric effect is dominant for γ -rays with low energy ($E_\gamma < 100$ keV) and increases with the atomic number Z of the medium. The absorption probability is approximately given by:

$$\sigma_{pe} = C \frac{Z^n}{E_\gamma^3}, \quad (3.2)$$

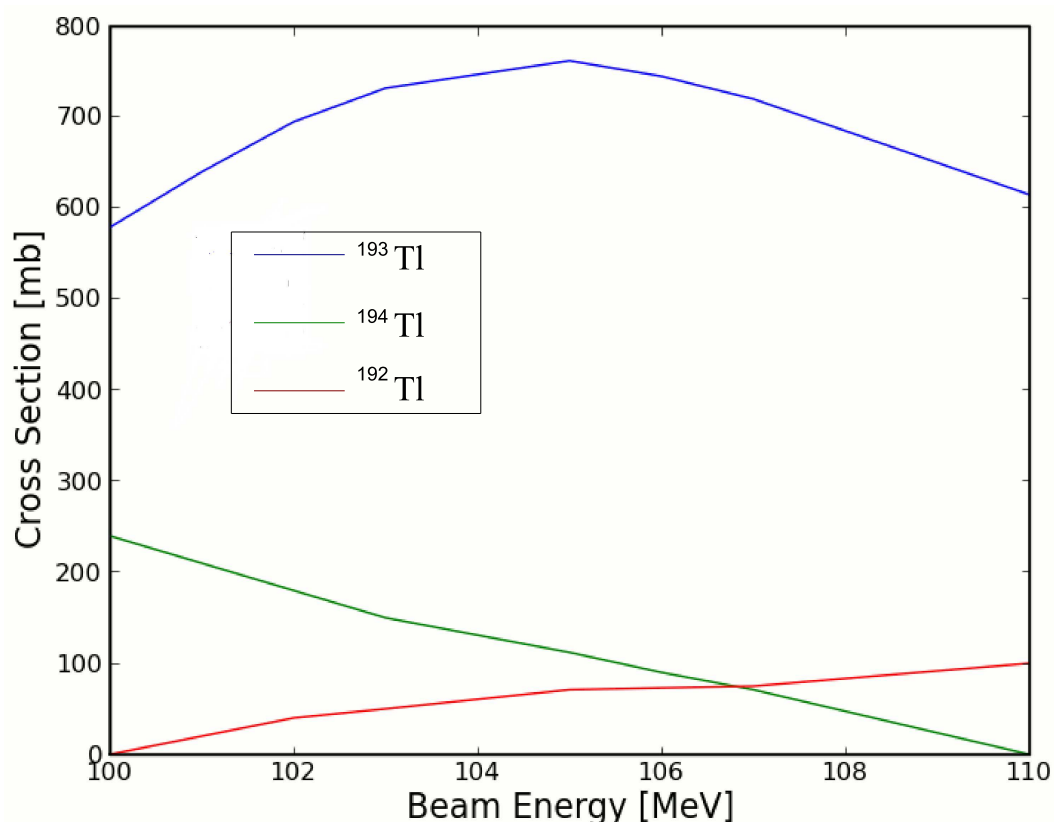


FIG. 3.3. Plot for the $^{181}\text{Ta}(^{18}\text{O}, xn)$ reaction cross-section as calculated with the PACE program. A large cross-section from $^{181}\text{Ta}(^{18}\text{O}, 6n)$ to study ^{193}Tl could be obtained using the beam energy of $E_{lab} = 105$ MeV.

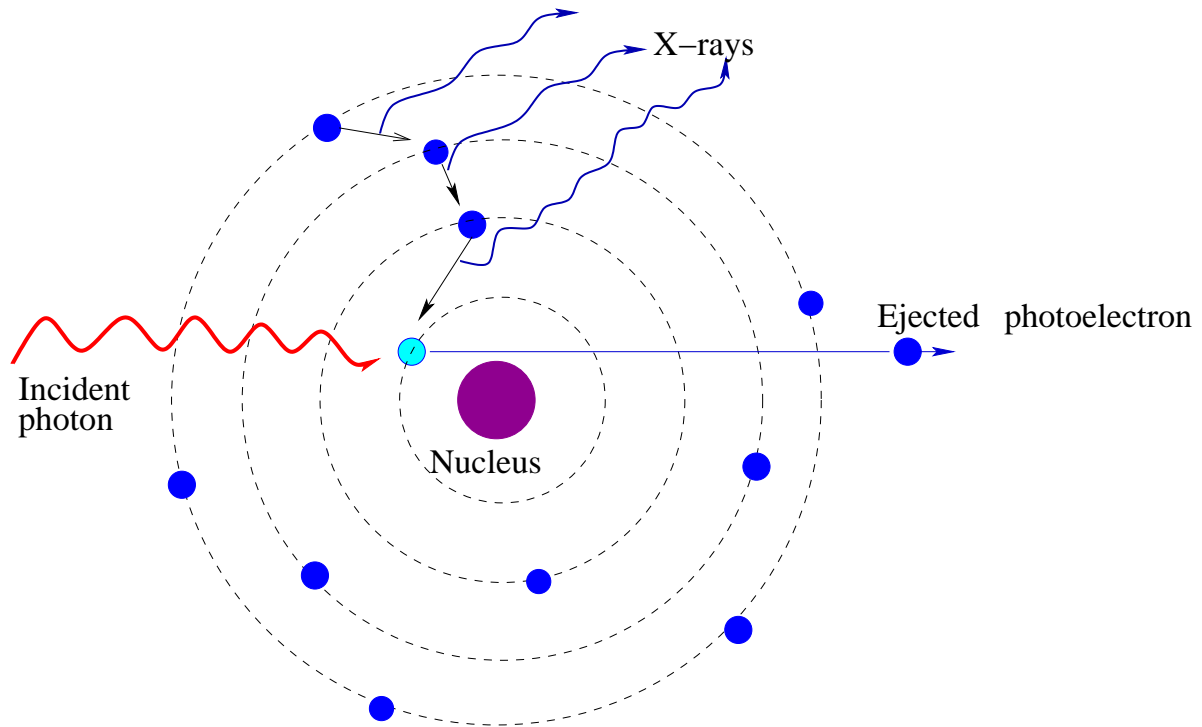


FIG. 3.4. Schematic illustration of photoelectric effect.

where n varies between 4 and 5 [102] and C is a constant. High energy γ -ray can be absorbed by the inner shell electron, thus creating a hole in the inner shell. This hole is quickly filled by an electron from outer shells. Consequently characteristic X-rays are produced and reabsorbed very close to the site of the initial γ -ray interaction (see Fig. 3.4). In some cases X-rays may escape and produce escape peaks which are mostly seen for $E_\gamma < 50$ keV. The energy conservation in this process is expressed as

$$E_\gamma = T_e + B_e, \quad (3.3)$$

where E_γ is the initial γ -ray energy, T_e is the kinetic energy of the photo-electron and B_e is the binding energy of the photo-electron [102].

3.2.2 Compton scattering

In this interaction an incident γ -photon transfers a portion of its energy to atomic electron from the outer shells that can be treated as free because of its very low binding energy. The

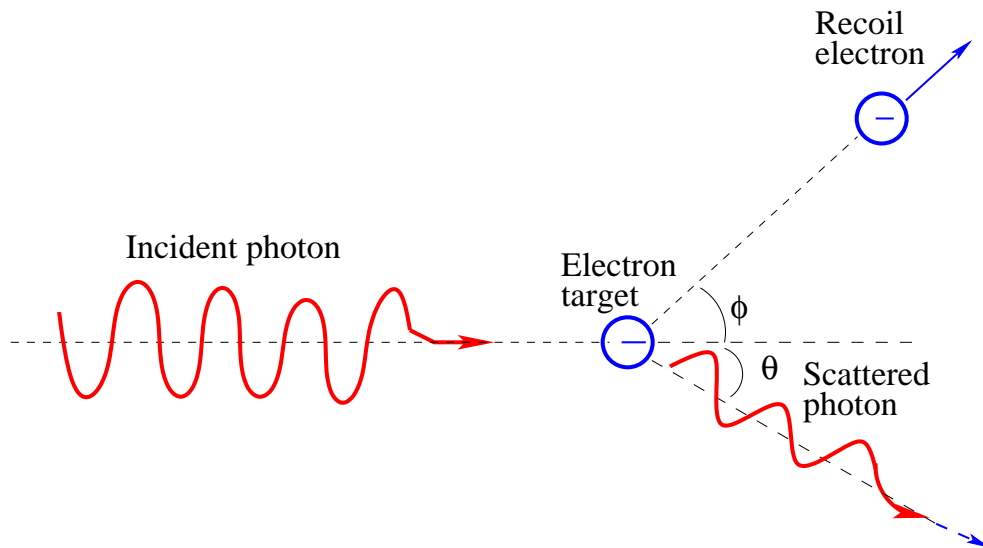


FIG. 3.5. Schematic illustration of Compton scattering.

original photon loses energy and appears as a secondary photon with a different frequency, that is scattered at a certain angle θ (see Fig. 3.5). The Compton scattering formula and the kinetic energy of the scattered electron expressed in terms of θ are respectively given by:

$$E_{\gamma'} = \frac{E_{\gamma}}{1 + (E_{\gamma}/mc^2)(1 - \cos\theta)} \quad (3.4)$$

and

$$T_e = E_{\gamma} - E_{\gamma'} = \frac{E_{\gamma}^2(1 - \cos\theta)}{mc^2 + E_{\gamma}(1 - \cos\theta)}, \quad (3.5)$$

where m is the mass of the electron. The Compton scattering probability decreases with the increase of the energy of the incident γ -ray. This process is a dominant absorption mechanism for γ -ray energies below 8 MeV (see Fig. 3.7).

3.2.3 Pair production

This is a case when the incident photon interacts with the electric field of a nucleus to form an electron-positron pair. This phenomenon is possible with γ -energy exceeding the rest masses of electron and positron, i.e. 1.022 MeV. The excess energy above 1.022 MeV is given as kinetic energy of the pair and as a recoil energy of the nucleus. The positron and

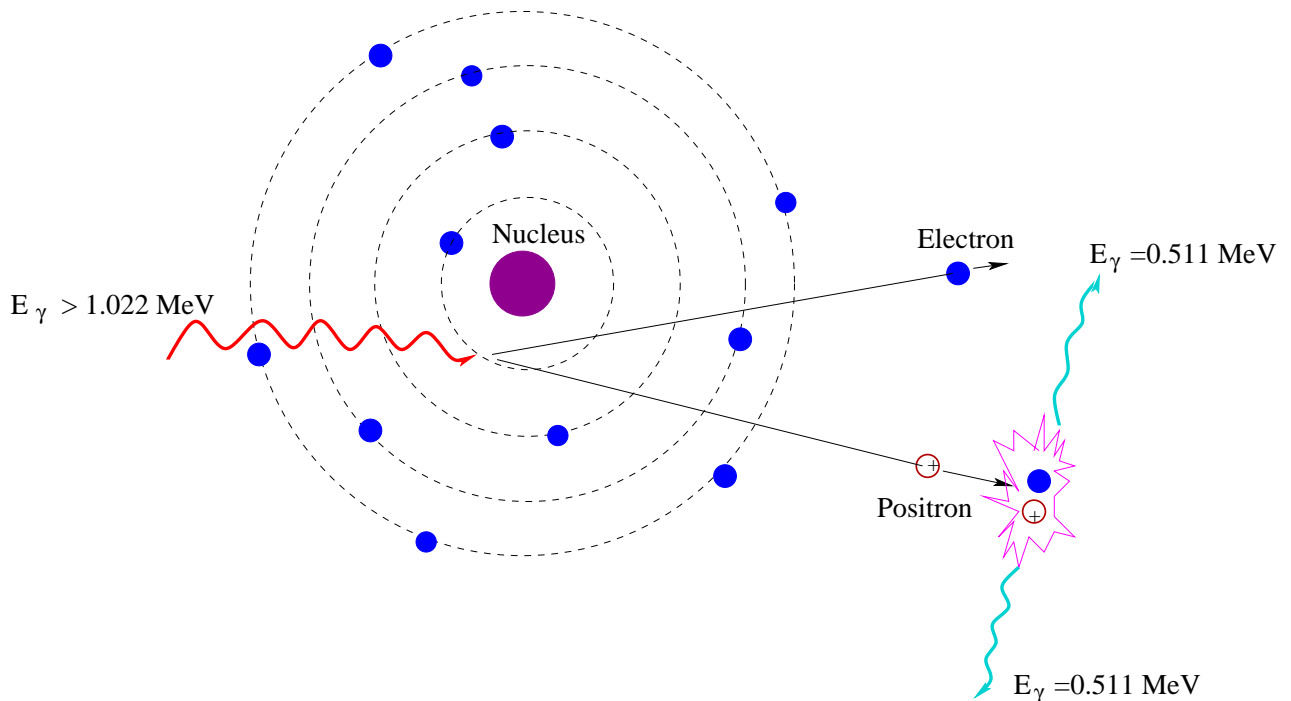


FIG. 3.6. Schematic illustration of pair production.

the electron will slow down. Finally the positron combines with a free electron and the two will annihilate, producing two photons of 0.511 MeV (see Fig. 3.6). If both photons are absorbed in a detector, the full energy of the incident γ -ray will be registered. If one of the two annihilation photons leaves the detector without interaction, the registered energy will be equivalent to $E_d = E_\gamma - 0.511 \text{ MeV}$, which is known as a single escape peak. If the two photons leave the detector without interaction, it will be $E_d = E_\gamma - 1.022 \text{ MeV}$, known as the double escape peak. On the other hand an energy of 0.511 MeV from an annihilation photon may be registered elsewhere.

Fig. 3.7 illustrates the linear attenuation coefficient of a Ge detector for the three γ -interactions. The total coefficient is large at low γ -ray energies due to the photoelectric effect. It considerably decreases at intermediate γ -ray energies and increases again at high energies as the pair production becomes dominant.

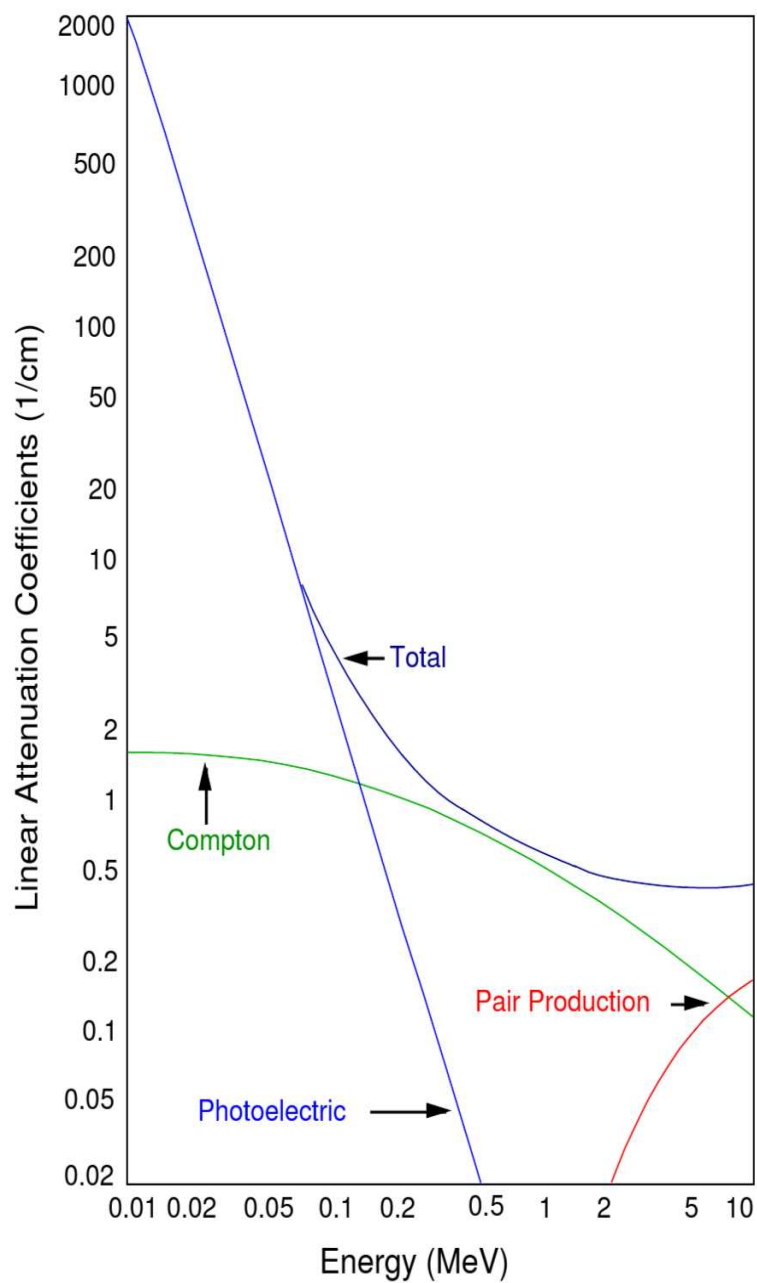


FIG. 3.7. Plot of γ -ray cross-sections for germanium. The Compton scattering covers a wide range of energies. The photoelectric effect takes place mainly at low energies [103].

3.3 Detection and measurements of γ -rays

A photon can be observed by detecting its interactions with matter. In all three fundamental processes of γ -ray interaction with matter, free electrons are generated and slow down on their path through matter. The passage of current creates events such as excited molecular states (scintillating organic crystals), electron-ion pairs (gases) or electron-hole pairs (semiconductors crystals). These charge carriers are used in many photon detectors to determine properties of a photon. The quantity of events generated also depends on factors associated to detector materials. For example the interaction cross-section is proportional to the atomic number of the medium so that detectors with high Z-value are often chosen. The average energy required to produce an electron-hole pair in a Ge semiconductor detector is small (0.7 eV) compared to the energy (30 eV) needed in gas ionization chamber. For γ -ray detection semiconductor detectors (germanium) are commonly preferred as they have a good resolution which is inversely proportional to the square root of the number of carriers generated.

3.3.1 Semiconductor detectors

As the atoms in a crystal are tightly arranged together their states split into energy level groups or bands. Three bands can be identified. A band with unfilled levels (conduction band), a filled band (valence band) and an energy gap (forbidden band). In a conducting solid there is no gap and the two bands (the conduction band and the valence band) are in direct contact so that electrons can easily move to the conduction band. A good insulator is characterised by a large gap such that a large amount of energy is required to move an electron to the conduction band. In a semiconductor the gap is small (see Fig. 3.8) and an electron can move to the conduction band under certain conditions like thermal motion.

A vacancy (hole) in a band is created when an electron moves to another band. That hole will be filled by an electron leaving behind a hole which will also be filled and so on. Thus, One can apply a strong electric field and trigger a simultaneous drift of electrons and holes toward the opposite poles of the field.

Although the crystalline structure always contains some impurities, additional impuri-

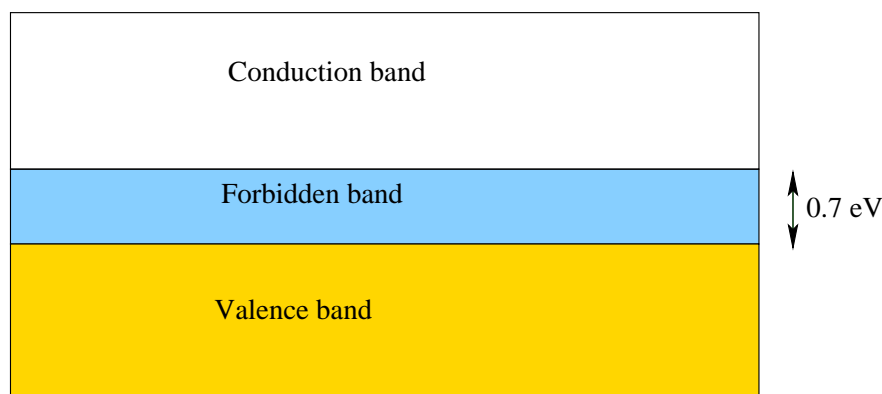


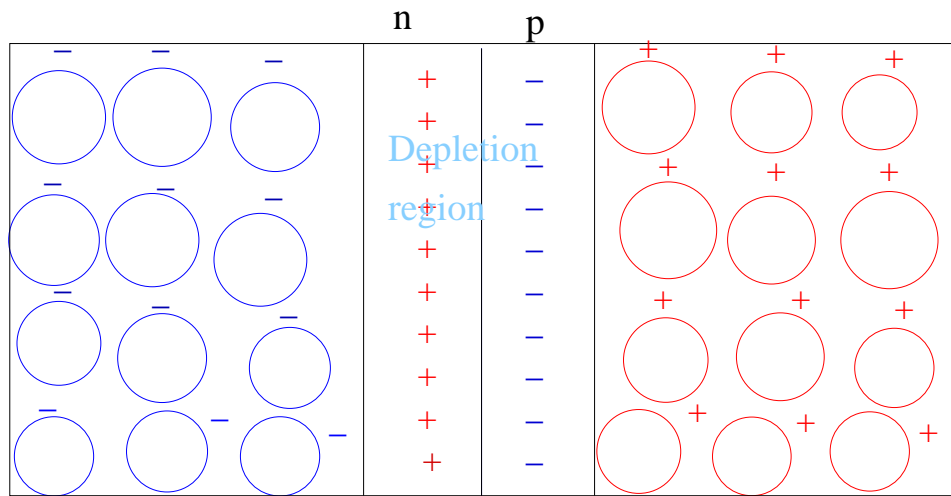
FIG. 3.8. Diagram showing different bands of a Ge semiconductor.

ties are needed for a semiconductor to work under controlled conditions. A material with an excess of outer electrons, known as n-type impurity, allows the extra electrons to be donated to the conduction band and decrease the energy gap. By adding a material with an excess of holes, known as p-type impurity, the holes or acceptors will receive electrons from the valence band. Optimising the amount of both n-type and p-type impurities in a semiconductor can improve the properties of the semiconductor and make it a suitable material for a radiation detector.

However, electrons and holes can be trapped which will cause partial collection of the charges. Fewer energy carriers lead to poor energy resolution. In modern semiconductor detectors the n-type and p-type semiconductors are united in a semiconductor junction where a depletion region is created (see Fig. 3.9). This depletion region is formed by the diffusion of electrons from the n-type material into the p-type material and the one of holes from the p-type material into the n-type material [104].

3.4 High purity germanium (HPGe) clover detectors

In this experiment, nine high-purity germanium clover detectors were used. Each of the nine clovers is made out of four Ge crystals (see Fig. 3.10). The germanium crystal has an electron configuration of $[\text{Ar}] 3d^{10} .4s^2.4p^2$ where the $4p^2$ level is 3 fold degenerate and each atom has two valence electrons free to form covalent bonds with neighbouring atoms. The Ge crystals are of n-type with p-n junction at the outer surface of the detector. This



n-p junction

FIG. 3.9. Illustration of the depletion region.

is where the depletion region is. In order to increase the sensitive volume of the detector and make the charge collection more efficient, the magnitude of the electrical field in the depletion region is increased by operating the Ge clover detectors at high voltage of 2200 V - 3500 V. A γ -ray entering the depletion region (which is usually covering the whole volume of the Ge crystals) creates electrons and holes that move in opposite directions. A signal pulse which is formed by the total number of electron-hole pairs is proportional to the incident γ -ray energy. Ge clover detectors must be kept at low temperature of at least -150° to avoid thermal noise.

Excellent energy resolution is the main factor which makes HPGe detectors the best γ -ray spectrometers. They have also an advantage on linearity over a wide energy range. However, their efficiency is smaller than the efficiency of a scintillator with the same volume, such as BGO, because they have a smaller atomic number. The time resolution of the HPGe detectors is poor which is a consequence of the use of large volume crystals. In addition potential Doppler broadening may decrease the energy resolution of the photo peaks. The Doppler broadening is expressed by:

$$\Delta E_\gamma = E_o \frac{v}{c} \sin(\theta) \Delta \theta \quad (3.6)$$

where E_o is the γ -ray energy, θ is the angle of the detector with respect to the beam axis, v is the velocity of the residual nucleus and c is the speed of light. The peak resolution can be improved using a composite detector that decreases the opening angle $\Delta\theta$. With use of such a detector one needs to implement add-back for improving the photo peak efficiency, and eliminate a part of the Compton continuum background to make the spectrum cleaner.

When measuring γ -ray spectra in Ge-detectors produced in a nuclear reaction where fast neutrons are emitted as outgoing particles, some nuclei of different Ge isotopes (^{70}Ge , ^{72}Ge , ^{73}Ge , ^{74}Ge) undergo inelastic neutron excitation. In addition to the energy of the γ -ray deposited, the recoiling Ge nucleus deposits its energy inside the detector. Thus, in the measured γ -ray spectra, additional peaks resulting from the inelastic neutron excitation appear. These neutron peaks are characterized by a peculiar asymmetric triangular shape of about 40 keV across. In this experiment some neutron peaks were observed the largest being around 596 keV.

Ge detectors can be damaged by radiation when the incident particles cause lattice defects by knocking the atoms out of their normal positions in the crystal lattice. The atom dislocations can result in trapping of the charge, when the electrons or holes are captured near the dislocation. Thus, the charge collection might be incomplete. Such loss of charge has a negative effect on the detector resolution producing low-energy tail on the γ -ray peaks. It was found that a neutron fluence of about $10^{10}n/cm^2$ could totally damage the detector and make it unusable [105].

3.4.1 Compton suppression

Some γ -ray energies can be partially recorded due to Compton scattering, thus creating Compton continuum background. Large background in the spectrum makes the observation of weak peaks more difficult. It is possible to veto some of the Compton scattering events from the HPGe detectors by using bismuth germanate shield (BGO) which is made of scintillating detectors surrounding each HPGe detector (see Fig. 3.11). The energy of the Compton scattered γ -rays from the HPGe detector can be deposited into the BGO. Then the Compton continuum background is reduced by rejecting those γ -rays. In order to prevent detection in the BGO shield of the γ rays which have not scattered from the

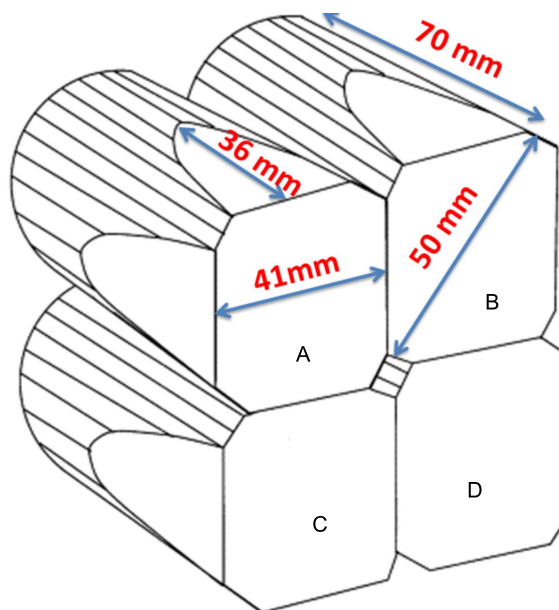


FIG. 3.10. Schematic representation of a clover germanium detector. Figure taken from [106] and modified.

HPGe crystal, heavy metal collimators are placed in front of the BGO detectors. This is important as without such collimators one may veto good events when two γ -rays are detected simultaneously in the Ge crystal and in the BGO shield.

For a monoenergetic γ -ray spectrum, the ratio of counts in the photo peak to the total counts collected (namely peak-to-total P/T) allows to measure the effectiveness of a Compton suppression shield. Often the P/T ratio is measured with ^{60}Co , which has two photo-peaks (1173.2 keV and 1332.5 keV). In this case the P/T ratio is given by percentage of the number of counts in the two photo-peaks divided by the total counts in the whole spectrum. In a standard HPGe detector, it is common to have a P/T ratio at the level of $\sim 20\%$, where only 20% of the counts are in the photo peaks and the remaining 80% are in the background. For a suppressed detector, the P/T can be improved to nearly $\sim 60\%$ [107].

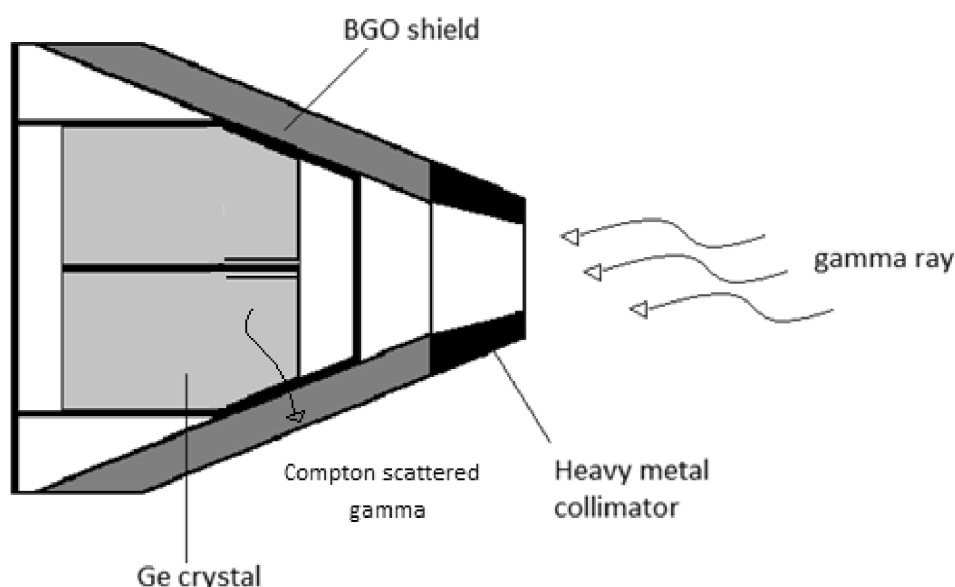


FIG. 3.11. Diagram showing a BGO shield around a clover germanium detector [108].

3.4.2 Absorbers

In some cases the γ -ray spectra show large X-ray peaks. The X-ray might be produced in internal conversion process with a consequent emission of X-ray. Similar effect might be obtained in X-ray fluorescence or when the projectile interacts with the target material and ejects atomic electrons. If a hole in the inner electronic orbit is created in such process it is later filled by an outer electron and a X-ray is emitted. Absorbers are used in order to minimize detection of X-rays, which interact mainly through photoelectric effect. The mass attenuation coefficient is given by

$$\frac{\mu(\lambda)}{\rho} = \frac{N_A}{A} \sigma_{photoelectric} \quad (3.7)$$

where λ is the γ -ray wavelength, ρ is the density of the absorber in g/cm^3 , N_A is the Avagadro's number (6.02×10^{23}), and A is the atomic mass of the absorber. However, too thick absorbers may completely absorb low energy γ -rays. Thus, a balance is needed to minimize detection of X-rays and allow low energy γ -rays to be still observed in the data [102].

In this experiment, X-rays coming from the residual thallium isotopes were observed ($K_{\alpha_1}=70$ keV, $K_{\alpha_2} = 72$ keV and $K_{\beta} = 82$ keV). They are due to internal conversion of K-shell electrons. Detection of X-rays was reduced by placing a 0.15 mm tin (Sn) absorber on top of 0.07 mm brass (copper zinc alloy) absorber. Usually the optimal thickness of absorber is derived from exponential attenuation equation given by:

$$I_x = I_0 \exp(-\mu x) \quad (3.8)$$

where I_x is the desired reduced radiation intensity after γ -rays pass through the absorber, I_0 is the incident radiation intensity, μ is the linear attenuation coefficient of an absorbing material, and x is the thickness.

3.4.3 HPGe detector arrays

A common problem in experiments is the low production yields of many nuclei far from stability. Another challenge is to reduce the influence of Doppler broadening on the energy resolution. The intrinsic energy resolution of a new Ge crystal is typically $\Delta E_{\gamma}^{intr} \leq 0.2\%$ for a 1.33 MeV γ -ray. But, real resolution in an in-beam experiment can change due to Doppler broadening when the residual nucleus recoil out of the target.

HPGe detectors are arranged in arrays in order to maximize the solid angle covered while keeping low probability for coincidence summing. In addition, as a way to increase the photo peak efficiency for high energy γ -rays, the detectors in these arrays have several close-packed HPGe crystals within each cryostat. Thus, if a γ -ray Compton scatters from one Ge crystal to the neighbouring one, the two energies collected from the two crystals can be added. The efficiency of the detector can increase significantly using this add-back technique [109]. The HPGe detector array as used in this experiment will be described in the next section.

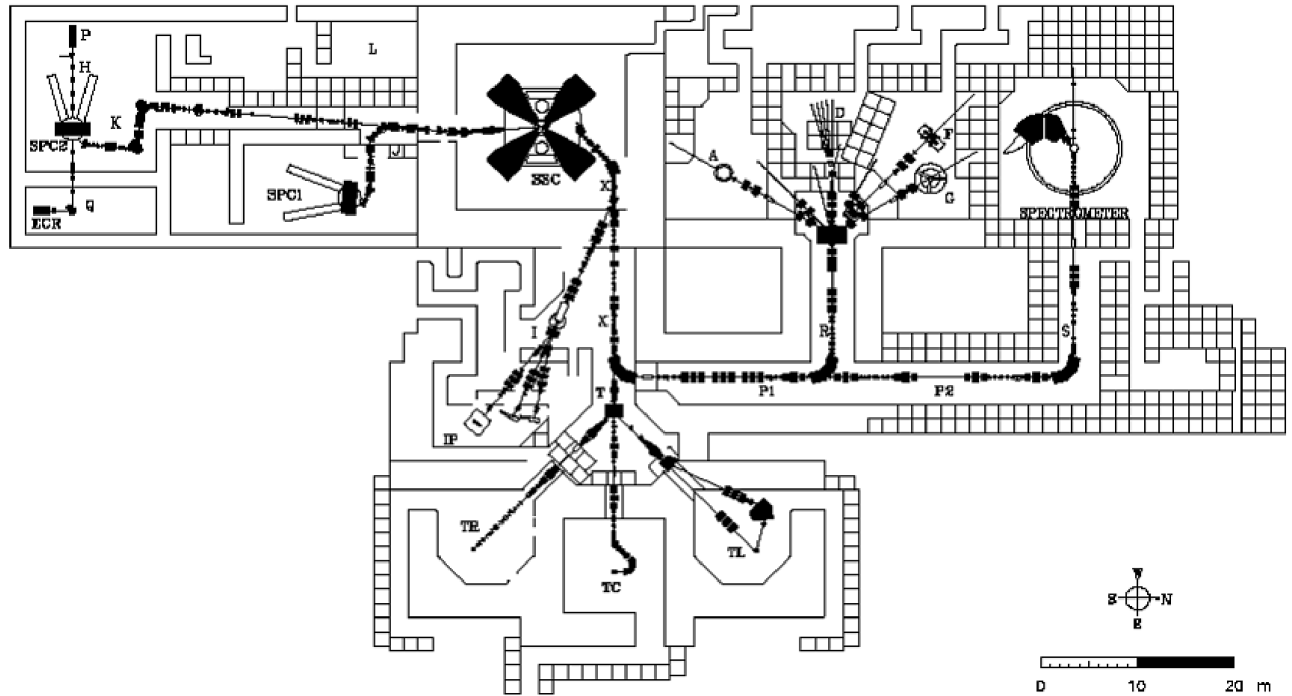


FIG. 3.12. Schematic illustration of the experimental facilities at iThemba LABS [111].

3.5 AFRODITE array

The AFRODITE (AFRican Omnipurpose Detector for Innovative Techniques and Experiments [110]) array is located at iThemba LABS in South Africa. iThemba LABS is a multidisciplinary facility for research and training, which is developing expertise in accelerator based science and technologies. The separated sector cyclotron (SSC) at iThemba LABS provides particle beams used for radioisotope production, proton and neutron therapy and basic nuclear physics research.

The ion beams used for nuclear physics experiments are created with an electron cyclotron resonance ion beam (ECR). The ion beam is first accelerated by one solid-pole injector (SPC2) and then accelerated into SSC to produce the desired beam energy. Finally, the

TABLE. 3.1. Description details for abbreviations used in Fig. 3.13

Abbreviation	Description details
A	Scattering chamber beam line
D	Collimated neutron beam facility
ECR	Electron Cyclotron Resonance Ion Sources
ECD	Electron and Cable Distribution
F	AFRODITE γ -ray spectrometer
G	γ -ray angular correlation table
IP	Isotope Production
L	Low energy experimental area
P	Polarized ion source
SPC1	Solid pole injector cyclotron for light ions
SPC2	Solid ion cyclotron for heavy and polarized ions
SSC	Separated Sector Cyclotron
TC	Isocentric system for neutron therapy
TR	Horizontal beam line for proton therapy
TL	Isocentric proton therapy

beam is transported through the X and P beam lines towards the AFRODITE array in the experimental vault F (see Fig. 3.12 and Table. 3.1).

The AFRODITE array (see Fig. 3.13.) with 16 detector positions, is made up of two types of high purity Ge detectors, namely clover detectors and LEPS (Low Energy Photon Spectrometers) detectors. In the experiments performed in this work, only clover detectors were used. Detectors can be mounted around the target chamber at three different angles with respect to the beam direction (45° , 90° , 135°). The target chamber has aluminium windows. Inside the target chamber there is a target ladder which has four positions (two target slots, one slot for an empty frame and a slot for the viewer to focus the beam). It can move up and down such that one of the four slots is placed in front of the beam. Focusing is optimized first with a small beam intensity (often of ~ 0.5 nA) through the viewer. We also check that all beam intensity ends on the beam dump. Then the beam intensity is increased up to the optimal level for the experiment using an empty frame. To ensure that there is no halo the counts with and without beam should be approximately equal.

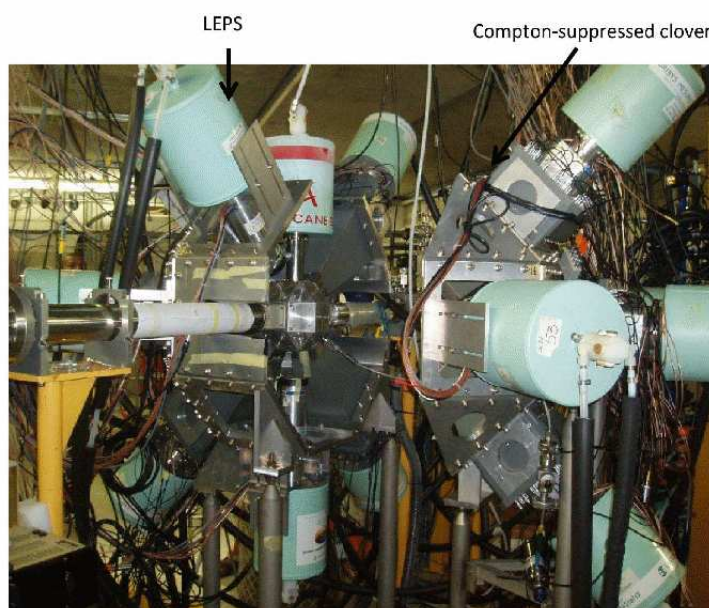


FIG. 3.13. AFRODITE array with HPGe clover detectors and LEPS.

3.6 Basic ideas of electronics

Measurements for nuclear spectroscopy require an appropriate data acquisition system. Important developments have been made in recent years with the transition from analog data acquisition systems to modern digital systems. The traditional analog approach is relatively not effective at high counting rates, mainly due to the high dead time that paralyses the system. In order to optimize the performance, a new digital processing system was introduced. In contrast to analog systems, the detector signals are digitized directly after the preamplification stage. Next subsections explain different stages for detector signal processing. The analog and the digital acquisition systems have been used in the first and second experiments respectively. Data with better statistics could be produced using the digital acquisition system.

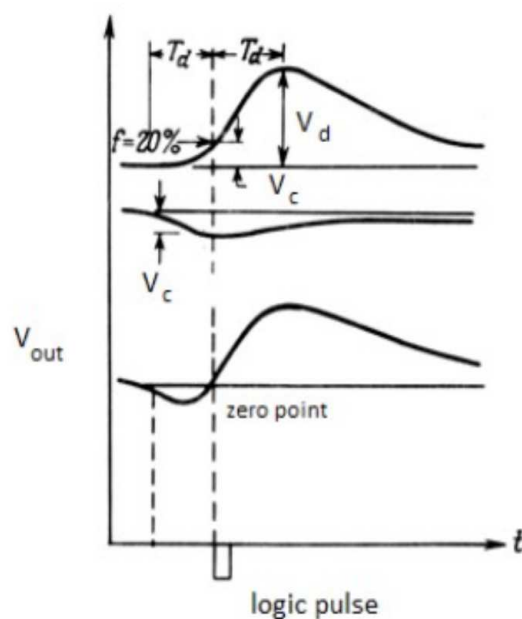


FIG. 3.14. Illustration of the pulse splitting using the CFD [114].

3.6.1 Analog electronics

The process to extract energy information using analog electronics has three main phases involving three electronic devices: preamplifier, amplifier, and Analog to Digital Converter (ADC) respectively. When γ -radiation interacts with a detector it creates a number of excitations, which produce an observable charge pulse proportional to the incident γ -ray energy deposited into the detector. The charge pulse created within a Ge detector is too weak to be processed directly. Thus, the detector has a built-in preamplifier composed of a Field Effect Transistor and a feedback loop which integrates the charge pulse and converts it into a voltage pulse. The pulse is then passed through a pre-amplifier to increase the amplitude. The output voltage pulse has a fast rise time and a large exponential decay time ($\sim 50 \mu s$). Its amplitude is proportional to the energy of the incident radiation but the pulse shape and the leading edge of the signal are too sharp to be converted with good precision into energy by the ADC. In addition, the large decay time of the voltage pulse can cause pile-up of different signals. Thus, a spectroscopy amplifier is required which converts the detector output into signal with quasi-Gaussian shape that is fed in the ADC.

Finally, the ADC evaluates the amplitude of the quasi-Gaussian shape and then converts it into a digital number which is proportional to the γ -ray energy [112, 113].

The time when the radiation is detected is needed for coincidence measurements that are crucial to construct the level scheme. Timing is based on generation of logic pulses whose leading edge indicates the time of the input pulses occurrence. A logic pulse is created only if the detector signal passes a set threshold level. However, two problems may arise when generating the logic pulse. Two incident pulses with different amplitudes and/or rise times can cause the discriminator to trigger at different times while the two pulses are exactly coincident. This problem is known as amplitude walk. Another problem known as time jitter is due to noise and statistical fluctuations in the detector signal that can result in timing fluctuations and consequently two coincident signals may trigger at different times. These problems are minimized using a Constant Fraction Discriminator (CFD). The incoming pulse is split into two parts V_d and V_c . V_d is delayed by a time T_d and V_c is inverted and attenuated by a factor f . Both f and T_d are optimized for best time resolution with minimum amplitude walk and time jitter. The start time of the logic pulse will be the zero crossing of a bipolar pulse which is formed by a sum of the pulses V_d and V_c (see Fig. 3.14) [114].

Both the energy and time are registered and monitored by the electronics built in RIS clover modules [113]. Further processing such as data sorting, construction of spectra and various matrices is performed via the MIDAS software package.

3.6.2 Digital electronics

Techniques for measurement of the γ -ray energy using digital electronics consist of digitizing the pulse signal directly after the preamplification stage. The ADC of the digital electronics converts the detector output into a string of discrete values. These values are passed through a trapezoidal filter. The values of the filter are obtained by taking a sum over the values of the pulse within certain length (L) and subtract it from the sum over the values of the pulse for the same length after a certain gap (G) (see Fig. 3.15). Summing and subtracting throughout the waveform of the signal results in a trapezoidal form with a height proportional to the amplitude of the input pulse and thus to the γ -ray energy

(see Fig. 3.15). The trapezoidal filter output is continuously updated in the DGF (digital gamma finder) Pixie 16 [115].

Time properties associated with the incident γ -ray energy are deduced based on the fast trapezoidal filter and a threshold set by the user. The fast trapezoidal filter follows the same algorithm as the slow trapezoidal filter, but with smaller values for L and G . The start time is deduced when the fast filter crosses the set threshold (see Fig. 3.15). Crossing the threshold corresponds to the appropriate time to start counting the sampling time at the end of which the value of the flat top of the slow filter is measured. For clovers typical values for the slow filter are $L_s = 4 \mu s$ and $G_s = 1 \mu s$ while for the fast filter they are $L_f = 0.1 \mu s$ and $G_f = 0.1 \mu s$.

In order to avoid pile-up, two pulses must be separated by at least a time interval equal to the slow filter rise-time plus the flat top width. Thus, whether pulses suffer pile-up depends critically on the rise-time of the filter being used. The amount of pile-up which occurs at a given average signal rate will increase with longer rise-times. Since the fast filter rise-time is very short, the Pixie - 16 can test for slow filter pile-up by measuring the fast filter for interval PEAKSEP (a value governing the minimum time separation between two pulses) after a pulse arrival time. If no second pulse occurs in this interval PEAKSEP, which is usually set to a value close to the slow filter rise-time plus flat top width, then there is no slow filter pile-up. The piled up pulses are rejected.

The digital signal processor (DSP) reads out and formats the energy and time records before they are written to external memory for later analysis [115, 116].

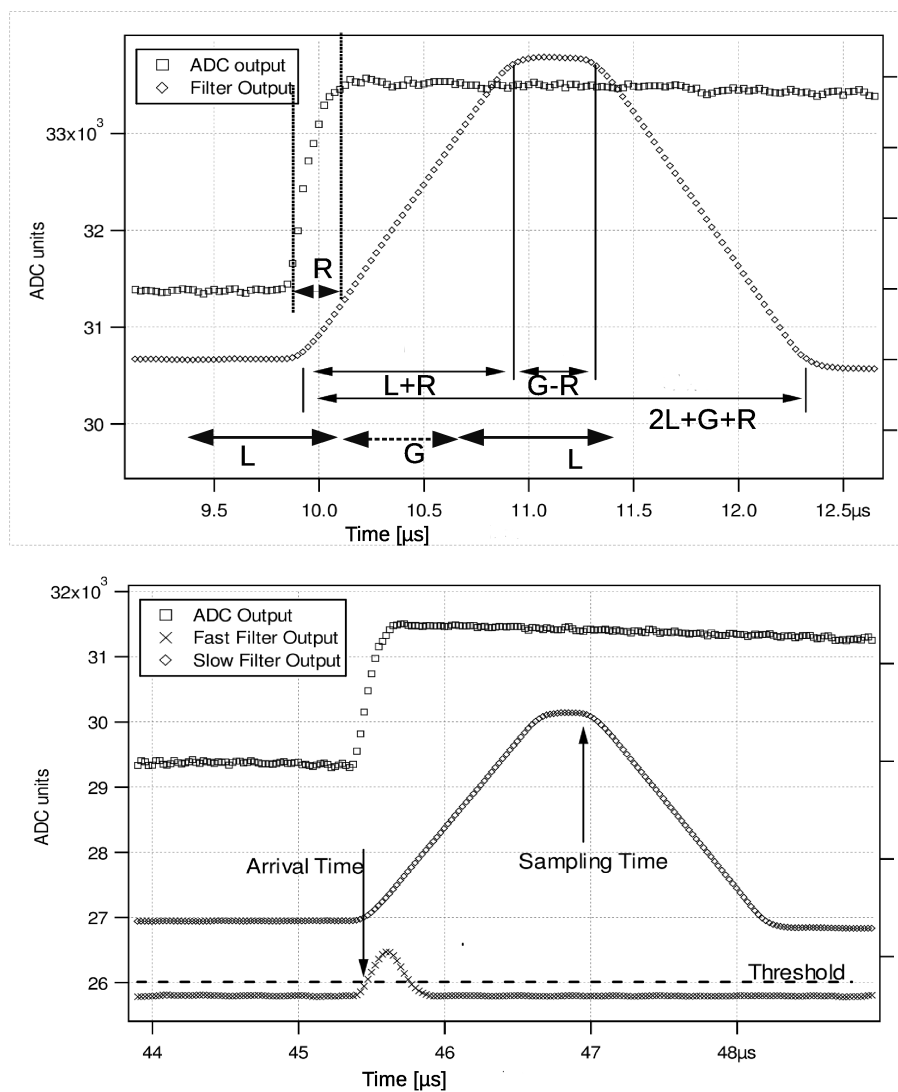


FIG. 3.15. Illustration of the fast trapezoidal filter for arrival time (bottom panel) and the slow trapezoidal filter for the γ -ray energy (top panel). Modified figure that was taken from [115].

3.6.3 Threshold and pole zero adjustment

To avoid recording noise with digital electronics an electronic level which is called threshold is adjusted such that it is not too high to avoid excluding the detection of low-energy γ -rays and not too low to let much noise coming through. The threshold adjustment results in minimizing collection of unwanted events and thus increases computer time to process the events of interest.

Threshold level is also required in radiation measurements with analog electronics. It was manually adjusted by fine tuning the threshold on the CFD and examining on an oscilloscope the output pulse produced by γ -rays emitted by ^{152}Eu .

Pole zero adjustment is also a necessity with analog electronics since settings of electronics may change with time due to many factors like temperature fluctuations, intrusive factors such as turning equipment on and off and moving detectors around. In fact, the tail of the semi-Gaussian signal from the amplifier can undershoot (below the zero baseline) or overshoot (above the zero baseline). This can affect the amplitude of a signal produced within the under/over shoot region of a proceeding signal, and consequently the detected γ -ray energy. Therefore the pole zero needs to be correctly adjusted to bring the right hand side of the signal peaks to the zero baseline and then make correct γ -ray energy measurement.

3.6.4 Time window and trigger condition

Coincidence measurements were performed with a coincidence window set to 150 ns for all detectors. Coincidence window corresponds to the required period of time within which the logic signals from γ -rays hitting other detectors should arrive. This time was chosen to prevent random coincidences summing where γ -rays from the decay of two different nuclei produced within different beam pulses may arrive within the coincidence window and be considered as belonging to the same nuclear reaction. Probability of random coincidences decreases by decreasing the coincidence window. However, a too short coincidence window can cause a loss of efficiency to detect low energy transitions which demand longer time for charge collection. In addition, time resolution induces a normal distribution of the time difference between two correlated events. Therefore, the smaller the time window the

larger the chance of finding two correlated events outside the window.

Trigger, which counts signal pulses in a specific time window and validates the event if the required condition is met, is also a necessity. In these experiments the trigger selected at least two γ -rays within the time window, i.e. a minimum of two detectors had detected γ -rays from the same decay path, each γ -ray entering a detector within the coincidence window.

3.7 Data analysis procedures

3.7.1 Set of programs for data analysis

Data analysis requires a set of programs. A sort code (MT sort) was compiled and executed for sorting spectra and matrices. The sorted data were then analysed with the Radware software package [117], which is specifically designed for γ -spectroscopy studies.

3.7.2 Energy calibration and gain matching

The data are sorted with respect to each clover element in the AFRODITE array. However, the clovers have different gains. In order to avoid mismatching in the spectra, all clover detectors were gain-matched and calibrated to the same energy relationship of $N = 2E_\gamma$, where N is the channel number and E_γ is the γ -ray energy in keV. A radioactive source (^{152}Eu), with known γ -ray energies was used. Each weekend the ^{152}Eu source was placed in front of the detectors to collect data for about 30 minutes. The relation between γ -ray energies from the source and the gain-matched spectrum is parametrized using the following equation

$$kE = ax^2 + bx + c = N \quad (3.9)$$

where a , b , and c are the gain matching coefficients, x is the channel number in the spectrum of the source peak with energy E , N is the channel number of this peak in the gain matched spectrum. k was chosen as $k = 2$, meaning that the gain matched spectrum has a gain of 0.5 keV/channel. Since a is very small, only b and c are usually considered.

A few programs were run to produce gain matching coefficients for each clover crystal. The energy histograms from the ^{152}Eu source were saved and then converted to ascii format (.dat files). Using a fitting program, as many peaks as possible were fitted extracting centroids, areas, and χ^2 . With the energy values and centroids, a calibration program was run to produce a set of gain matching coefficients for each clover element. Good calibration E_{cal} is achieved when the measured energy (E_m) and E_{cal} are almost equal, with a difference of less than 0.1 keV.

3.7.3 Doppler shift correction

If γ -rays of decaying excited states are emitted in flight when the excited nucleus recoils from the target with velocity v , the observed γ -ray energy E_s is Doppler shifted depending on the detector angle and the recoil velocity (see Fig. 3.16). In this case Doppler shift correction is required. The Doppler shift energy is expressed as

$$E_s = E_0 \frac{\sqrt{1 - \frac{v}{c}}}{1 - \frac{v}{c} \cos \theta} \approx E_0 \left(1 + \frac{v}{c} \cos \theta\right) \quad (3.10)$$

where E_0 is the γ -ray energy in the rest-frame.

A broadening in the Doppler shift energy will appear following a finite opening angle $\theta + \Delta\theta$ of the germanium crystal that measures the γ -ray energy. For each crystal of the clover detectors of the AFRODITE array $\Delta\theta = 5^\circ$. If two Ge crystals (placed at two different angles θ) in the same clover detector are hit simultaneously $\Delta\theta = 10^\circ$. The Doppler broadening can be approximated by differentiating equation (3.10) which gives

$$\frac{dE_s}{d\theta} \approx \frac{\Delta E_s}{\Delta\theta} \approx E_0 \frac{v}{c} \sin \theta. \quad (3.11)$$

When including the broadening due to recoil velocity, it is

$$\Delta E_s \approx E_0 \cos \theta \frac{\Delta v}{c} - E_0 \frac{v}{c} \sin \theta \Delta\theta. \quad (3.12)$$

A Doppler correction program was used to correct the gain matched energies for Doppler shifts, thus producing a new set of gain matching coefficients.

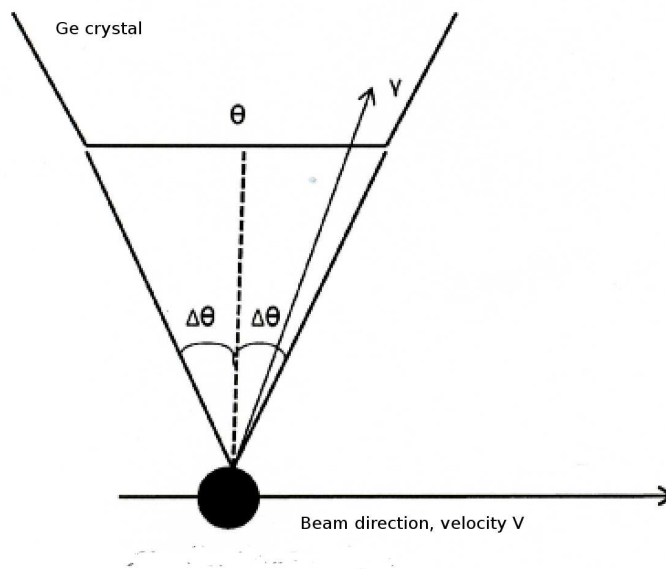


FIG. 3.16. Schematic representation of the detector opening angle and the recoil velocity causing the Doppler broadening of the detected γ -rays. Figure taken from [58].

3.7.4 Gain drift correction of the energies

Gain drifts of the clover detectors may occur during experiment due to temperature fluctuations. They are typically less than 1 keV for low energy peaks and about up to 2-3 keV for high energy peaks. The gain drifts correction was performed referring to gain matching of the detectors as a function of time.

3.7.5 HPGe clovers and add-back procedure

One advantage of the use of HPGe clovers is the possibility to recover additional photo-peak events by summing γ -ray interactions in different crystals [118]. It is possible that γ -ray scatters from one crystal to another in the same HPGe clover. Depending on scattering probability, a range of add-back schemes is suggested for summing and no summing. If two neighbouring crystals are fired horizontally or vertically, i.e AB, CD or BD, AC (see Fig.3.10.), the signals are added. Cases of diagonal scattering (AD or BC) and triple hits are not accepted since they probably do not originate from the same γ -ray.

3.7.6 $\gamma - \gamma$ matrix construction

In a γ -ray experiment, each nucleus in a sample of excited nuclei decays by emitting a cascade of consecutive γ -rays until it reaches its ground state. A useful technique in coincidence measurements is to produce and analyze γ - γ matrix which is a two-dimensional E_{γ_1} and E_{γ_2} energy histogram with the energy of one photon on one axis and the energy of a coincident photon on the other axis, i.e. X- and Y-axes respectively. The coincidence counts are incremented on the Z-axis (see Fig. 3.17). The matrix is symmetric with respect to X- and Y-axes since for each γ -ray pair of E_{γ_1} and E_{γ_2} coincidence counts are incremented for both $(E_{\gamma_1}, E_{\gamma_2})$ and $(E_{\gamma_2}, E_{\gamma_1})$.

3.7.7 Gating

Gating is a way to know all the γ -rays which are in coincidence with a γ -transition of interest. In practice gating on a transition is performed by taking a slice of the $\gamma - \gamma$ matrix, which refers to a coincidence spectrum that is obtained by selecting a narrow window around a peak on X-axis and projecting out the one dimensional γ -ray spectrum on the remaining Y-axis. Gating on different photo peaks of interest allows to place the γ -ray transitions in the level scheme. For example the level scheme shown in Fig. 3.18 shows five levels and five transitions with energies E_{γ_1} , E_{γ_2} , E_{γ_3} , E_{γ_4} and E_{γ_5} . A spectrum gated on E_{γ_1} will show the γ -rays that belong to the decay paths passing through γ_1 , i.e. E_{γ_5} , E_{γ_2} and E_{γ_4} . Gate on E_{γ_2} will show E_{γ_1} . The spectrum gated on E_{γ_4} will show E_{γ_5} , E_{γ_3} and E_{γ_1} , and so on. Based on the number of conditions determined from the analysis of the gated spectra obtained in a γ -coincidence experiment, the level scheme of a nucleus can be built.

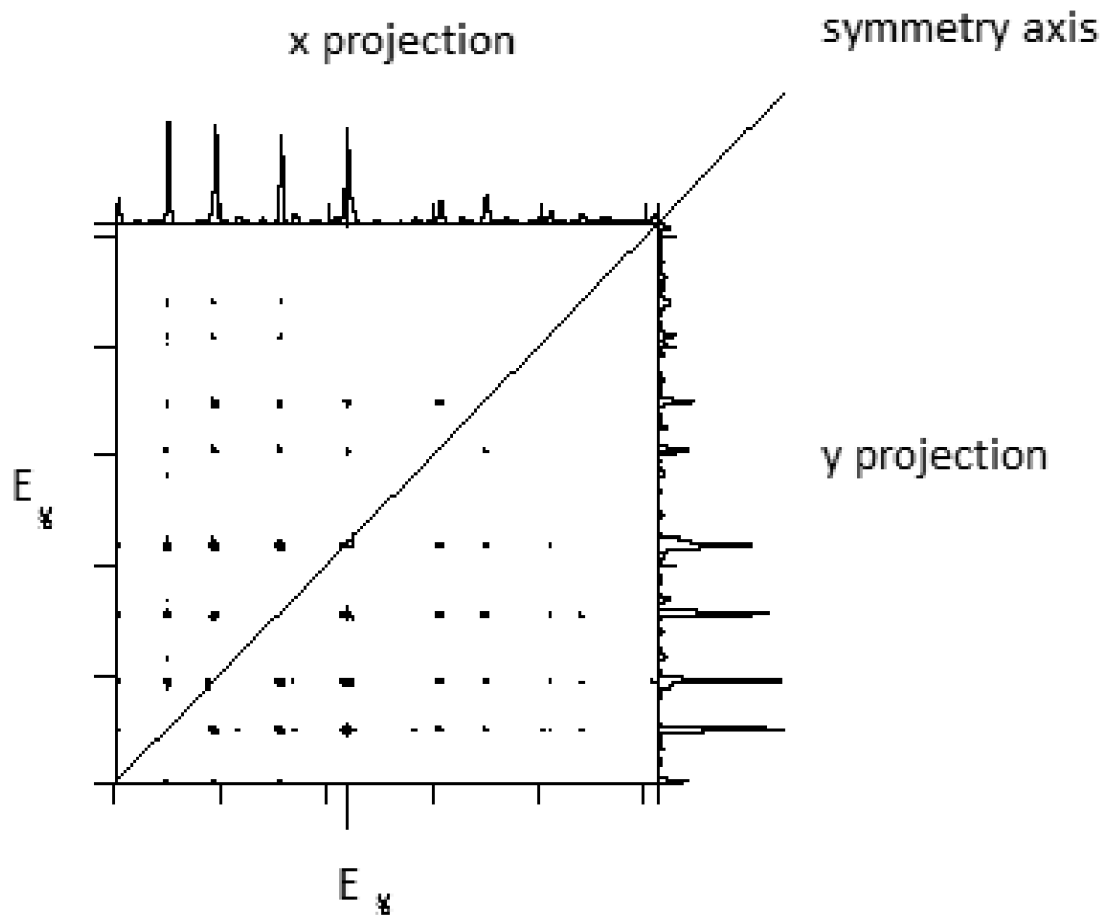


FIG. 3.17. Plot of γ - γ matrix illustrating the coincidence events on X and Y-axis. Dots illustrate counts being incremented on Z-axis [119].

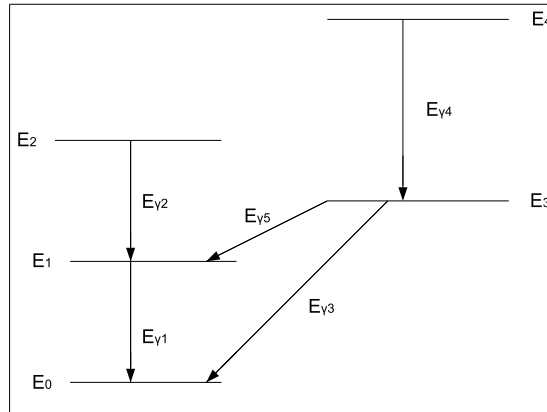


FIG. 3.18. Example of a simple level scheme.

3.7.8 Spin and parity measurements

After constructing the level scheme, the spin and parity assignments of the energy levels were performed by analyzing the angular distribution ratios and the linear polarisations of the emitted γ -rays.

i) Spin measurement

For fusion evaporation reactions the intensity of the γ -rays emitted in different directions in space obeys an angular distribution which is given by:

$$W(\theta) = \sum_{k=even} \alpha_k A_k(J_i, L_1, L_2, J_f) P_k(\cos \theta), \quad (3.13)$$

where $P_k(\cos \theta)$ are the Legendre polynomials. A_k are the angular distribution coefficients which are theoretically calculated. They depend on the initial and final spins J_i and J_f respectively, on the multiple order of the radiation L_1 and $L_2 = L_1 + 1$, and the mixing ratio δ if the transition is mixed. α_k are attenuation coefficients having values between 0 and 1. They are expressed as a function of the distribution parameter (σ/J) (see Fig. 3 in Ref. [120]), where σ is the Gaussian parameter of the alignment of the nuclear state and

J is its spin [120]. The angular distribution coefficients are given by:

$$A_k(J_i L_1 L_2 J_f) = \frac{1}{1 + \delta^2} \{f_k(J_f L_1 L_1 J_i) + 2\delta f_k(J_f L_1 L_2 J_i) + \delta^2 f_k(J_f L_2 L_2 J_i)\}, \quad (3.14)$$

where

$$f_k(J_f L_1 L_2 J_i) \equiv B_k(J_i) F_k(J_f L_1 L_2 J_i). \quad (3.15)$$

F_k and $B_k F_k$ are given in nuclear tables [120]. Measuring γ -ray intensity at different angles allows the multipolarities to be distinguished by analyzing the angular distribution ratios. The angular distribution function $W(\theta)$ for pure stretched dipole and quadrupole transitions are shown in Fig. 3.19.

In these experiments, the AFRODITE array comprised 4 clovers at 135° and 5 clovers at 90° . For a certain γ_2 -ray transition that is in coincidence with γ_1 -ray, the theoretical angular distribution ratio is given by:

$$R_{AD}^{th} = \frac{W(135^\circ)}{W(90^\circ)}. \quad (3.16)$$

It can be compared with the experimentally measured angular distribution ratio

$$R_{AD}^{exp} = \frac{I_{\gamma_2}(135^\circ) \text{ gated on } \gamma_1 \text{ in all detectors}}{I_{\gamma_2}(90^\circ) \text{ gated on } \gamma_1 \text{ in all detectors}}, \quad (3.17)$$

where $I_{\gamma_2}(135^\circ)$ and $I_{\gamma_2}(90^\circ)$ are respectively the intensity of γ_2 at 135° and 90° from the spectrum gated on γ_1 . Since the dependence of the efficiency from the γ -ray energy is approximately the same at 135° and 90° , the angular distribution ratio can be given by:

$$R_{AD}^{exp} = \frac{A_{\gamma_2}(135^\circ) \text{ gated on } \gamma_1 \text{ in all detectors}}{A_{\gamma_2}(90^\circ) \text{ gated on } \gamma_1 \text{ in all detectors}} \cdot C, \quad (3.18)$$

where A_{γ_2} is the area of the peak of γ_2 , and C is a coefficient representing the ratio of the number of working detectors at 90° and 135° with respect to the beam axis.

$R_{AD}^{th} = 0.85$ for pure stretched dipole and $R_{AD}^{th} = 1.35$ for pure stretched quadrupole transitions. They are obtained, assuming that $\sigma/I = 0.3$, which is in agreement with the experimental angular distribution of E2 transition. This leads to attenuation coefficients $\alpha_2 = 0.75$ and $\alpha_4 = 0.4$ respectively.

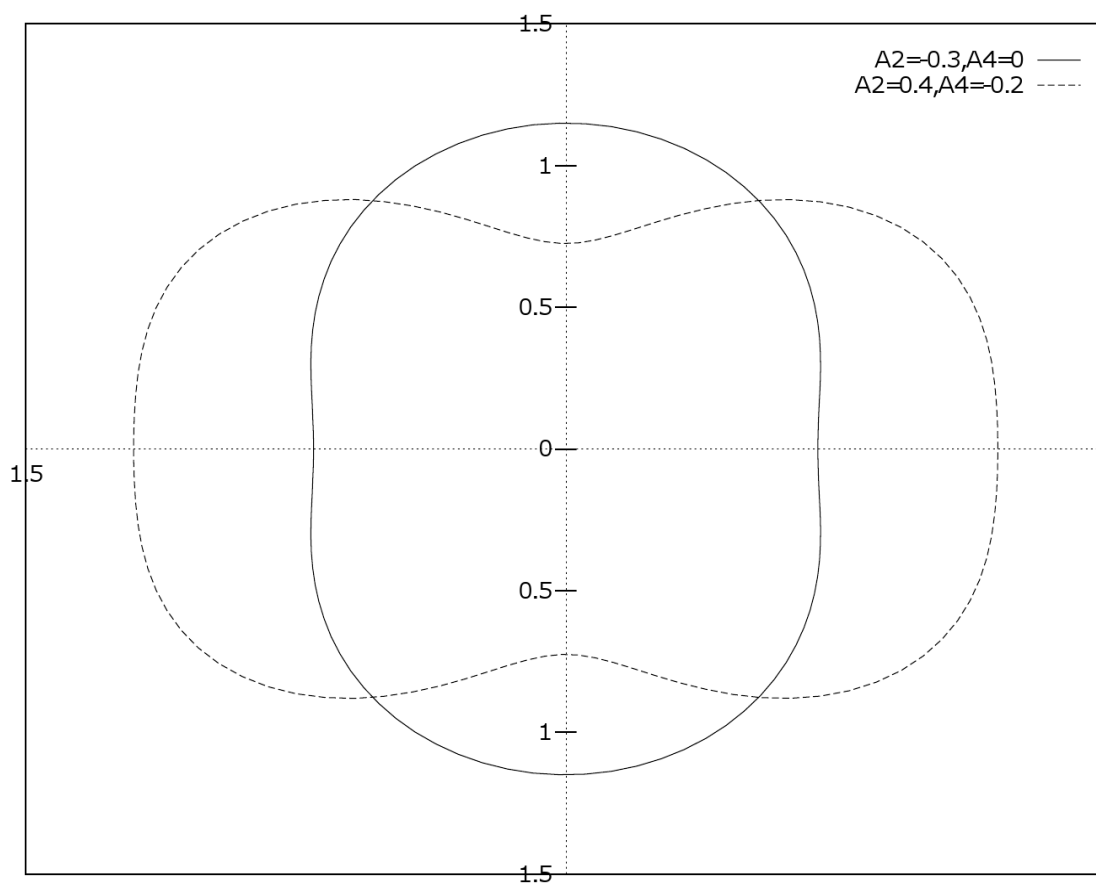


FIG. 3.19. Plot illustrating the angular distribution function $W(\theta)$ as a function of the angle θ for $I \rightarrow I - 1$ dipole transition (solid line) and $I \rightarrow I - 2$ quadrupole transition (dashed line). $\theta = 0^\circ$ corresponds to the positive x-axis. Figure taken from [58].

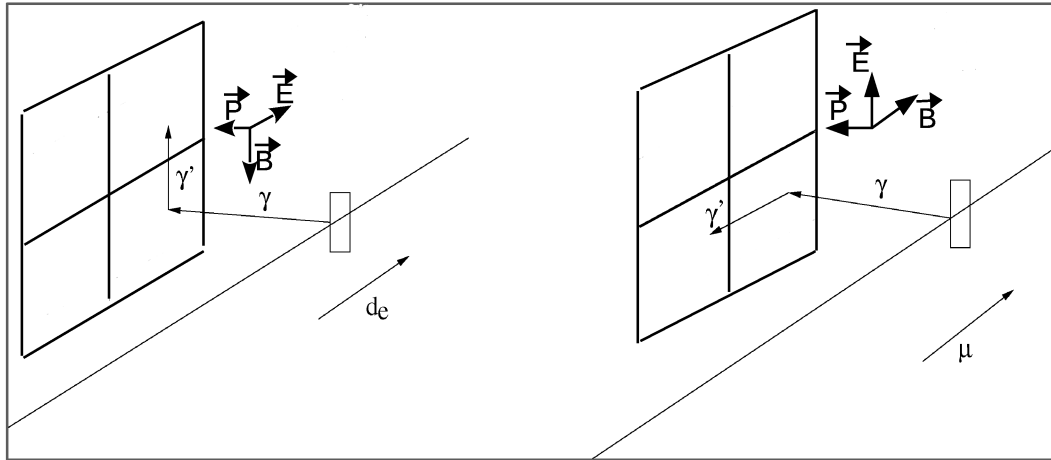


FIG. 3.20. Compton scattering in a clover detector for stretched electric (left panel) and magnetic (right panel) dipole transition.

ii) Parity measurement

In order to determine whether the radiation is electric or magnetic in character, linear polarization measurements are performed. A fraction of the γ -rays that hit a crystal of a clover detector Compton scatters into another crystal where they are absorbed. This is known as a double hit event. As these γ -rays have larger probability to scatter perpendicular to their electric field vector \vec{E} , one can determine an electric or magnetic nature of the transition by knowing the Poynting vector \vec{P} which is a directional vector of the electromagnetic energy and measuring the direction of \vec{E} from the number of double hit events scattered vertically and horizontally (see Fig. 3.20). The polarization anisotropy is expressed as:

$$A_p = \frac{N_V - \varepsilon N_H}{N_V + \varepsilon N_H}, \quad (3.19)$$

where N_V and N_H are the number of double-hit events scattered in vertical and horizontal direction respectively, and ε is the relative efficiency of the detector crystals (typically very close to 1).

Experimental measurement of the linear polarization anisotropy can be performed using horizontal and vertical polarization γ - γ matrices, where horizontally or vertically scattered γ -rays are located on one axis and γ -rays from all the detectors on the other axis. Setting

gates on γ -ray transitions in the two matrices on the axes of all detectors, the polarization anisotropy A_p is calculated:

$$A(E_\gamma) = \frac{I_v(E_\gamma) - I_h(E_\gamma)}{I_v(E_\gamma) + I_h(E_\gamma)}, \quad (3.20)$$

where I_v and I_h are the intensities of vertically and horizontally scattered γ -rays of energy E_γ , respectively. A_p has positive sign for stretched electric transitions and negative for stretched magnetic transitions [115].

3.7.9 Measurement of γ -ray relative intensities

γ -ray intensities are essential to deduce the transition probabilities. In addition to coincidence analysis for the level scheme construction, γ -ray intensities can support arguments for the ordering of the transitions.

γ -ray intensity determination is made with gated coincidence spectra which are fitted to obtain the area of the peaks and their corresponding uncertainties. The γ -ray intensity is given by:

$$I_\gamma = \frac{A_\gamma}{\varepsilon_\gamma} \quad (3.21)$$

where A_γ is the area of the γ -ray peak and ε_γ is the efficiency of the array for the γ -ray of interest. The efficiency as a function of energy in our experiment is shown in Fig. 3.22. It was obtained with data from ^{152}Eu and ^{133}Ba sources and using a few Radware programs. Peaks from the two spectra were fitted and areas were saved. Then EFFIT program was used to fit the efficiency curve with:

$$\varepsilon_\gamma = [(A + Bx + Cx^2)^{-G} + (D + Ey + Fy^2)^{-G}]^{1/G}, \quad (3.22)$$

where A , B , C , D , E , F , and G are coefficients and $x = \log \frac{E_\gamma}{100}$ and $y = \log \frac{E_\gamma}{1000}$, with E_γ in keV.

The total transition intensity, I_t is given by:

$$I_t = (1 + \alpha)I_\gamma, \quad (3.23)$$

where α is the internal conversion coefficient. The internal conversion coefficient can be found from the ESCL8R programme or from the ICC online programme [121-123]

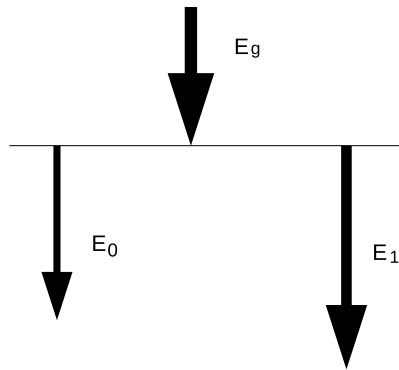


FIG. 3.21. Schematic illustration of the intensity measurement with normalization correction. Intensity is measured from above at the gate on the energy transition E_g

If γ -ray intensity of a transition of interest is measured in two different gated spectra, different values will be obtained. Thus, in principle all γ -ray intensities should be measured from the same gated spectrum. In some cases this is not possible the measured intensity (from a different gate) should be normalized. For instance (see Fig. 3.21.), normalization of the measured intensity from a gate E_g can be performed as follows. Assume that the intensity I_0 of the transition E_0 is already measured from a gate below. Then the intensity I_1 of the transition E_1 when measured in the same gate will be

$$I_1 = I_0 \frac{I'_1}{I'_0}, \quad (3.24)$$

where I'_1 and I'_0 are the intensities of E_1 and E_0 , when measured in the spectrum gated on E_g .

3.7.10 Identification of isomers using the Recoil Shadow Anisotropy Method (RSAM)

Intensity of transitions is affected by the presence of isomers in the nanosecond range. The detection of γ -rays emitted by recoiling nuclei can be affected by the collimator shadows on the different elements of the clover detectors (see Fig. 3.23). The shadow effect can be used to indicate the delayed transitions and to identify the isomeric levels in the level scheme.

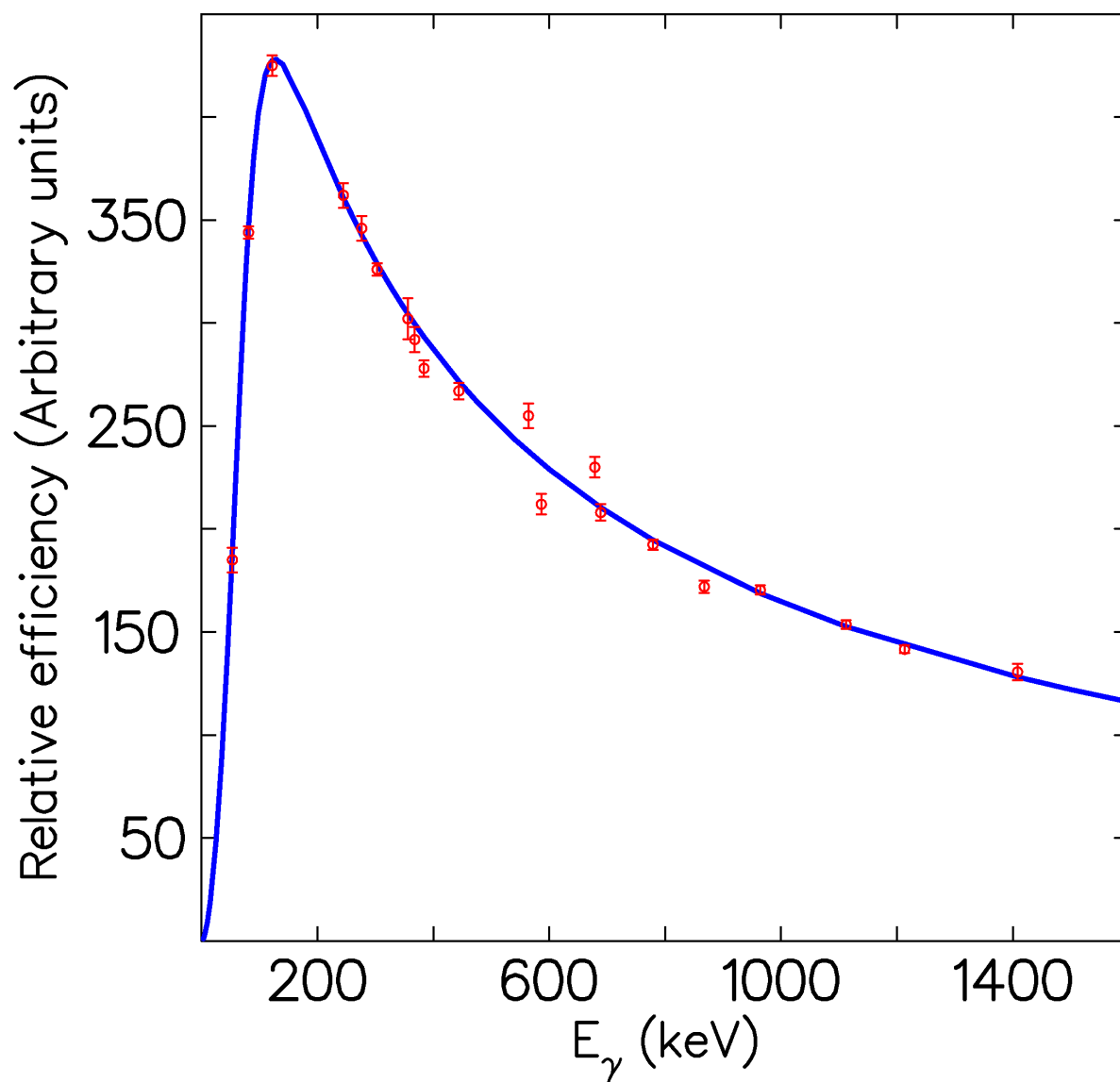


FIG. 3.22. Plot of the detector efficiency of the AFRODITE array as a function of energy obtained with ^{152}Eu and ^{133}Ba sources in our experiment.

This technique to identify isomers is known as the Recoil Shadow Anisotropy Method (RSAM) [124]. It can be applied to experiments performed with thin targets and collimated clover detectors. It does not require any additional device. Isomers in the nanosecond range can be identified with this method.

In heavy-ion fusion-evaporation reaction with a thin target, the prompt γ -rays are emitted at the target position and they are equally seen by the detectors at the same solid angle. However, the delayed γ -rays, following de-excitation of isomeric states, are emitted at a certain distance from the target position. Consequently the measured γ -ray intensity with detectors at lower angles decreases compared to those measured with detectors at higher angles. In order to take into account the relative detection efficiency at each angle, gated spectra from different angles are normalised. In our case a normalizing coefficient of 0.9 was used because one crystal at 95° was left out as it had poor resolution. It can be noted that should the target be shifted slightly from the center, the clover collimator shadowing effect appears also for the prompt transitions. Thus, to compensate for it a normalizing coefficient different from the ratio of working clover elements is needed.

The AFRODITE clover detectors are placed at average angles of 90° and 135° , but the crystals are arranged in separate rings at 85° and 95° , 130° and 140° . γ -rays from recoiling nuclei are shadowed by collimators at 80° and 130° . Thus, the intensity for delayed transitions will be greater at 95° (140°) compared to that at 85° (130°).

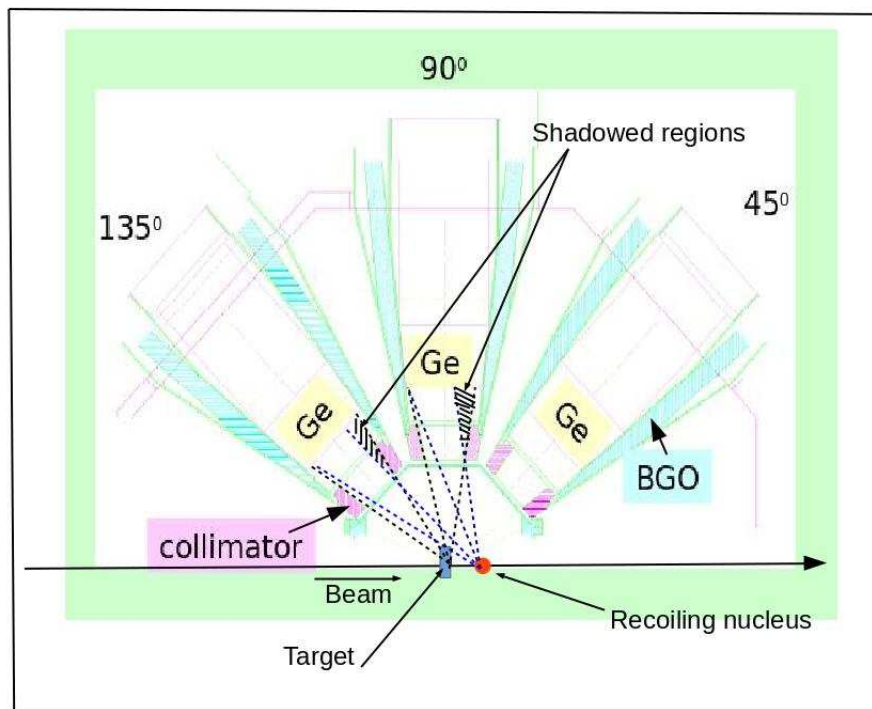


FIG. 3.23. Schematic illustration of geometry of the AFRODITE clover detectors showing collimator shadow effect on the detectors located at 85° and 135° for the delayed transition.

The magnitude of the shadow effect on the delayed transitions can be calculated in terms of a parameter called RSAM anisotropy, defined as:

$$A = \frac{A_\gamma(95^\circ) - A_\gamma(85^\circ)}{A_\gamma(95^\circ) + A_\gamma(85^\circ)}, \quad (3.25)$$

where A_γ is the measured area of the photo-peak of the transition which is proportional to the γ -ray intensity of transition. Furthermore using the calibration for AFRODITE (see Ref. [125]), which is shown in Fig. 3.24, one can evaluate the lifetime of the isomer.

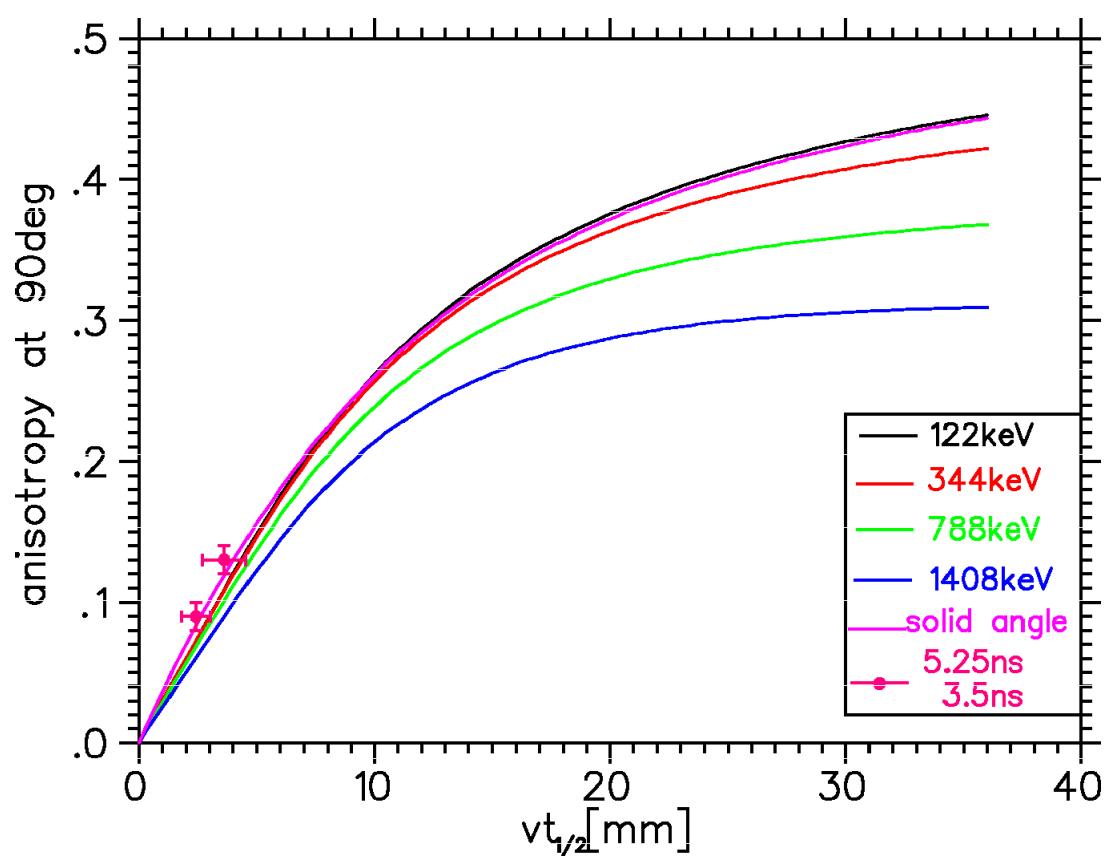


FIG. 3.24. Calibration anisotropy curve and the experimental data for the 12^+ (3.5 ns) and 7^- (5.25 ns) isomers in ^{196}Hg from Ref. [125].

Chapter 4

Experimental details, results and discussion

4.1 Introduction

In order to extend investigations of chiral symmetry in the $A \sim 190$ mass region, two experiments were performed to study $^{192,193}\text{Tl}$. This chapter describes the experiments, the experimental results and the corresponding theoretical interpretation. Experimental details on the construction of the level schemes, the spin and parity assignments of the levels, and the intensity measurements are given. The interpretation is based on the analysis of the measured alignments and on the calculations performed with the multiparticle rotor (MPR) model, the two-quasiparticle-plus-triaxial rotor model (TQPRM) and the Cranked Nilsson-Strutinsky (CNS) model.

4.2 Experimental details

γ -spectroscopy studies were performed using a heavy-ion reaction of $^{160}\text{Gd}(^{37}\text{Cl}, 4n)$ at $E_{lab} = 167$ MeV, with a thin target of 1.0 mg/cm^2 and the 9 clovers of the AFRODITE array placed at $\theta_{lab} = 90^\circ$ and $\theta_{lab} = 135^\circ$ with respect to the beam direction. Two weekends of beam time were allocated for the thin target experiment. In addition, lifetime measurements using the Doppler Shift Attenuation Method (DSAM) were attempted, using

a thick target of 10.0 mg/cm^2 and a beam energy of $E_{lab} = 162 \text{ MeV}$. The clover detectors were placed at $\theta_{lab} = 45^\circ$ and $\theta_{lab} = 135^\circ$ with respect to the beam direction. The trigger condition required at least two clovers firing in coincidence. The beam and the target were chosen to ensure a large initial recoil velocity of the ^{193}Tl nuclei, $v/c = 1.8\%$. Unfortunately no distinct Doppler broadening was observed in the peaks from the second experiment indicating that all nuclei were stopped by the time they emitted the γ -rays. Thus, the data sets from both thin and thick target experiments were used to build the level schemes, while the data from the thin target experiment were used to measure the angular distribution coefficients and the polarization anisotropies. The second weekend data from this experiment showed a contribution from contaminants produced in the $^{37}\text{Cl} + ^{16}\text{O}$ reaction. This indicated that the target had partially oxidized. The obtained data was not sufficient to solve all open questions in the level scheme of ^{193}Tl , including finding linking transitions for the weaker bands and establishing their spin and parity. For the thin and thick target experiments only one Ge crystal was left out due to poor resolution, all other clovers crystals were in good working conditions with resolution of less than 3 keV.

To solve the open questions about possible chirality in ^{193}Tl , another experiment was performed using a different reaction of $^{181}\text{Ta}(^{18}\text{O}, 6n)$ at $E_{lab} = 105 \text{ MeV}$ which has much larger cross-section for the production of ^{193}Tl than the previous reaction. A thin target of 1.0 mg/cm^2 was used and the AFRODITE clovers were placed at $\theta_{lab} = 90^\circ$ and $\theta_{lab} = 135^\circ$ with respect to the beam direction. Moreover, the data set was considerably larger due to the use of the digital acquisition system which has little dead time in comparison with the previously used analog electronics. Two weekends of beam time were allocated for this experiment. Generally the nine clover detectors of AFRODITE had a resolution of less than 3 keV during this experiment. All of them were working, except two crystals that were left out as they had poor resolution.

4.3 Experimental results

4.3.1 Level scheme of ^{193}Tl

The first level scheme of ^{193}Tl was constructed by Newton *et al.* [126] through a variety of reactions: $^{181}\text{Ta}(^{16}\text{O}, 4\text{n})$ at bombarding energies of $E_{lab} = 79, 84, 89$ and 98 MeV; $^{184}\text{W}(^{14}\text{N}, 5\text{n})$ at $E_{lab} = 82, 86$ and 89 MeV; $^{197}\text{Au}(^4\text{He}, 8\text{n})$ at $E_{lab} = 93, 104$ and 116 MeV. States with spin up to $15/2\hbar$ were established and the level scheme started from the $9/2^-$ isomeric state ($t_{1/2} = 2.1$ min) which is fed by all γ -rays that were observed in their data.

Later, the level scheme of ^{193}Tl was extended by W. Reviol *et al.* [70] using the $^{160}\text{Gd}(^{37}\text{Cl}, 4\text{n})$ reaction at a bombarding energy of $E_{lab} = 167$ MeV with 12 Compton-suppressed Ge detectors surrounded by 50 BGO elements. Two main sequences of levels of different parity all feeding the $9/2^-$ isomeric state were identified. The level scheme was constructed up to the $I = 41/2$ level at an excitation energy of $E_x = 6.089$ MeV.

In the present work, further investigations were performed on the states of ^{193}Tl . Most of the transitions in the previous level scheme were observed, but the level scheme needed a considerable revision including a modification in the placement of one band and several other transitions. It was also extended with additional 29 transitions.

The experimental results for the ^{193}Tl level scheme are summarized in TABLE. 4.1. showing the energies, total intensities, R_{AD} ratios, linear polarization anisotropies, γ -ray intensities, excitation energy of the initial levels and spin assignments of the γ -transitions in ^{193}Tl . The constructed ^{193}Tl level scheme is shown in Fig. 4.1.

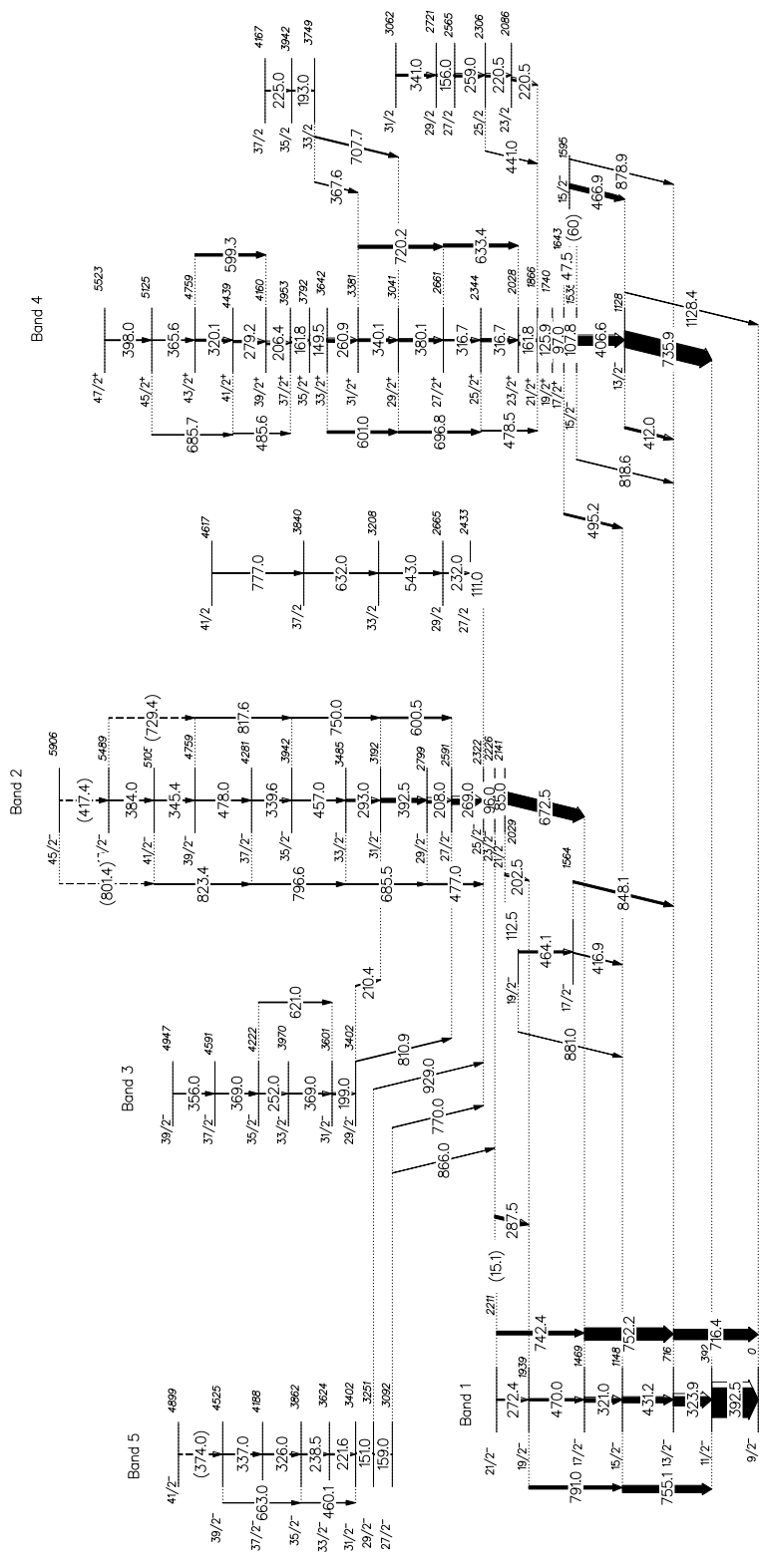


FIG. 4.1. Total level scheme of ^{193}Tl as constructed in this work.

TABLE. 4.1: List of the energies, total γ -ray intensities, angular distribution ratios, linear polarization anisotropy, γ -ray intensities, energy of the initial levels and corresponding spin assignments for the γ -transitions in ^{193}Tl . The low energy transition marked with # could not be observed, but was tentatively placed in the level scheme on the basis of the coincidence relationships of the observed transitions. The star (*) labels an unobserved transition that lies at the shoulder of the X-ray peak tentatively placed in the level scheme based on observed coincidence relationships. Values marked with @ correspond to unseparated doublet transitions, the measured value is for the total peak.

E_γ [keV]	I_t	R_{AD} ratio	A_{pol}	I_γ	E_{in} [keV]	$I_i^\pi \rightarrow I_f^\pi$
15.1#					2226	$23/2^- \rightarrow 21/2^-$
47.5	2993(419)	0.86(20)		1829(419)	1643	$17/2^+ \rightarrow 15/2^-$
60.3*					2226	$15/2^- \rightarrow 15/2^-$
85.0					1643	$23/2^- \rightarrow 21/2^-$
96.0	5275(765)	0.87(17)		475(69)	2322	$25/2^- \rightarrow 23/2^-$
97.0	5132(395)	0.75(27)		475(37)	1740	$19/2^+ \rightarrow 17/2^+$
107.8	811(65)	0.87(19)		596(48)	1643	$17/2^+ \rightarrow 15/2^-$
111.0	648(146)	0.78(12)		85(19)	2433	$27/2 \rightarrow 25/2$
112.5	687(130)	0.85(25)		87(17)	2141	$21/2^- \rightarrow 19/2^-$
125.9	4816(384)	0.81(21)		854(68)	1866	$21/2^+ \rightarrow 19/2^+$
149.5	1660(143)	0.74(13)		832(37)	3792	$35/2^+ \rightarrow 33/2^+$
151.0	384(73)	0.76(19)		102(19)	3402	$31/2^- \rightarrow 29/2^-$
156.0	697(97)	0.81(30)		198(28)	2721	$29/2 \rightarrow 27/2$
159.0	231(47)	0.74(21)		68(14)	3251	$31/2^- \rightarrow 29/2^-$
161.8	3106(418)			947(127)	2028	$23/2^+ \rightarrow 21/2^+$
161.8	1747(151)	0.87(21)		533(46)	3953	$37/2^+ \rightarrow 35/2^+$
193.0	231(33)	0.73(18)		126(18)	3942	$35/2 \rightarrow 33/2$
199.0	651(65)	0.79(11)		287(28)	3601	$31/2^- \rightarrow 29/2^-$
202.5	828(149)	0.90(14)		375(67)	2141	$21/2^- \rightarrow 19/2^-$
206.4	1163(124)	0.85(14)		541(58)	4160	$39/2^+ \rightarrow 37/2^+$
208.0	1766(351)	0.82(12)		833(166)	2799	$29/2^- \rightarrow 27/2^-$
210.4	288(48)	0.73(28)		138(23)	3402	$29/2^- \rightarrow 31/2^-$
220.5	706(152) [@]	0.75(27) [@]		360(79) [@]	2086	$23/2 \rightarrow 21/2$

TABLE. 4.1 – continued from previous page

E_γ [keV]	I_t	R_{AD} ratio	A_{pol}	I_γ	E_{in} [keV]	$I_i^\pi \rightarrow I_f^\pi$
220.5	706(152) [ⓐ]	0.75(27) [ⓐ]		360(79) [ⓐ]	2306	25/2 \rightarrow 23/2
221.6	449(93)	0.83(8)	-0.172(43)	232(48)	3624	33/2 ⁻ \rightarrow 31/2 ⁻
225.0	231(27)	0.87(8)		122(14)	4167	37/2 \rightarrow 35/2
232.0	233(59)	0.86(26)		128(32)	2665	29/2 \rightarrow 27/2
238.5	409(51)	0.77(12)	-0.063(43)	232(29)	3862	35/2 ⁻ \rightarrow 33/2 ⁻
252.0	135(43)	0.85(24)		82(26)	4222	35/2 ⁻ \rightarrow 33/2 ⁻
259.0	1427(113)	0.70(16)		875(69)	2565	27/2 \rightarrow 25/2
260.9	1342(179)	0.72(20)	-0.096(37)	840(112)	3642	33/2 ⁺ \rightarrow 31/2 ⁺
269.0	2556(169)	0.78(9)	-0.038(34)	1649(109)	2591	27/2 ⁻ \rightarrow 25/2 ⁻
272.4	445(67)	0.81(21)		291(44)	2211	21/2 ⁻ \rightarrow 19/2 ⁻
279.2	716(107)	0.77(7)	-0.059(31)	479(72)	4439	41/2 ⁺ \rightarrow 39/2 ⁺
287.5	918(159)	1.12(8)		814(141)	2226	23/2 ⁻ \rightarrow 19/2 ⁻
293.0	727(90)	0.81(10)		507(62)	3485	33/2 ⁻ \rightarrow 31/2 ⁻
316.7	1028(81)	0.73(8)		760(60)	2344	25/2 ⁺ \rightarrow 23/2 ⁺
316.7	459(48)	0.66(37)		339(35)	2661	27/2 ⁺ \rightarrow 25/2 ⁺
320.1	639(87)	0.76(9)		476(65)	2661	43/2 ⁺ \rightarrow 41/2 ⁺
321.0	1611(225)	0.85(12)		1203(68)	1469	17/2 ⁻ \rightarrow 15/2 ⁻
323.9	3841(686)	0.86(9)		2886(515)	716	13/2 ⁻ \rightarrow 11/2 ⁻
326.0	401(74)	0.74(9)		303(56)	4188	37/2 ⁻ \rightarrow 35/2 ⁻
337.0	173(35)	0.68(19)		133(27)	4759	39/2 ⁻ \rightarrow 37/2 ⁻
339.6	270(65)	0.74(10)	-0.061(37)	209(50)	4182	37/2 ⁻ \rightarrow 35/2 ⁻
340.1	880(74)	0.72(13)	-0.051(33)	683(57)	3381	31/2 ⁺ \rightarrow 29/2 ⁺
341.0	679(54)	0.75(21)		527(42)	3062	31/2 \rightarrow 29/2
345.4	153(26)	0.76(25)	-0.098(36)	120(20)	5105	41/2 ⁻ \rightarrow 39/2 ⁻
356.0	129(15)	0.77(23)		103(12)	4947	39/2 ⁻ \rightarrow 37/2 ⁻
365.6	217(49)	0.74(24)		175(40)	5125	45/2 ⁻ \rightarrow 43/2 ⁻
367.5	210(43)	0.77(21)		170(35)	3749	33/2 \rightarrow 31/2
369.0	314(35) [ⓐ]	0.70(12) [ⓐ]		219(41)	3970	33/2 ⁻ \rightarrow 31/2 ⁻
369.0	314(35) [ⓐ]	0.70(12) [ⓐ]		188(19)	4591	37/2 ⁻ \rightarrow 35/2 ⁻
374.0	29(6)	0.75(23)		24(5)	4899	41/2 ⁻ \rightarrow 39/2 ⁻
380.1	974(110)	0.69(12)	-0.053(33)	802(91)	3041	29/2 ⁺ \rightarrow 27/2 ⁺

TABLE. 4.1 – continued from previous page

E_γ [keV]	I_t	R_{AD} ratio	A_{pol}	I_γ	E_{in} [keV]	$I_i^\pi \rightarrow I_f^\pi$
384.0	159(44)	0.85(29)		132(36)	5489	$43/2^- \rightarrow 41/2^-$
392.5	11045(1142)	0.91(8)	-0.019(29)	9227(954)	392	$11/2^- \rightarrow 9/2^-$
392.5	1530(189)	0.78(12)	-0.078(37)	1275(157)	3192	$31/2^- \rightarrow 29/2^-$
398.0	278(49)	0.64(11)		234(41)	5522.6	$47/2^+ \rightarrow 45/2^+$
406.6	3231(162)	0.83(14)	-0.069(29)	2740(137)	1535	$15/2^- \rightarrow 13/2^-$
412.0	593(59)	1.12(8)		567(56)	1128	$13/2^- \rightarrow 13/2^-$
416.9	267(85) [Ⓐ]			229(73) [Ⓐ]	1564	$17/2^- \rightarrow 15/2^-$
417.4	267(85) [Ⓐ]			229(73) [Ⓐ]	5906	$45/2^- \rightarrow 43/2^-$
431.2	1908(137)	0.79(8)	-0.037(27)	1653(119)	1148	$15/2^- \rightarrow 13/2^-$
441.0	126(15)	1.16(20)		121(14)	1148	$25/2 \rightarrow 21/2$
457.0	311(70)	0.65(28)	-0.028(13)	275(62)	3942	$35/2^- \rightarrow 33/2^-$
460.1	171(44)	1.25(35)		165(43)	3862	$35/2^- \rightarrow 31/2^-$
464.1	634(121)	0.73(17)		563(107)	2029	$19/2^- \rightarrow 17/2^-$
466.9	1495(120)	0.73(16)	-0.053(33)	1330(106)	1595	$15/2^- \rightarrow 13/2^-$
470.0	691(69)	0.82(17)		615(61)	1939	$19/2^- \rightarrow 17/2^-$
477.0	423(59)	1.28(28)		411(57)	2799	$29/2^- \rightarrow 25/2^-$
478.0	229(46)	0.83(8)		205(41)	4759	$39/2^- \rightarrow 37/2^-$
478.5	253(62)	1.23(29)		246(60)	2344	$25/2^+ \rightarrow 21/2^+$
485.6	67(18)	1.25(13)		65(17)	4439	$41/2^+ \rightarrow 37/2^+$
495.2	560(90)	0.78(17)	0.034(31)	555(89)	1643	$17/2^+ \rightarrow 15/2^-$
543.0	169(46)	1.17(6)		165(45)	3208	$33/2 \rightarrow 29/2$
599.3	571(131) [Ⓐ]			561(129) [Ⓐ]	4759	$43/2^+ \rightarrow 39/2^+$
600.5	279(104)			275(102)	3191	$31/2^- \rightarrow 27/2^-$
601.0	571(131) [Ⓐ]			561(129) [Ⓐ]	3642	$33/2^+ \rightarrow 29/2^+$
621.0	85(22)	1.41(11)		84(22)	4222	$35/2^- \rightarrow 31/2^-$
632.0	200(27)	1.21(31)		162(27)	3840	$37/2 \rightarrow 33/2$
633.4	979(103)	1.33(11)	0.041(39)	965(101)	2661	$27/2^+ \rightarrow 23/2^+$
663.0	68(18)	1.31(20)		67(18)	4525	$39/2^- \rightarrow 35/2^-$
672.5	3665(257)	1.21(15)	0.038(32)	3616(354)	2141	$21/2^- \rightarrow 17/2^-$
685.5	436(91)	1.25(11)	0.073(36)	431(90)	3485	$33/2^- \rightarrow 29/2^-$
685.7	46(7)	1.25(21)		45(7)	5125	$45/2^+ \rightarrow 41/2^+$

TABLE. 4.1 – continued from previous page

E_γ [keV]	I_t	R_{AD} ratio	A_{pol}	I_γ	E_{in} [keV]	$I_i^\pi \rightarrow I_f^\pi$
696.8	718(50)	1.15(8)	0.039(25)	709(49)	3041	$29/2^+ \rightarrow 25/2^+$
707.7	388(84)	1.33(18)		383(83)	3749	$33/2 \rightarrow 29/2$
716.4	3257(588)	1.29(23)	0.057(28)	3218(589)	716	$13/2^- \rightarrow 9/2^-$
720.2	987(71)	1.33(5)	0.059(42)	975(70)	3381	$31/2^+ \rightarrow 27/2^+$
729.4	29(10)			29(10)	5489	$43/2^- \rightarrow 39/2^-$
735.9	5003(550)	0.72(13)	0.001(34)	4829(531)	1129	$13/2^- \rightarrow 11/2^-$
742.4	1205(120)	1.29(25)		1192(119)	2211	$21/2^- \rightarrow 17/2^-$
750.0	164(52)	1.21(14)		163(51)	3942	$35/2^- \rightarrow 31/2^-$
752.2	3885(622)	1.20(34)		3843(615)	1469	$17/2^- \rightarrow 13/2^-$
755.1	2274(477)	1.25(12)		2249(472)	1148	$15/2^- \rightarrow 11/2^-$
770.0	139(29)	0.76(37)	-0.051(43)	135(28)	3092	$27/2^- \rightarrow 25/2^-$
777.0	182(29)	1.28(28)		180(29)	4617	$41/2 \rightarrow 37/2$
791.0	1001(70)	1.13(11)	0.038(25)	992(69)	1939	$19/2^- \rightarrow 15/2^-$
796.6	310(59)	1.15(8)	0.131(47)	307(58)	4281	$37/2^- \rightarrow 33/2^-$
801.4	67(16)			66(16)	5906	$45/2^- \rightarrow 41/2^-$
810.9	216(49)	0.53(13)	-0.143(44)	210(48)	3402	$29/2^- \rightarrow 27/2^-$
817.6	113(17)	1.30(11)		112(17)	4759	$39/2^- \rightarrow 35/2^-$
818.6	172(39)	0.78(8)		167(38)	1535	$15/2^- \rightarrow 13/2^-$
823.4	93(28)	1.32(20)		92(28)	5105	$41/2^- \rightarrow 37/2^-$
848.1	667(133)	1.131(21)		662(132)	1564	$17/2^- \rightarrow 13/2^-$
866.0	85(21)	1.16(25)	0.093(54)	84(21)	3092	$27/2^- \rightarrow 21/2^-$
878.9	135(23)	0.86(15)		132(22)	1595	$15/2^- \rightarrow 13/2^-$
881.0	82(11)	1.23(22)		81(11)	2029	$19/2^- \rightarrow 15/2^-$
929.0	97(22)	1.17(31)		96(22)	3251	$29/2^- \rightarrow 25/2^-$
1128.4	149(19)	1.34(8)		148(19)	1128	$13/2^- \rightarrow 9/2^-$

4.4 Rotational bands and other structures of ^{193}Tl

4.4.1 Band 1

This is a negative parity band. It consists of 7 states and 11 transitions all feeding the $9/2^-$ isomeric state through the 392.5 keV ($11/2^- \rightarrow 9/2^-$) and the 716.4 keV ($13/2^- \rightarrow 9/2^-$) transitions. The intensities of all other bands flow into this yrast band through several linking transitions. Seven new linking transitions to Band 2 and Band 4 have been added, among them the 1128.4 keV ($13/2^- \rightarrow 9/2^-$) transition feeding directly the $9/2^-$ isomeric state. This transition is important because its presence suggests that the previously assigned positive parity to the $I = 13/2$ state at excitation energy of $E_x = 1128$ keV is questionable. More details are given in section 4.4.4.

The data analysis confirmed that Band 1 consists of successive transitions of M1 character and their corresponding E2 cross-overs. Two transitions with close energies of 752.2 keV ($17/2^- \rightarrow 13/2^-$) and 755.1 keV ($15/2^- \rightarrow 11/2^-$) are observed and placed in Band 1. The placement of these two transitions is illustrated in Fig. 4.2 with gates on 791.0 keV and 716.4 keV transitions. The 752.2 keV peak that is observed in the 716.4 keV gate is not found in the 791.0 keV gate, thus the 752.2 keV γ -ray must be in anti-coincidence with the 791.0 keV transition, but in coincidence with the 716.4 keV γ -ray. Similarly a 755.1 keV peak is observed in the 791.0 keV gated spectrum but not in the spectrum gated on 716.4 keV. So 755.1 keV γ -ray is in coincidence with the 791.0 keV transition and in anti-coincidence with the 716.4 keV transition. A third transition with close energy of 750 keV was identified and placed in Band 2. Similarly the energy doublet of 321.0 keV ($17/2^- \rightarrow 15/2^-$) and 323.9 keV ($13/2^- \rightarrow 11/2^-$) transitions was identified in Band 1. The 321.0 keV γ -ray is observed in the 716.4 keV gate, while the 323.9 keV peak appears strongly in the 791.0 keV gate (see Fig. 4.2). Thus the 321.0 keV transition is in coincidence with the 716.4 keV transition, while the 323.9 keV γ -ray is in coincidence with the 791.0 keV transition. A 392.5 keV doublet was also observed and is illustrated by a clear enhancement of the 392.5 keV peak intensity that is seen in the 791.0 keV gate compared to its intensity in the 716.4 keV gate. The spectra in Fig. 4.2. show also the other transitions placed in Band 1 and the new transitions decaying from Band 2 and Band 4, in particular the new 818.8 keV ($15/2^- \rightarrow 13/2^-$) transition and the new linking transitions to Band 2,

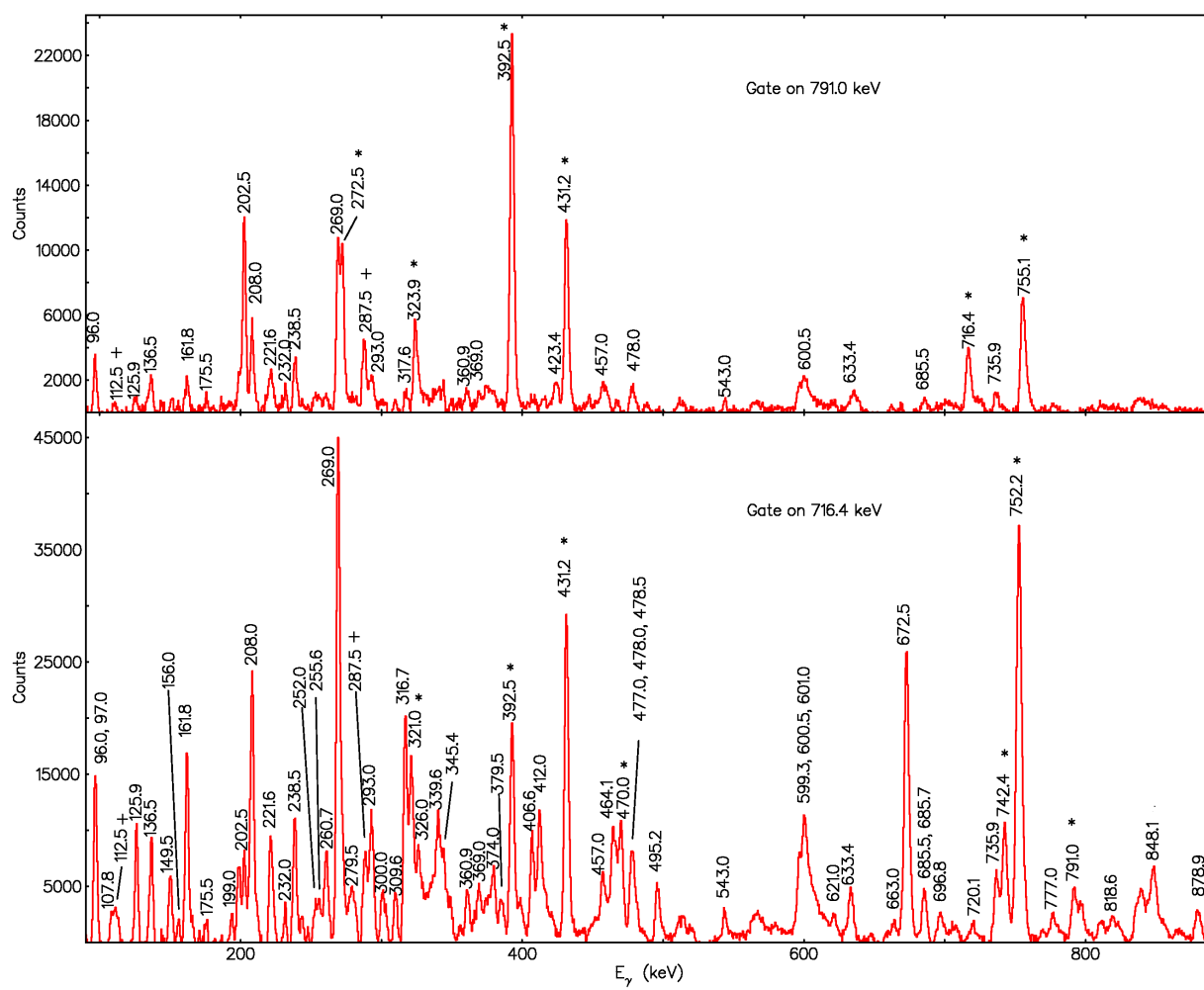


FIG. 4.2. Spectra gated on 716.4 and 791.0 keV transitions. The star signs (*) show the transitions placed in Band 1. The new linking transitions to Band 2 are labeled with +.

287.5 keV ($23/2^- \rightarrow 19/2^-$) and 112.5 keV ($21/2^- \rightarrow 19/2^-$).

4.4.2 Band 2

Band 2 is a negative parity band feeding Band 1 through several transitions. Two new transitions with low energies of 96.0 keV ($25/2^- \rightarrow 23/2^-$) and 85.0 keV ($23/2^- \rightarrow 21/2^-$) were added in the band crossing region, thus increasing the excitation energy and the previously assigned spin of this band. The remaining transitions of Band 2 were observed previously and their placement was confirmed in the present work.

One doublet (477.0 keV and 478.0 keV) was identified in Band 2. The gate on 672.5 keV shows an asymmetric wide peak around 477.0 keV while the spectrum gated on 477.0 keV clearly shows the 478.0 keV transition (see Fig. 4.3 and Fig. 4.4).

Band 2 is linked to the yrast band mainly through the 672.5 keV transition. The spectrum gated on 672.5 keV shows most of the transitions placed in Band 2. In particular, a clear enhancement of the 85.0 keV X-ray peak is seen in the 672.5 keV gate in comparison to the 735.9 keV gate (see Fig. 4.4) which indicates the presence of a 85 keV γ -ray. The new low-energy transition of 96.0 keV is visible in the 672.5 keV gate, while a 97.0 keV transition is placed in the positive parity Band 4, see the 735.9 keV gate in Fig. 4.4.

In general, measurements on the 85.0 keV peak are difficult as it is overlapping with the X-rays region. However, the measured angular distribution ratio of the other transitions, such as the 287.5 keV, 112.5 keV, 202.5 keV, and 672.5 keV transitions suggest that the 85.0 keV γ -ray is a stretched magnetic dipole. Analysis of the angular distribution ratio shows that the 96.0 keV transition should be a stretched dipole. It is not possible for this transition to be an electric dipole since its intensity will be too low in comparison to the intensities of the transitions depopulating the $23/2^-$ state which it feeds. The measured intensity of the 287.5 keV transition (which is just one of the transitions depopulating the $23/2^-$ state) from a gate above it will be greater than the intensity of the 96.0 keV transition itself, see TABLE. 4.2. However, sufficient intensity of the 96.0 keV transition can be obtained if this transition is a magnetic dipole. Thus, Band 2 is assigned negative parity.

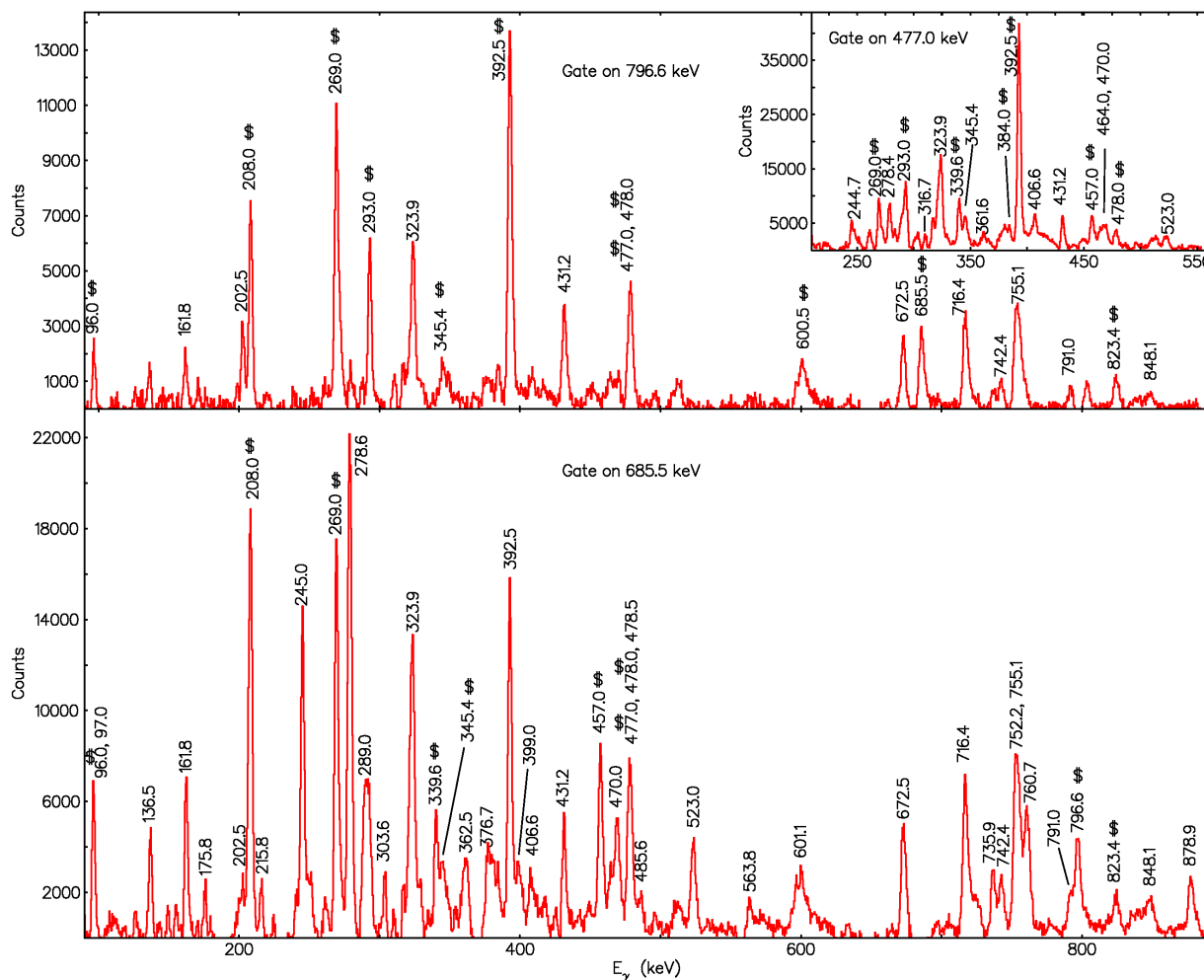


FIG. 4.3. Spectra illustrating the coincidence relationships of the transitions in Band 2. Peaks that belong to Band 2 are marked with \$. The spectrum in the insert is gated on 477.0 keV and shows that the 477.0 keV transition is in coincidence with the 478.0 keV γ -ray.

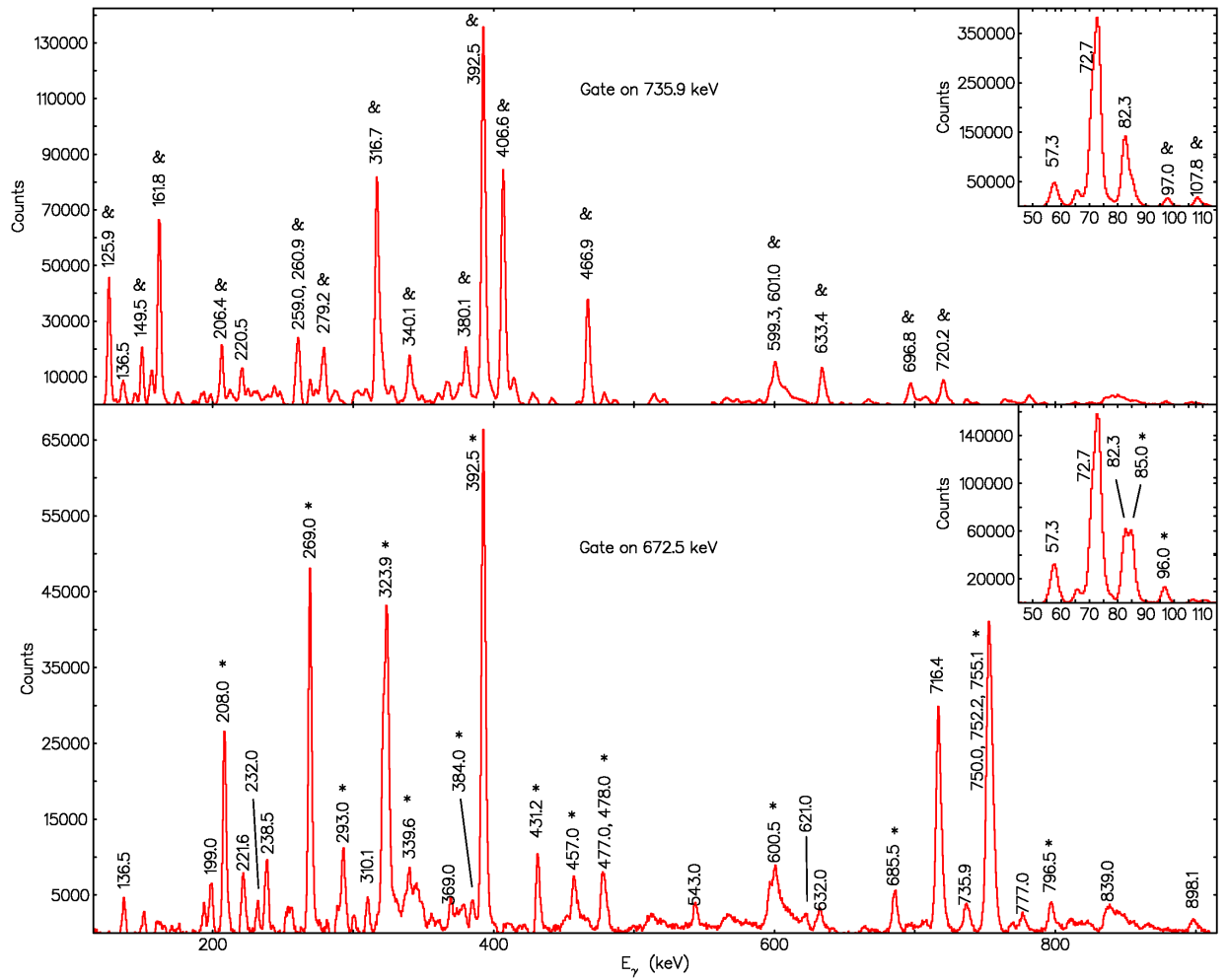


FIG. 4.4. Illustration of the coincidence data for Band 2. Gate on 672.5 keV shows the transitions marked with * that belong to Band 2, including the new low-energy transitions 85.0 and 96.0 keV. The transitions labeled with & in the 735.9 keV gate were placed in Band 4.

TABLE. 4.2. Measured total intensities for the transitions below the $25/2^-$ state measured in a spectrum gated on the 269.0 keV transition. The star sign (*) labels the multipolarity of the 96.0 keV γ -ray that was deduced.

Total intensities measured in the spectrum gated on 269.0 keV			
E_γ [keV]	ML	Intensity	$I_i^\pi \rightarrow I_f^\pi$
96.0	M1*	4068(159)	$25/2^- \rightarrow 23/2^-$
96.0	E1	543(21)	$25/2^- \rightarrow 23/2^-$
112.5	M1	652(114)	$21/2^- \rightarrow 19/2^-$
202.5	M1	670(98)	$21/2^- \rightarrow 19/2^-$
287.5	E2	691(111)	$21/2^- \rightarrow 19/2^-$
672.5	E2	1851(83)	$21/2^- \rightarrow 17/2^-$

Based on the intensity measurements, Band 2 has largest intensity at low spins, near the strong 269.0 keV transition and the intensity decreases upwards. At the top of the band the statistics is not enough for a conclusive placement of the 801.4 keV, 729.4 keV and 417.4 keV transitions.

4.4.3 Band 3

This is a weak band that was previously observed [70] but did not have parity assignment and only tentative spins. Furthermore, none of the linking transitions that were suggested in the previous work [70] could be identified in the present work. No evidence for a 383.3 keV transition in addition to the 384.0 keV transition placed at the top in Band 2 ($43/2^- \rightarrow 41/2^-$) was found. Similarly, no 568.0 keV transition in parallel to the 199.0 keV and 369.0 keV transitions was observed. Six transitions (199.0, 369.0, 252.0, 621.0, 369.0, 356.0 keV) were identified to belong to this band. Based on angular distribution ratio measurements five of them, 199.0, 369.0, 252.0, 369.0, 356.0 keV transitions, are stretched dipoles, while the 621.0 keV transition is a stretched quadrupole. The 621.0 keV transition is placed as a cross-over of the 369.0 keV and 252.0 keV transitions. Intensity measurements were also used to order the transitions in this band. Based on the data available and the systematics it was assumed that these transitions form a rotational band built of stretched M1 transitions with E2 cross overs.

Search for possible linking transitions was undertaken based on the coincidence data. Two

new linking transitions of 810.9 keV and 210.4 keV were identified. The negative parity assignment for this band was determined using the angular distribution ratio and the linear polarization anisotropy for the 810.9 keV transition showing it is a stretched magnetic dipole.

To test the consistency of the assumed magnetic nature of the stretched dipole 199.0 keV transition and its placement at the bottom of the band, the intensity balance near the $29/2^-$ level was measured. It was found that this stretched dipole should be of magnetic nature in order to have sufficient intensity. Because if the 199.0 keV γ -ray is a stretched electric dipole, its total intensity measured from the 369.0 keV gated spectrum would be 171(22) while the total intensities of the 810.9 keV and 210.4 keV transitions respectively would be 126(18) and 177(34). Therefore the total intensity of the 199.0 keV transition (if an electric dipole), would be too small in comparison with the sum of the intensities of the 810.9 and 210.4 keV transitions. However, the total intensity of the 199.0 keV transition, if it is a stretched magnetic dipole, would be 361(47), which is in good agreement with the sum of the intensities of the 810.9 keV and 210.4 keV transitions. Thus, the test is positive, i.e. the suggested magnetic character of the 199.0 keV γ -ray is consistent with its placement.

Fig. 4.5 shows two gated spectra illustrating the transitions in this band. The two linking transitions are visible in the spectrum gated on the 369.0 keV γ -ray. The 810.9 keV gate shows all the transitions placed in Band 3.

4.4.4 Band 4 and its decay paths

Band 4 is a positive parity band characterised by irregular spacings of the energy levels and a larger number of dipole transitions with their E2 cross-over transitions. A number of new transitions have been added to this band and the placement of a few old transitions was revised.

The analysis of the total intensity, the measurements of the angular distribution ratio, and the linear polarization anisotropy show a positive parity structure starting from the $17/2^+$ state at $E_x = 1643$ keV. This is different from what was suggested in the previous

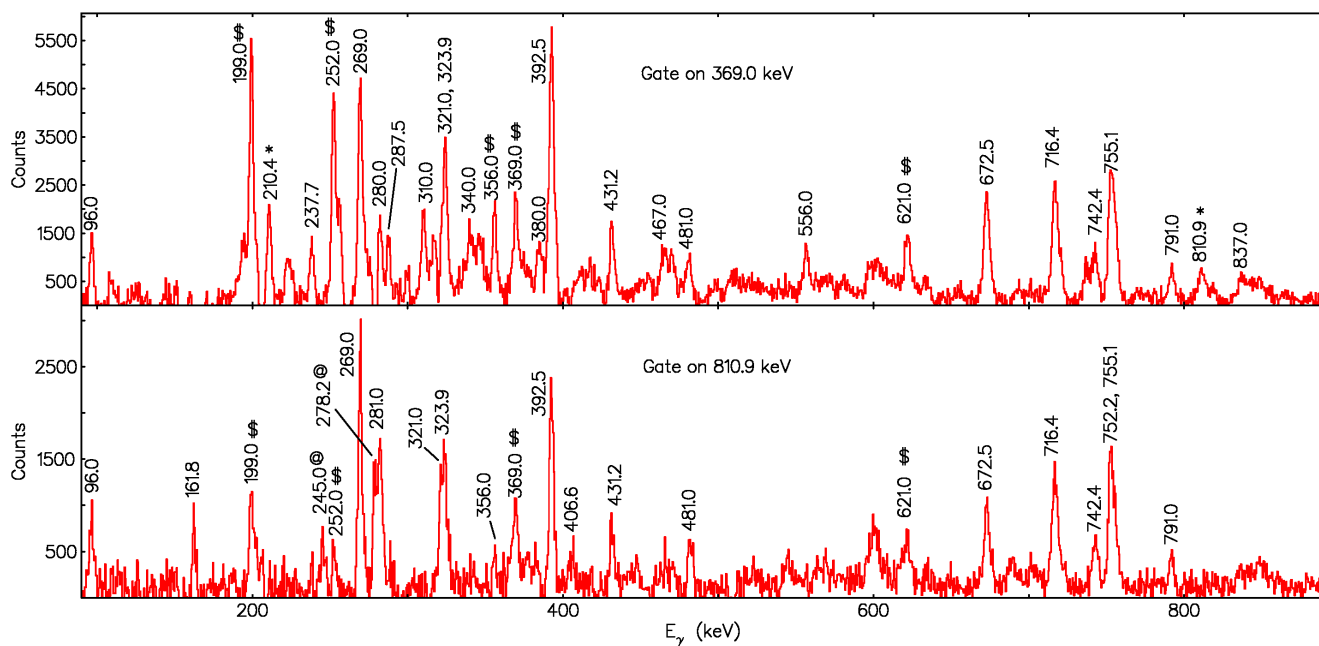


FIG. 4.5. Gates on 810.9 and 369.0 keV illustrating the coincidence data for Band 3. The two linking transitions are visible in the 369.0 keV gated spectrum and are marked with *. The same gate shows that 369.0 keV is a doublet and the two members are in coincidence. The dollar sign (\$) labels the transitions that were placed in Band 3. Transitions marked with @ belong to ^{194}Tl .

work [70] where the positive parity structure starts from the $I = 13/2$ level at excitation energy of $E_x = 1128$ keV, i.e. this $I = 13/2$ level and the $I = 15/2$ level at $E_x = 1535$ keV were previously assigned positive parity, while in this work they were found to have negative parity. The present measurements show that the 735.9, 406.6 and 466.9 keV transitions are stretched magnetic dipoles, while the 495.2 keV γ -ray is a stretched electric dipole transition. The negative parity assignment of the 13/2 level is also consistent with the observation of the 1128.0 keV transition which would have to be M2 if this level had positive parity. M2 multipolarity corresponds to strong hindrance of such a transition, inconsistent with our observation. Considering the intensities of the 406.6, 818.6, 466.9 and 878.9 keV transitions, it follows that the 107.8 and 47.5 keV transitions must be stretched electric dipole transitions. It is unlikely for the 107.8 and the 47.5 keV transitions to be magnetic since their intensities will be considerably larger than the intensities of the 406.6, 818.6, 466.9 and 878.9 keV transitions depopulating the two $15/2^-$ states. That will demand other large-intensity paths depopulating these $15/2^-$ states. Such transitions were not found in our coincidence data. It was also observed that the 406.6 keV transition is in coincidence with the 47.5 keV γ -ray (see Fig. 4.6), suggesting a presence of a linking transition connecting the two $15/2^-$ states. The energy of such a transition would be 60.3 keV, but it could not be seen because it has high internal conversion coefficient and it lies too close to the strong 57.4 keV X-ray (see Fig. 4.6.). The gate on 47.5 keV (see the insert in Fig. 4.6) shows that it is in coincidence with the 406.6 keV transition. The enhancement of the 466.9 keV peak in the 47.5 keV gate compared to the 406.6 keV peak (see the spectra gated on 696.8 keV and 125.9 keV in Fig. 4.6) also agrees with the placement of the 47.5 keV transition on top of the 466.9 keV γ -ray, but in coincidence with the 406.6 keV transition.

The $17/2^+$ state was found to be an isomer. Some drop in the intensity of the transitions below this state was observed. Analysis using the Recoil Shadow Anisotropy Method (RSAM) [124] shows that the transitions below the $17/2^+$ state are delayed. The intensity measurements were performed in several gated spectra at 85° (shadowed by detector collimators) and 95° (not shadowed). The RSAM anisotropy parameter A_{RSAM} that can inform about the presence of an isomeric state was calculated.

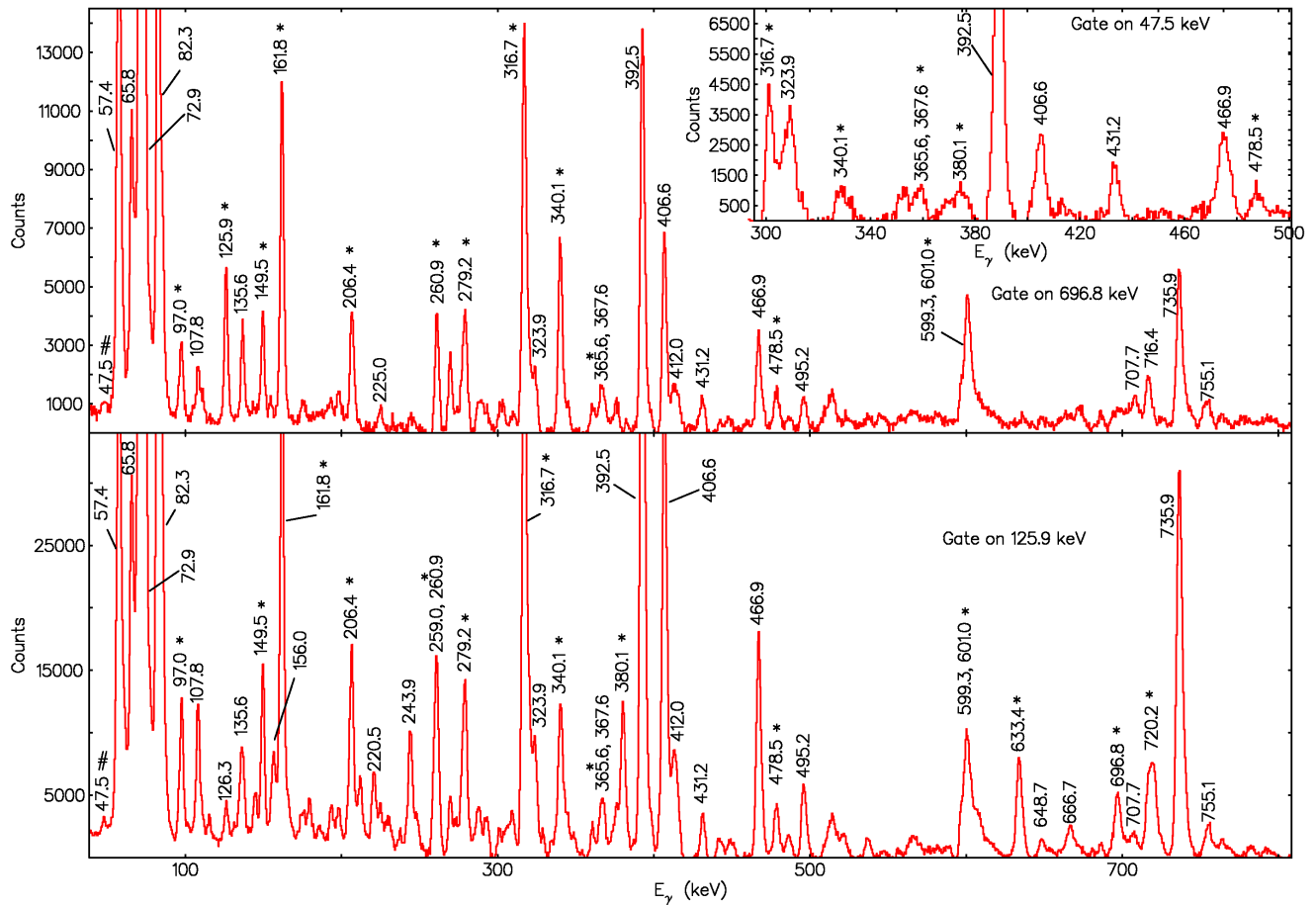


FIG. 4.6. Spectra gated on the 125.9, 696.8 and 47.5 keV transitions respectively. The transitions placed in Band 4 are marked with *. The low energy transition (47.5 [keV]) is marked with #.

TABLE. 4.3. Illustration of the analysis of the total intensities showing that the 107.8 keV and the 47.5 keV transitions are stretched electric dipoles. The star signs (*) labels the multiplicities that were deduced.

Total intensities measured in the spectrum gated on 696.8 keV			
E_γ [keV]	ML	Intensity	$I_i^\pi \rightarrow I_f^\pi$
47.5	E1*	367(72)	$17/2^+ \rightarrow 15/2^-$
47.5	M1	3263(645)	$17/2^+ \rightarrow 15/2^-$
97.0	M1	649(83)	$19/2^+ \rightarrow 17/2^+$
125.9	M1	596(68)	$21/2^+ \rightarrow 19/2^+$
107.8	E1*	47(5)	$17/2^+ \rightarrow 15/2^-$
107.8	M1	280(32)	$17/2^+ \rightarrow 15/2^-$
406.6	M1	248(27)	$15/2^- \rightarrow 13/2^-$
466.9	M1	100(23)	$15/2^- \rightarrow 13/2^-$
495.2	E1	51(11)	$17/2^+ \rightarrow 15/2^-$
818.6	M1	6(1)	$15/2^- \rightarrow 13/2^-$
878.9	M1	12(1)	$15/2^- \rightarrow 13/2^-$

The error on A_{RSAM} is calculated as [127]:

$$\sigma = \frac{2}{N_{tot}^2} \sqrt{L^2 \sigma_R^2 + R^2 \sigma_L^2}, \quad (4.1)$$

where L is the number of counts at 85° , R is the number of counts at 95° , $N_{tot} = R + L$ is the total number of counts at 95° and 85° , σ_L and σ_R are the statistical errors at 85° and 95° respectively. The A_{RSAM} values for the transitions below the $17/2^+$ state were found to be $\sim 2.5\%$, while the A_{RSAM} values for the transitions above the $17/2^+$ state are close to zero. The obtained A_{RSAM} values from the coincidence spectra gated on 161.8, 316.7 and 125.9 keV transitions for a sample of transitions placed below and above the $17/2^+$ state are given in the TABLE. 4.4. Using the RSAM calibration [125] for $A_{RSAM} = 2.5\%$ and $\frac{v}{c} = 0.6\%$ the lifetime is estimated as $t_{1/2} = 0.6$ ns.

Band 4 is formed by a cascade of M1 transitions. This cascade was extended up to the $47/2^+$ level with a new 398.0 keV transition. The spectra gated on the 633.4 and 466.9 keV γ -rays illustrate most of the transitions that were placed in this band (see Fig. 4.7). Many transitions from this band are also visible in the spectrum gated on the 735.9 keV γ -ray (see Fig. 4.4). There is a 97.0 keV transition that was previously placed in coincidence with the 735.9 keV transition. We confirm this coincidence relationship, but modify the placement of the 97.0 keV transition, because it is also in coincidence with both the 406.6 keV and

TABLE. 4.4. Some energy transitions from the coincidence spectra gated on 161.7, 316.8 and 125.9 keV and the corresponding percentage of the RSAM anisotropy parameter A denoted respectively by $A_{g161.8}$, $A_{g316.7}$ and $A_{g125.9}$. A_{av} shows the weighted average for the obtained A values for each transition. The star sign (*) labels the A values for transitions below the $17/2^+$ state.

E_γ [keV]	$A_{g161.8}$ %	$A_{g316.8}$ %	$A_{g125.9}$ %	A_{av} %
97.0	-2.20(60)	0.34(27)	0.63(26)	0.25(18)
107.8	2.47(101)	2.80(167)	3.11(101)	2.79(66)*
125.9	-0.17(117)	-0.20(44)		-0.30(41)
149.5	-0.04(9)	-0.02(64)	-2.7(125)	-0.05(9)
161.8	-0.20(9)	0.59(19)	0.33(29)	-0.03(8)
206.4	0.07(58)	1.58(51)	-0.09(55)	0.59(31)
323.9	3.11(158)	3.31(132)	3.19(39)	3.19(36)*
392.5	2.05(111)	2.40(57)	2.00(78)	2.23(43)*
406.6	2.73(140)	2.65(99)	2.77(118)	2.71(67)*
466.9	1.82(12)	1.99(59)	2.26(25)	1.91(11)*
495.2	1.99(103)	1.47(34)	2.31(73)	1.65(30)*
716.4	2.94(141)	2.64(144)	3.15(51)	3.08(46)*
735.9	3.11(26)	2.49(84)	2.83(26)	2.95(18)*

the 466.9 keV transitions, in contrast to its previous placement in anti-coincidence with the 406.6 keV transition. The placement of the 478.5 keV γ -ray was also revised. It was found that it is in coincidence with only one 316.7 keV ($27/2^+ \rightarrow 25/2^+$) transition, which is different from its previous placement in anti-coincidence with both 316.7 keV transitions.

Most importantly the placement of one band, now called Band 5 (see Fig. 4.1) was revised. This band was previously placed above the 735.9 keV transition, but we found that it feeds the levels above the 672.5 keV γ -ray. The 238.5 and 221.6 keV transitions belonging to Band 5 are clearly visible in the 672.5 keV gate (see Fig. 4.4). This band is of particular interest to us as it can be involved in a possible chiral structure.

The coincidence data show that the 161.8 and 316.7 keV peaks are both doublets consisting of two transitions in coincidence and with the same energy. Another doublet of two transitions with similar energies of 599.3 keV and 601.0 keV also belong to this band. The placement of the 149.5 keV γ -ray was revised and two new 818.6 and 878.9 keV transitions decaying toward Band 1 were identified. A new 685.7 keV transition was added as parallel

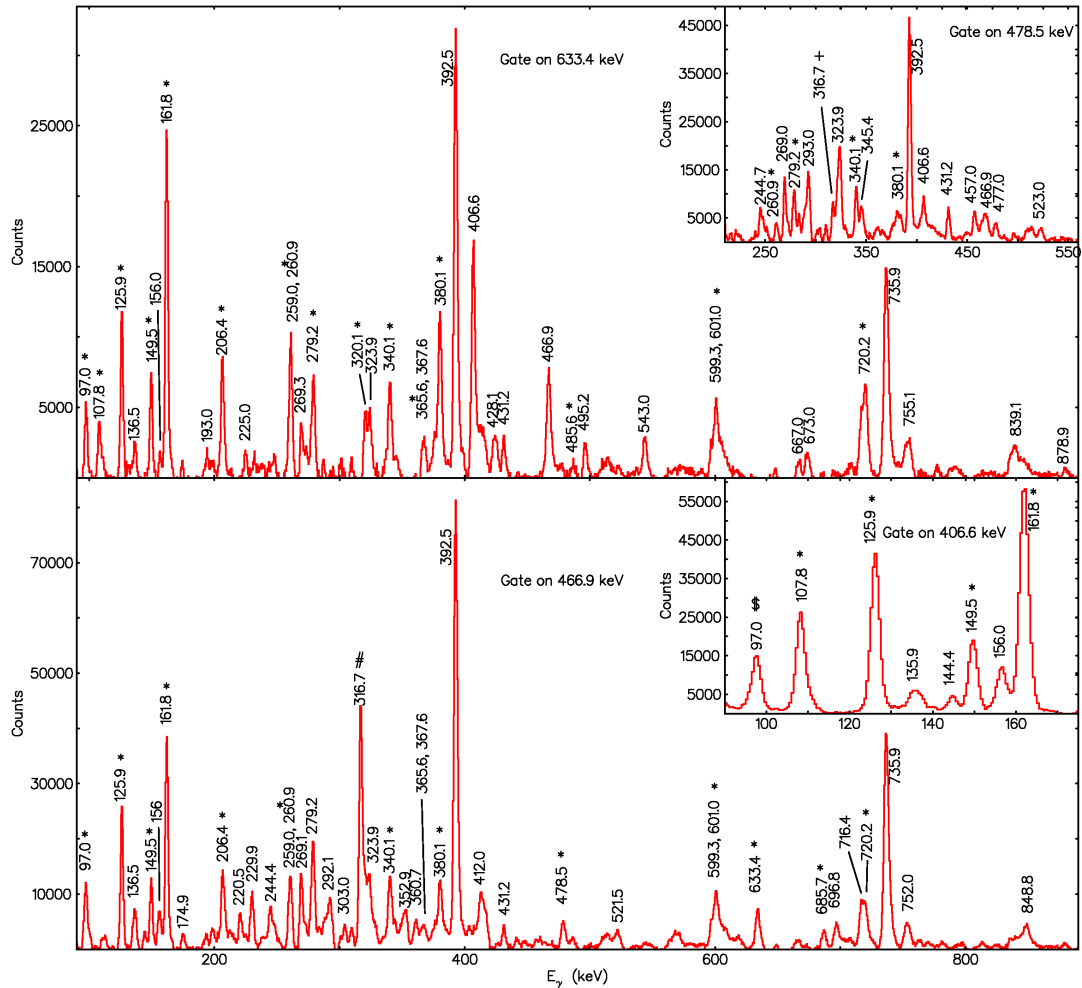


FIG. 4.7. Spectra showing the transitions as placed in Band 4. The \$ sign shows that the 97.0 keV transition is also in coincidence with the 406.6 keV transition. The plus sign (+) in the insert at the top shows the change of placement for the 478.5 keV transition since it is in coincidence with the 316.7 keV ($27/2^+ \rightarrow 25/2^+$) transition. The 316.7 keV peak is marked with # as it appears twice and is in anti-coincidence with the 633.4 keV transition. The other transitions placed in Band 4 are marked with *.

cross-over of the 365.6 and 320.1 keV transitions.

4.4.5 Band 5

Some transitions in this band were previously observed, but within a sequence that was feeding the $17/2^+$ state. The band is now placed at the negative parity side of the level scheme. Three new transitions of 929.0, 866.0 and 770.0 keV were identified as linking transitions and two new transitions of 159.0 and 151.0 keV were added to this band. The 374.0 keV transition was tentatively placed at the top of this band. The coincidence data used for the placement of the transitions in this band is illustrated in Fig. 4.8 and Fig. 4.9.

The spin and parity measurements suggest negative parity for this band. The angular distribution ratio and the linear polarization measurements show that the 866.0 and 770.0 keV transitions are respectively electric quadrupole and stretched magnetic dipole transitions. The existence of the 929.0 keV cross-over of the 159.0 and 770.0 keV stretched dipoles suggest magnetic nature for the 159.0 keV γ -ray. Since the linear polarization measurements were not possible at low energies, one can make comparison between the total intensities of the transitions depopulating the $29/2^-$ state and the total intensity of the 151 keV transition. Gating on 238.5 keV and assuming that the 151.0 keV transition is a stretched magnetic dipole, the obtained total intensities of the 151.0, 159.0 and 929.0 keV transitions are respectively 340(36), 237(19) and 34(7). If the 151.0 keV γ -ray is an electric dipole, its total intensity will be 104(10). Comparing these total intensities, one concludes that the 151.0 keV transition should be a magnetic dipole.

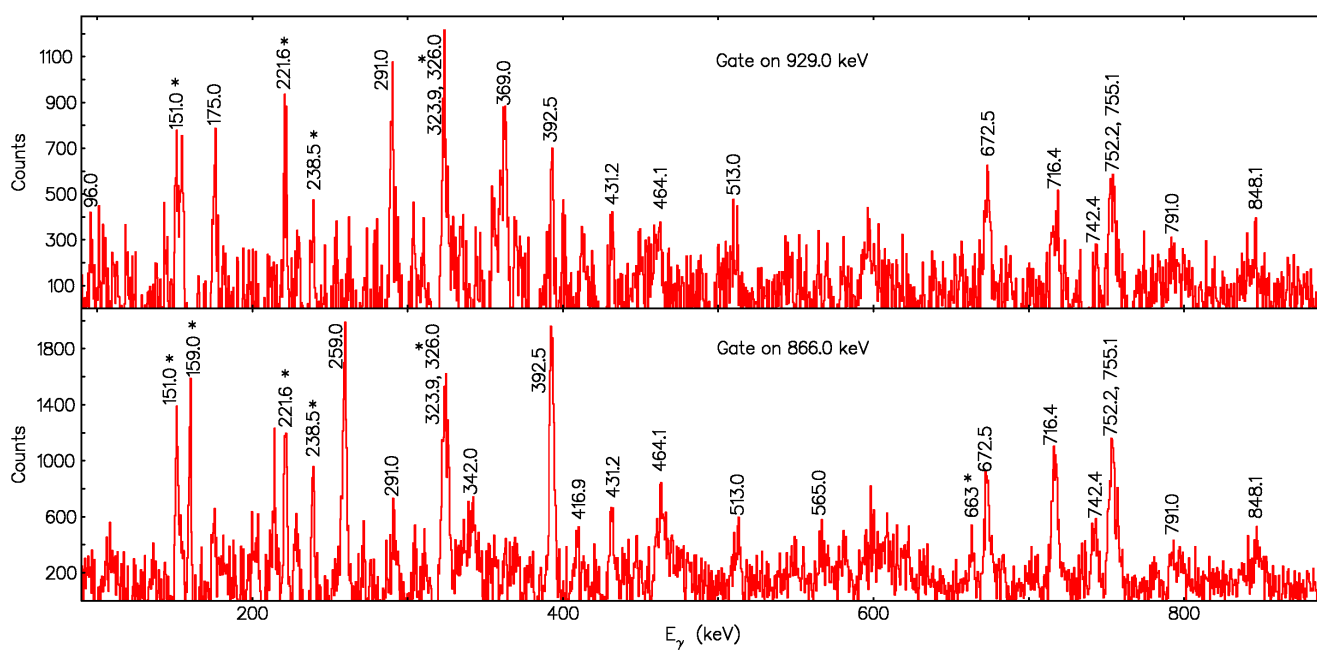


FIG. 4.8. Spectra gated on the 866.0 and 929.0 keV transitions illustrating the coincidence relationships in Band 5. The star sign (*) labels the transitions that were placed in Band 5.

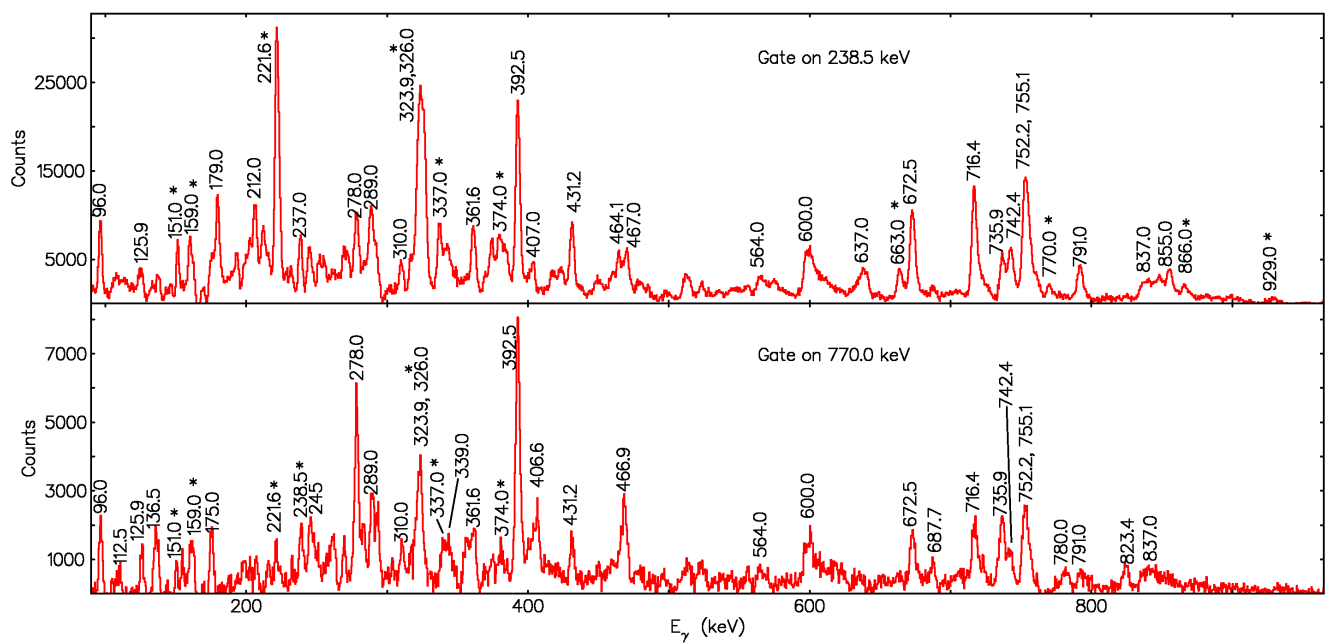


FIG. 4.9. Illustration of the coincidence data in Band 5. The star sign (*) labels the transitions placed in this band. The three linking transitions are visible in the spectrum gated on 238.5 keV.

4.4.6 Other sequences

Three other sequences were identified, but their parity could not be determined due to low statistics. One sequence consisting of 4 transitions is linked to Band 2 through the 111.0 keV transition. Two sequences are linked to Band 4. One of them shows a new 441.0 keV transition as a cross-over of a doublet of 220.5 keV transitions. The other sequence of 193.0 and 225.0 keV transitions is linked to Band 2 through 367.6 keV and 707.7 keV γ -rays.

4.5 ^{192}Tl Level scheme

Investigations performed in the past to study states of ^{192}Tl revealed an isomer with $I^\pi = 7^+$, $T_{1/2} = 11$ min [128]. Another study of high-spin states in ^{192}Tl through the $^{181}\text{Ta}(^{18}\text{O},7n)$ and $^{181}\text{Ta}(^{16}\text{O},5n)$ reactions found a band of 13 transitions based on the $I^\pi = 8^-$ isomeric state at 250.6 keV above the known long-lived 7^+ level [71].

The coincidence data that were produced in our experiment with a heavy-ion reaction of $^{160}\text{Gd}(^{37}\text{Cl},5n)$ at $E_{lab} = 167$ MeV were used for investigations of the excited states of ^{192}Tl . The previously known level scheme [71] was initially extended by more than 50 new transitions, see the MSc work of J. Easton [73]. However, spin and parity measurements were not performed.

In the present work, the data were further analyzed, and another 15 new transitions were found including one new band. Furthermore, most of the new levels were assigned spin and parity based on measurements of the angular distribution ratios and linear polarization anisotropies. The level scheme of ^{192}Tl constructed in this work is shown in Fig. 4.10 and the corresponding experimental results are summarized in TABLE. 4.5.

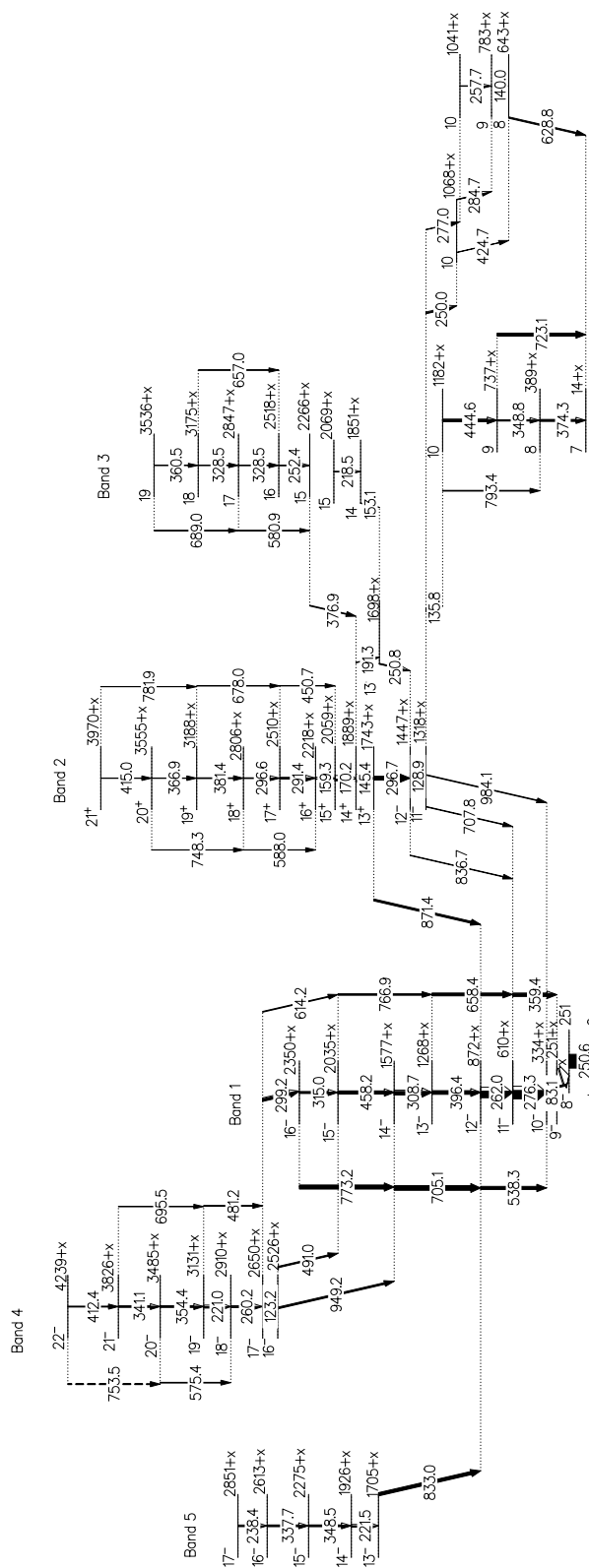


FIG. 4.10. The level scheme of ^{192}Tl , built in the present work.

TABLE. 4.5: List of the energies, total intensities, R_{AD} ratios, linear polarization anisotropies, γ -ray intensities, energies of the initial levels and corresponding assignments for γ -transitions in ^{192}Tl . An unobserved transition with energy "x" was suggested based on the systematics of odd-odd thallium isotopes. Values marked with @ correspond to unseparated doublet transitions, the measured value is for the total peak.

E_γ [keV]	I_t	R_{AD} ratio	A_{pol}	I_γ	E_{in} [keV]-x	$I_i^\pi \rightarrow I_f^\pi$
x					251	$9^- \rightarrow 8^-$
83.1					334	$10^- \rightarrow 9^-$
123.2	57(7)	0.81(11)		10(1)	2649	$17^- \rightarrow 16^-$
128.9	131(19)	0.75(17)		25(4)	1447	$12^- \rightarrow 11^-$
135.8	111(15)	0.93(21)		23(3)	1318	$11^- \rightarrow 10^-$
140.0	22(5)	0.91(17)		5(1)	783	$9^- \rightarrow 8^-$
145.4	255(22)	0.74(16)		63(5)	1889	$14^+ \rightarrow 13^+$
153.1	18(4)	1.61(31)		5(1)	1851	$14 \rightarrow 13$
159.3	72(10)	0.54(19)		21(3)	2218	$16^+ \rightarrow 15^+$
170.2	172(18)	0.61(11)		58(6)	2059	$15^+ \rightarrow 14^+$
191.3	38(6)	0.67(14)		16(2)	1889	$14^+ \rightarrow 13$
218.5	14(2)	0.91(15)		7(1)	2069	$15 \rightarrow 14$
221.0	96(30)	0.84(20)	-0.16(5)	49(15)	3131	$19^- \rightarrow 18^-$
221.5	90(21)	0.74(13)	-0.23(5)	46(11)	1926	$14^- \rightarrow 13^-$
238.4	55(19)	0.93(13)	-0.18(5)	31(11)	2851	$17^- \rightarrow 16^-$
250.0	33(7) [@]			20(4) [@]	1318	$11^- \rightarrow 10^-$
250.6	701(92)	0.78(13)	0.09(3)	421(55)	251+x	$8^- \rightarrow 7^+$
250.8	33(7) [@]			20(4) [@]	1697	$13 \rightarrow 12^-$
252.4	19(2)	0.75(8)		11(1)	2518	$16 \rightarrow 15$
257.7	14(2)	0.60(16)		9(1)	1041	$10^- \rightarrow 9^-$
260.2	415(32) [@]	0.84(11) [@]	-0.12(2) [@]	259(20) [@]	2910	$18^- \rightarrow 17^-$
262.0	415(32) [@]	0.84(11) [@]	-0.12(2) [@]	259(20) [@]	872	$12^- \rightarrow 11^-$
276.3	402(73)	0.88(17)	-0.07(3)	267(48)	610	$10^- \rightarrow 9^-$
277.0	16(2)	0.75(9)		10(1)	1318	$11^- \rightarrow 10^-$
284.7	18(2)	0.89(9)		12(1)	1068	$10^- \rightarrow 9^-$
291.4	58(8)	0.80(9)	-0.08(2)	40(6)	2510	$17^+ \rightarrow 16^+$

TABLE. 4.5 – continued from previous page

E_γ [keV]	I_t	R_{AD} ratio	A_{pol}	I_γ	E_{in} [keV]-x	$I_i^\pi \rightarrow I_f^\pi$
296.6	32(5)	0.84(5)		22(4)	2806	$18^+ \rightarrow 17^+$
296.7	120(22)	0.69(10)	0.16(6)	118(22)	1743	$13^+ \rightarrow 12^-$
299.2	112(9)	0.85(9)	-0.11(2)	79(6)	2649	$17^- \rightarrow 16^-$
308.7	157(12)	0.73(18)	-0.12(3)	114(9)	1577	$14^- \rightarrow 13^-$
315.0	65(10)	0.91(13)	-0.05(3)	48(7)	2350	$16^- \rightarrow 15^-$
328.5	35(3) [Ⓐ]	0.81(17) [Ⓐ]		27(2) [Ⓐ]	2847	$17 \rightarrow 16$
328.5	35(3) [Ⓐ]	0.81(17) [Ⓐ]		27(2) [Ⓐ]	3175	$18 \rightarrow 17$
337.7	56(11)	0.91(21)		44(9)	2613	$16 \rightarrow 15$
341.1	50(5)	0.91(19)	-0.25(4)	39(4)	3826	$21^- \rightarrow 20^-$
348.5	59(14)	0.64(7)		46(11)	2275	$15^- \rightarrow 14^-$
348.8	42(7)	0.76(16)	-0.04(1)	33(6)	737	$9^- \rightarrow 8^-$
354.4	54(9)	0.86(12)		43(7)	3885	$20^- \rightarrow 19^-$
359.4	54(5)	1.46(34)		43(5)	610	$11^- \rightarrow 9^-$
360.5	5(1)	0.79(14)		4(1)	3536	$19 \rightarrow 18$
366.9	13(3)	0.73(17)	11(2)	11(3)	3555	$20^+ \rightarrow 19^+$
374.3	52(5)	0.79(14)	-0.03(2)	43(4)	389	$8^- \rightarrow 7^-$
376.9	30(3)	0.92(11)		25(2)	2266	$15 \rightarrow 14^+$
381.4	25(4)	0.60(10)	-0.06(2)	21(3)	3188	$19^+ \rightarrow 18^+$
396.4	303(25)	0.86(9)	-0.16(5)	254(21)	1268	$13^- \rightarrow 12^-$
412.4	30(4)	0.90(12)		26(3)	4239	$22^- \rightarrow 21^-$
415.0	15(2)	0.66(21)		11(2)	3970	$21^+ \rightarrow 20^+$
424.7	13(2)	1.48(17)		11(2)	1068	$10^- \rightarrow 8^-$
444.6	82(9)	0.76(12)	-0.03(1)	72(8)	1182	$10^- \rightarrow 9^-$
450.7	6(2)	1.15(21)		6(2)	2510	$17^+ \rightarrow 15^+$
458.2	104(17)	0.79(16)	-0.08(2)	92(15)	2035	$15^- \rightarrow 14^-$
481.2	27(3)	1.28(33)		26(3)	3131	$19^- \rightarrow 17^-$
491.0	44(7)	0.78(21)	-0.24(3)	40(6)	2526	$16^- \rightarrow 15^-$
538.3	102(8)	1.40(32)	0.19(6)	100(9)	872	$12^- \rightarrow 10^-$
575.4	27(5)	1.23(15)		23(4)	3485	$20^- \rightarrow 18^-$
580.9	6(1)	1.63(24)		5(1)	2847	$17 \rightarrow 15$
588.0	10(1)	1.36(16)		10(1)	2806	$18^+ \rightarrow 16^+$

TABLE. 4.5 – continued from previous page

E_γ [keV]	I_t	R_{AD} ratio	A_{pol}	I_γ	E_{in} [keV]-x	$I_i^\pi \rightarrow I_f^\pi$
614.2	26(6)	1.36(16)		26(6)	2526	$17^- \rightarrow 15^-$
628.8	43(10)	0.92(20)	-0.06(1)	41(10)	643	$8^- \rightarrow 7^-$
657.0	6(1)	1.24(20)		6(1)	3175	$19 \rightarrow 17$
658.4	91(8)	1.37(25)	0.10(2)	90(8)	1268	$13^- \rightarrow 11^-$
678.0	6(2)	1.39(26)		6(2)	3188	$19^+ \rightarrow 17^+$
689.0	5(1)			5(1)	3536	$19 \rightarrow 17$
695.5	12(3)	1.31(18)		12(3)	3826	$21^- \rightarrow 19^-$
705.1	150(55)	1.39(8)	0.09(4)	147(54)	1577	$14^- \rightarrow 12^-$
707.8	17(2)	1.34(16)		17(2)	1318	$11^- \rightarrow 11^-$
723.1	97(10)	1.19(9)	0.21(6)	96(10)	737	$9^- \rightarrow 7^-$
748.3	9(2)	1.55(17)		9(2)	3555	$20^+ \rightarrow 18^+$
753.5	43(14)	1.36(15)		43(14)	4239	$22^- \rightarrow 20^-$
766.9	48(10)	1.23(16)	0.12(4)	48(10)	2035	$15^- \rightarrow 13^-$
773.2	130(27)	1.28(9)	0.08(2)	129(27)	2350	$16^- \rightarrow 14^-$
781.9	3(1)			3(1)	3970	$21^+ \rightarrow 19^+$
793.4	26(4)	1.11(9)	0.03(1)	26(4)	1182	$10^- \rightarrow 8^-$
833.0	74(10)	0.55(11)	-0.09(3)	72(10)	1705	$13^- \rightarrow 12^-$
836.7	16(3)	0.55(11)		16(3)	1447	$12^- \rightarrow 11^-$
871.4	62(11)	0.75(17)		62(11)	1743	$13^- \rightarrow 12^-$
949.2	55(13)	1.41(24)		55(13)	2526	$16^- \rightarrow 14^-$
984.1	21(4)	1.13(23)	0.13(5)	21(4)	1318	$11^- \rightarrow 9^-$

4.6 ^{192}Tl bands and spectra

4.6.1 Band 1

Band 1 is the yrast band built on top of the previously known 8^- isomeric state. It consists of 16 transitions and 10 states. Two new transitions were added in this band following

the analysis of our data. In most cases the placement of transitions of M1 character is supported by observation of corresponding cross-overs of E2 character. Gates on the 458.2 and 275.8 keV transitions given in FIG. 4.11 show the transitions of Band 1 in ^{192}Tl . An 83.1 keV transition was observed on the shoulder of the 82.5 keV X-rays and placed below the 276.3 keV transition.

An unobserved transition with energy “x” was suggested based on the systematics of the odd-odd thallium isotopes. It is known that transitions of low energies belong to the bottom of the yrast bands in these nuclei. However, these low energy transitions have large internal conversion coefficients so that some of them may not be seen. In order to figure out whether such low energy transitions should be present, one can analyze the systematics trend of the decay transitions in these nuclei. Comparison was made involving the decay transitions in the yrast bands of ^{190}Tl , ^{192}Tl , ^{194}Tl , ^{196}Tl and ^{198}Tl . In the spin range of 9 to $17\hbar$ that was considered, a similar decay trend was observed (see FIG. 4.12), assuming that an additional low energy transition is present in ^{192}Tl . Such low energy transitions were observed in ^{194}Tl , ^{196}Tl and ^{198}Tl nuclei. That is the transition labeled “x” in ^{192}Tl .

4.6.2 Band 2

Band 2 is a new band in comparison with the level scheme of Ref. [71]. It has positive parity and consists of 9 states and 13 transitions. It is a rotational band with intensity that flows only partly towards Band 1. Another decay path feeds a group of levels including several states with spins between 7 and 11. The angular distribution and the linear polarization measurements indicate that the band consists of M1 transitions and parallel E2 cross-overs.

One observes a number of doublets in the level scheme of ^{192}Tl , such as 250.8 keV ($13^- \rightarrow 12^-$) and 250.0 keV ($11^- \rightarrow 10^-$) in Band 2, while 250.6 keV ($8^- \rightarrow 7^+$) decays out of Band 1. Other doublets are 296.7 keV ($13^+ \rightarrow 12^-$) and 296.6 keV ($18^+ \rightarrow 17^+$), and 277.0 and 276.3 keV. Some measurements were not possible for both members of these doublets. The transitions in Band 2 are illustrated in Fig. 4.13.

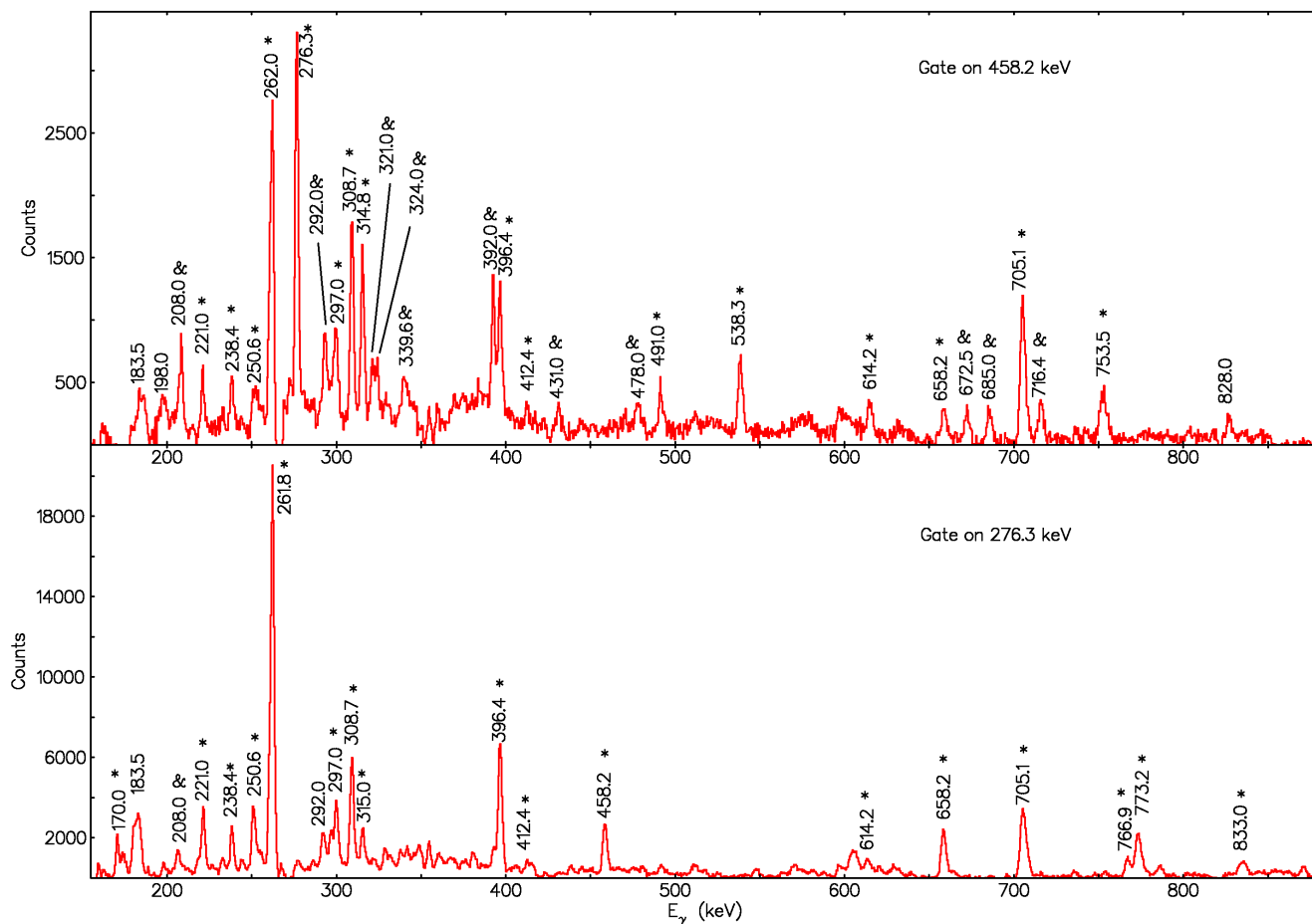


FIG. 4.11. Illustration of the transitions placed in Band 1 of ^{192}Tl . The star sign (*) labels the transitions belonging to ^{192}Tl , while & corresponds to some transitions of ^{193}Tl . The 538.3 keV cross-over of 262.0 keV and 276.3 keV appears strongly in the 458.2 keV gate but is not seen in the 276.3 keV gate. Similarly the 766.9 keV and 773.2 keV peaks are visible in the 276.3 keV gate, but disappear in the 458.2 keV gate, since they are placed in parallel to the 458.2 keV transition.

4.6.3 Band 3

This is a new band with respect to Ref. [71] decaying to Band 2 through the 376.9 keV transition. A total of 9 transitions and 7 states were observed in this band. The placement of the doublet 328.5 keV ($18 \rightarrow 17$ and $19 \rightarrow 18$) was supported by the observation of the 657.0 keV ($19 \rightarrow 17$) transition. The 580.9 keV ($18 \rightarrow 16$) and the 689.0 keV ($20 \rightarrow 18$) cross-overs correspond to the angular distribution ratios typical for stretched quadrupoles. Two transitions of 153.1 keV ($14 \rightarrow 13$) and 218.5 keV ($15 \rightarrow 14$) were observed and placed just above the 250.8 ($13 \rightarrow 12^-$) transition. The parity assignment for this band was not determined due to low statistics. Coincidence spectra for Band 3 are shown in Fig. 4.14.

4.6.4 Band 4

Band 4 is a new band with respect to the published level scheme of ^{192}Tl [71]. It consists of high spin states up to the state of $I^\pi = 22^-$. Band 4 decays to Band 1 through the 949.2 keV ($16^- \rightarrow 14^-$), 491.0 keV ($16^- \rightarrow 15^-$), 299.2 keV ($17^- \rightarrow 16^-$), and 614.2 keV ($17^- \rightarrow 15^-$) transitions. Illustration of coincidence data used to arrange the transitions in this band is given in Fig. 4.15.

4.6.5 Band 5

Band 5 is a new band with 4 transitions 221.5 keV ($14^- \rightarrow 13^-$), 348.7 keV ($15^- \rightarrow 14^-$), 337.7 keV ($16^- \rightarrow 15^-$), 238 keV ($17^- \rightarrow 16^-$), and 5 states. Analysis of the coincidence relationships and the relative intensities allowed the consecutive placement of transitions in this band. Coincidence spectra as used to arrange these transitions in Band 5 are shown in Fig. 4.16.

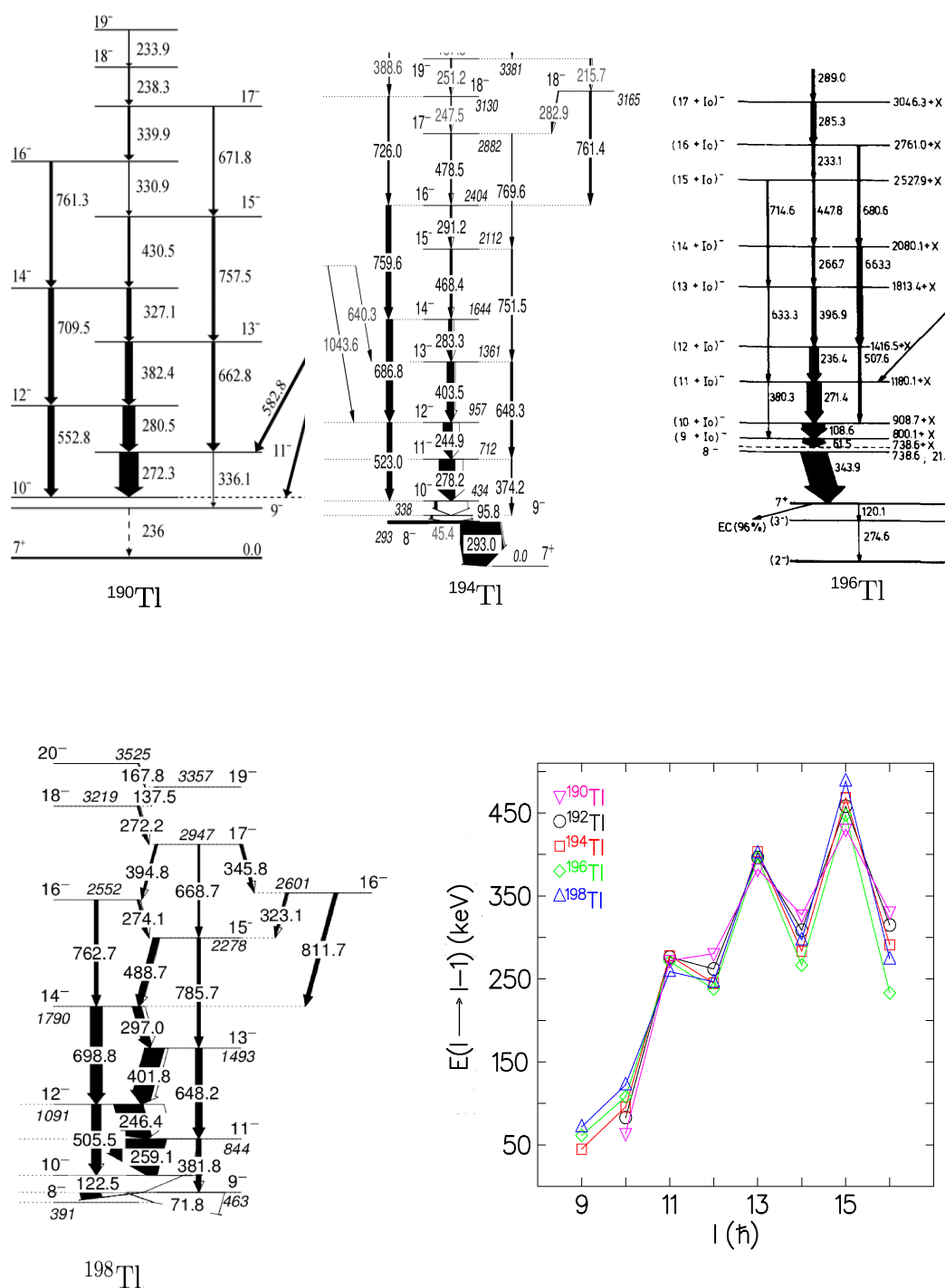


FIG. 4.12. Partial decay scheme of the yrast bands in ^{190}Tl [129], ^{194}Tl [58], ^{196}Tl [130] and ^{198}Tl [131]. The plot at the bottom right illustrates the systematics of the energies of the dipole transitions in the yrast bands in the odd-odd $^{190-198}\text{Tl}$ isotopes.

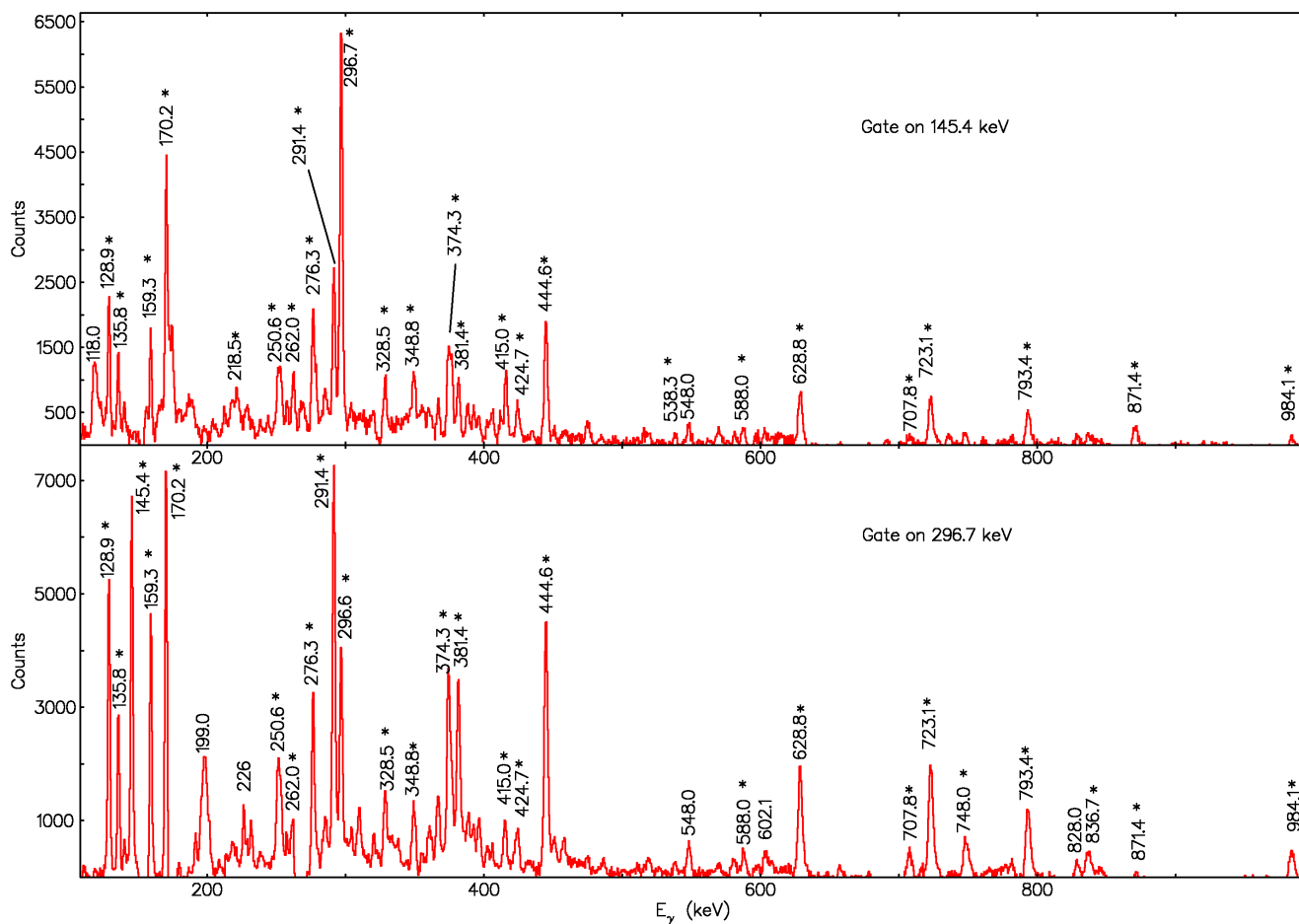


FIG. 4.13. Coincidence spectra for Band 2 of ^{192}Tl level scheme. All transitions marked with a star sign (*) were placed in this band. One observes an enhancement of the 296.7 keV peak in the 145.0 keV gate compared to the 296.6 keV gate since the doublet (296.6 and 296.7 keV) is in coincidence with the 145.0 keV transition while the 296.7 keV gate sees only the 296.6 keV transition. The transitions placed in the group of levels below the 11^- state are also visible in both gates.

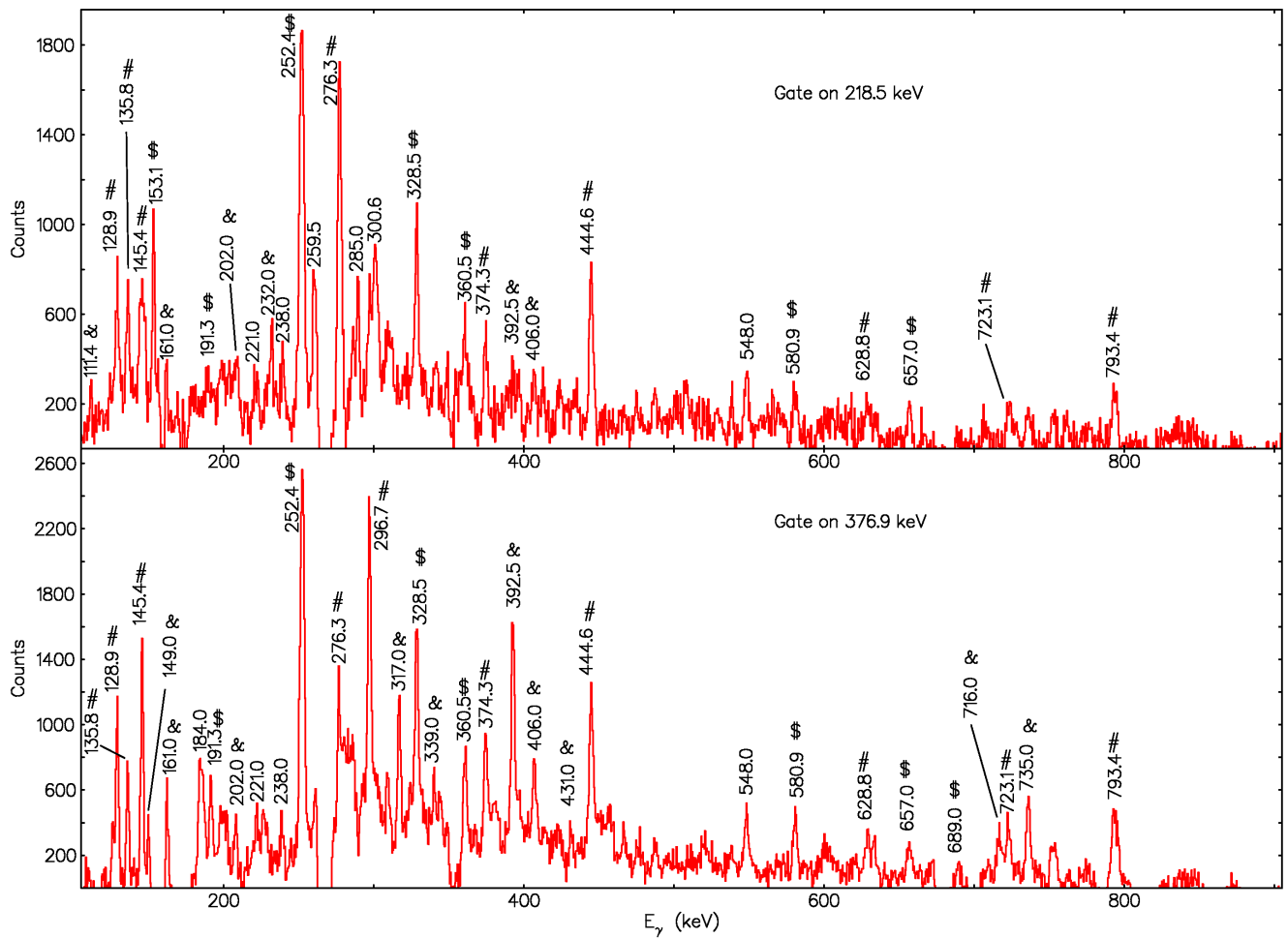


FIG. 4.14. Gated spectra illustrating transitions placed in Band 3 of ^{192}Tl . The dollar sign (\$) labels the transitions placed in Band 3. Transitions marked with # are in coincidence with Band 3 and are placed below the 13^- level. Transitions marked with & belong to ^{193}Tl .

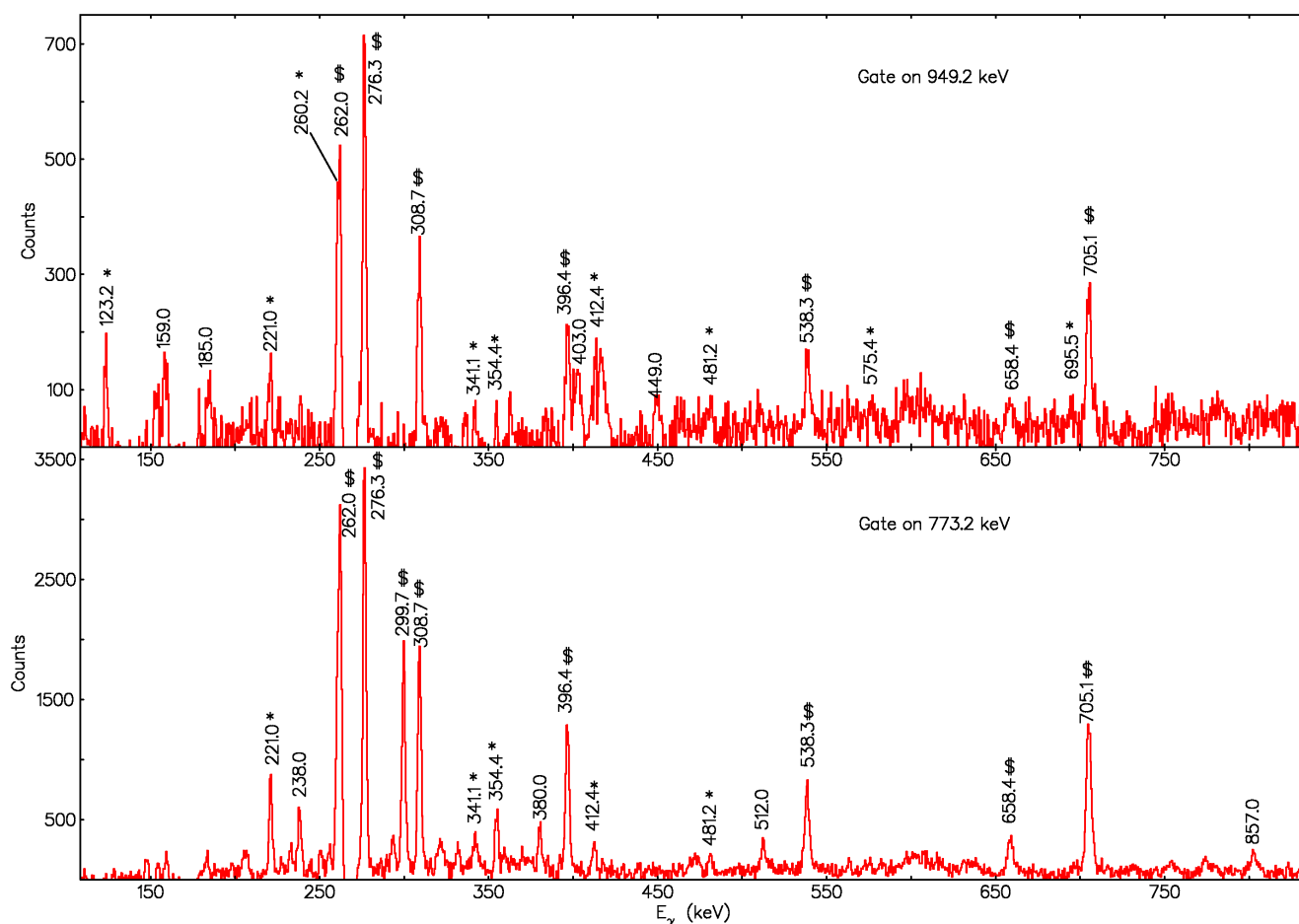


FIG. 4.15. Gated spectra showing transitions of Band 4 in ^{192}Tl . The star sign (*) labels the transitions placed in this band, while the dollar sign (\$) marks transitions placed in Band 1. One observes that the 123.2 keV peak is seen in the 949.2 keV gate but disappears in the 773.2 keV gate. Similarly, the observed 299.2 keV peak in the 773.2 keV gate is not visible in the 949.2 keV gate.

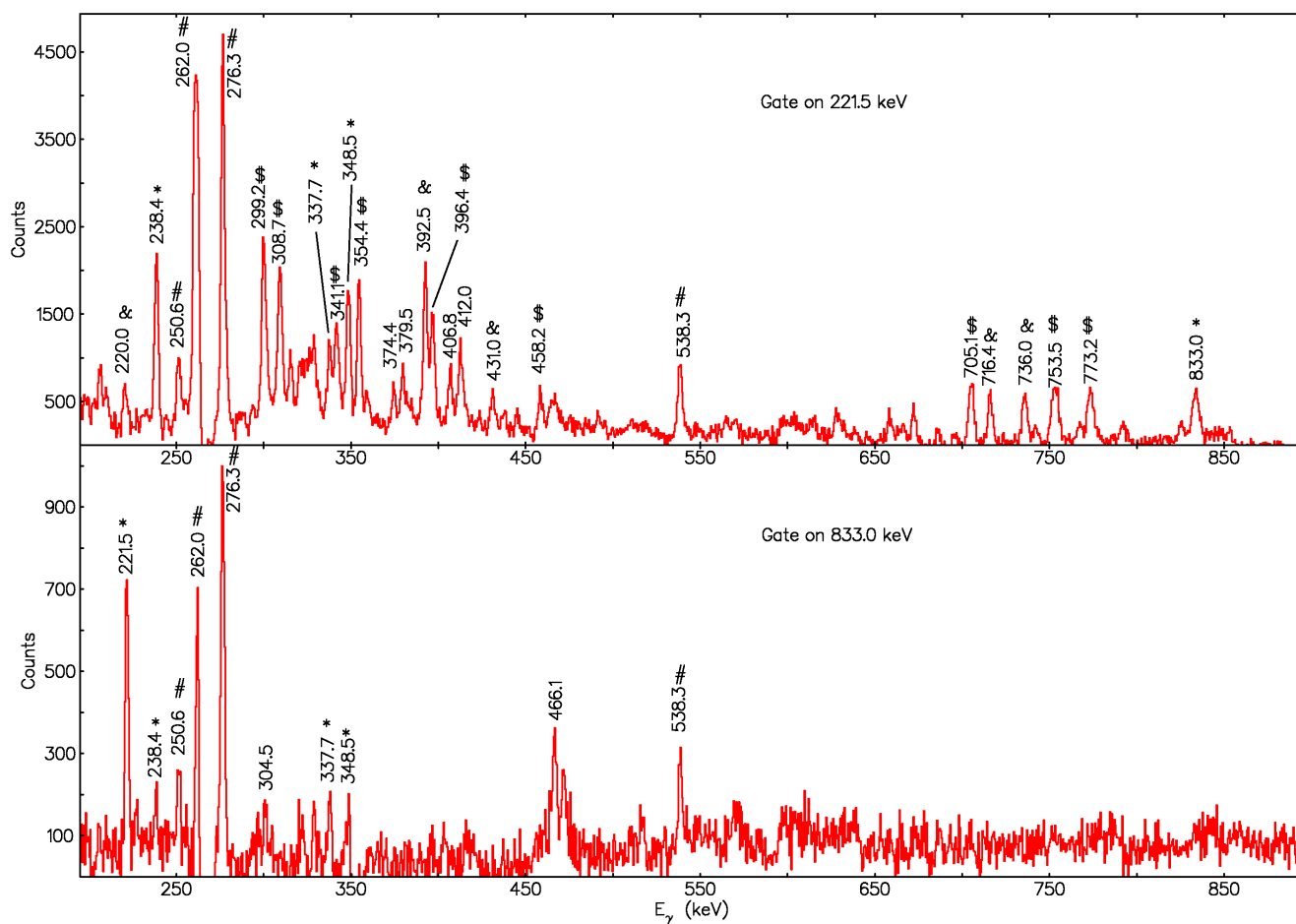


FIG. 4.16. Illustration of the transitions placed in Band 5 of ^{192}Tl . The star sign (*) labels the transitions placed in Band 5. Transitions marked with # are placed in Band 1. Since the 221.5 keV is a doublet, the dollar sign (\$) labels the transitions in coincidence with 221.0 keV that was placed in Band 4. Transitions labelled with & belong to ^{193}Tl .

4.7 Discussion

Experimental results for the two nuclei $^{192,193}\text{Tl}$ give more insights on the structure of the thallium isotopes in the $A \sim 190$ mass region. In the constructed level schemes, one observes a number of similar characteristics. Structures with different parity were identified in both nuclei. Each level scheme is made of 5 bands. These bands exhibit a rotational character and undergo band crossings when a neutron pair breaks and the angular momenta of the neutrons align along the rotational axis.

Possible chiral bands were identified in this work in both nuclei $^{192,193}\text{Tl}$. These are Bands 2, 3, and 5 in ^{193}Tl and Bands 1 and 5 in ^{192}Tl . More interestingly, a multiplet of chiral bands might be present in ^{193}Tl . Details about this possible multiplet are given in section 4.8.

In order to interpret the experimental results, a number of calculations were performed. Experimental alignments were extracted from the observed bands using Harris parameters of $J_0 = 8 \text{ MeV}^{-1}\hbar^2$ and $J_1 = 40 \text{ MeV}^{-3}\hbar^4$ as used in the corresponding Hg cores. The nuclear shape was described following calculations with the Cranked Nilsson Strutinsky (CNS) codes. In addition, the properties of the rotational bands were predicted using the multi-particle rotor (MPR) model and the two-quasiparticle-plus-triaxial rotor model (TQPRM). The calculations support the suggestion that chiral symmetry might be present.

4.7.1 Nucleon configurations of ^{193}Tl

The ^{193}Tl nucleus has $Z=81$ and $N=112$ with one proton short to fill the $Z=82$ shell and 14 neutrons away from filling the $N=126$ shell. Based on the Nilsson diagrams, the Fermi level for protons lies at the bottom of the $h_{9/2}$ shell while the Fermi level of neutrons lies at the upper part of the $i_{13/2}$ shell.

In the lowest lying states the unpaired proton in the $h_{9/2}$ shell is strongly coupled to the rotation of the core, with a maximum projection of the total angular momentum of the proton onto the short nuclear axis. Thus, Band 1 is a strongly coupled band. It is associated with a single-quasiproton $\pi h_{9/2}$ configuration and negative parity. As the angular momentum increases, the Coriolis force becomes stronger and induces a quasi-particle alignment of two neutrons resulting in a backbend, observed between Bands 1 and 2 (see Fig. 4.17).

In the case of ^{193}Tl two neutrons from the broken pair occupy $i_{13/2}$ orbitals and align along the long nuclear axis. The odd proton ($\pi h_{9/2}$) couples with these two neutrons ($\nu i_{13/2}^2$). The two neutrons will have different alignments of approximately $13/2$ and $11/2 \hbar$ due to the Pauli exclusion principle. The total angular momentum becomes $\sqrt{(9/2)^2 + (13/2 + 11/2)^2} \approx 25/2$. Indeed, Band 2 (see Fig. 4.1) has a band head near $25/2^-$. Thus, the negative parity Band 2 is associated with the $\pi h_{9/2} \otimes \nu i_{13/2}^2$ configuration. Such configuration is suitable for chiral symmetry, because the proton has a particle nature (occupies an orbital at the bottom of a shell) and its angular momentum aligns along the short nuclear axis, while the neutrons have hole nature (occupy orbitals at the upper part of a shell) and their angular momentum aligns along the long nuclear axis.

Bands 3 and 5 are also assigned a $\pi h_{9/2} \otimes \nu i_{13/2}^2$ configuration. In Fig. 4.17 the alignments of Bands 2, 3 and 5 in ^{193}Tl are compared with those of the yrast band in ^{193}Tl and the $\nu i_{13/2}^2$ band in the ^{192}Hg isotone [132]. The alignments of Bands 3 and 5 are very close to the alignment of the $\nu i_{13/2}^2$ band increased by the approximate alignment of the odd $h_{9/2}$ proton (see the dashed line in Fig. 4.17). This similarity in the alignments supports the proposed $\pi h_{9/2} \otimes \nu i_{13/2}^2$ configuration for Bands 3 and 5.

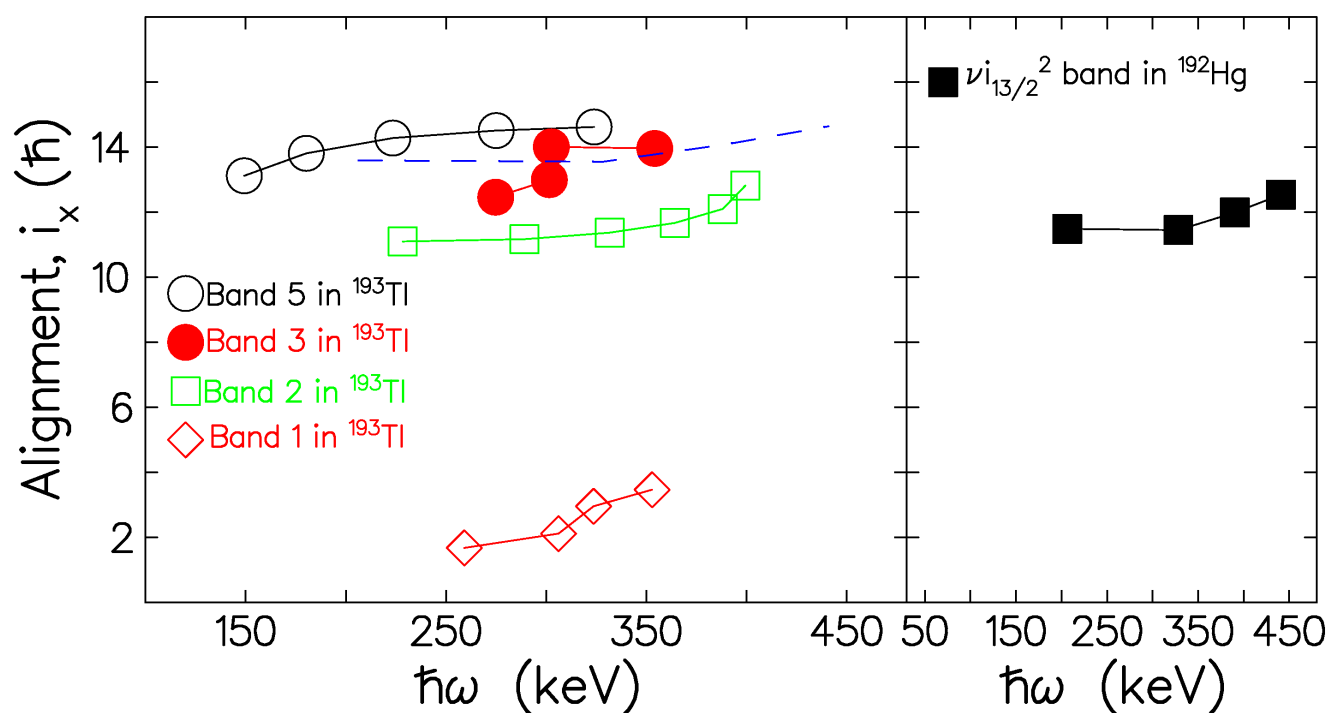


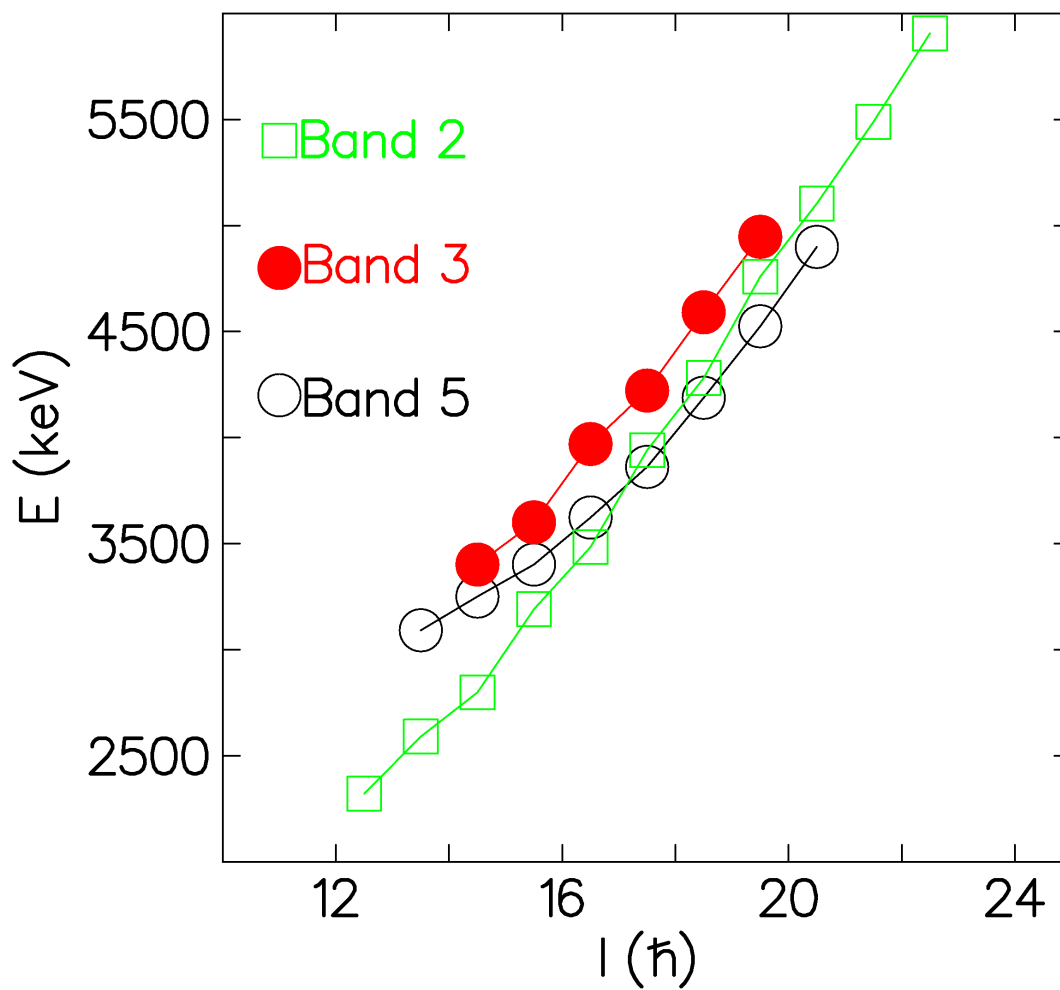
FIG. 4.17. Alignments of Bands 2, 3 and 5 built on the $\pi h_{9/2} \otimes \nu i_{13/2}^2$ configuration in ^{193}Tl compared with those of the $\nu i_{13/2}^2$ band in the ^{192}Hg isotone and the $\pi h_{9/2}$ band in ^{193}Tl . Harris parameters of $J_0 = 8\hbar^2/\text{MeV}$ and $J_1 = 40\hbar^4/\text{MeV}^3$ were used. The dashed blue line indicates the alignment of the $\nu i_{13/2}^2$ band in ^{192}Hg increased by $2.1 \hbar$, a value that corresponds to the approximate alignment of the odd $h_{9/2}$ proton.

The $B(M1)/B(E2)$ transition probabilities for the three bands are similar (see Fig. 4.19) supporting the suggestion that these bands involve a $\pi h_{9/2} \otimes \nu i_{13/2}^2$ configuration. Band 2 shows lower alignment than Bands 3 and 5 which is perhaps caused by not complete alignment of the three valence nucleons.

It should be noted that there are no other 3-quasiparticle configurations that can reproduce the negative parity and the high spin of these bands. Among the neutrons orbitals that lie close to the Fermi level we find the $i_{13/2}$, $p_{3/2}$, and $f_{5/3}$ orbitals. Two neutron configuration with positive parity and high alignment of $9 - 12 \hbar$ can only be constructed by $(i_{13/2})^2$. The alternative $(f_{5/2})^2$ configuration can contribute to a maximum alignment of $4 \hbar$ which is far too low in comparison with the experimental data, see Fig . 4.17.

The positive parity band (Band 4) involves negative parity low-j orbital. It can be associated with the $\pi h_{9/2} \otimes \nu i_{13/2} \nu j$ configuration, where $j=(3p_{1/2}, 2f_{5/2})$. The expected band head spin is $\sqrt{(9/2)^2 + (13/2 + 1/2)^2} \approx 17/2$ with positive parity. This is in good agreement with experiment since the positive parity structure starts at the $17/2^+$ level.

The nucleon configuration of two other sequences that were placed in the level scheme is unknown, since their parity assignment could not be determined due to low statistics.

FIG. 4.18. Experimental excitation energies of Band 2, 3 and 5 in ^{193}Tl .

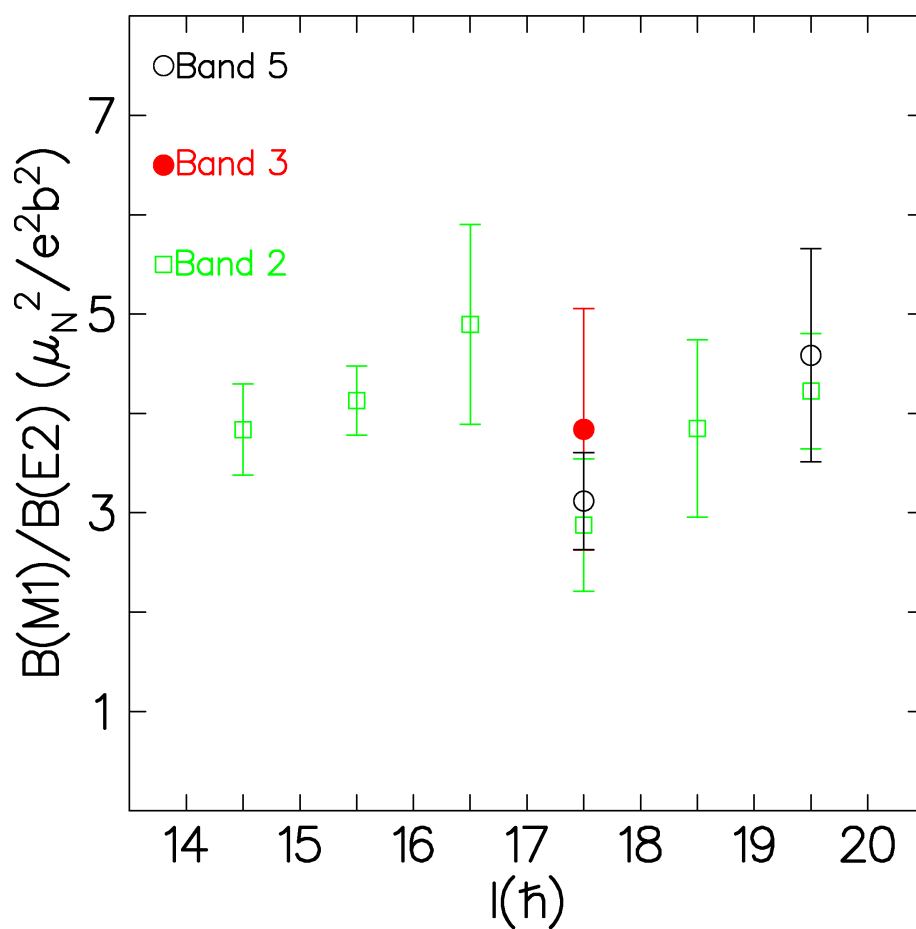


FIG. 4.19. Experimentally measured $B(M1)/B(E2)$ reduced transition probability ratios for Band 2, 3 and 5 in ^{193}Tl .

4.7.2 Nucleon configurations of ^{192}Tl

The level scheme of ^{192}Tl has similarities with ^{193}Tl . Band 1, 2 and 4 of ^{192}Tl resemble Band 1, 4 and 2 of ^{193}Tl respectively. Band 5 in ^{192}Tl could be a chiral partner of Band 1. The two bands have close excitation energies (see Fig. 4.21). At low spins their relative excitation energy is 437 keV, which decreases to 201 keV near $I \sim 17$. Concerning Band 3 in ^{192}Tl , its parity assignment could not be determined due to low statistics. Thus, the nature of this band is not known.

Investigations performed in the past revealed two isomers with $I^\pi = 2^-$, $T_{1/2} = 9.5$ min and $I^\pi = 7^+$, $T_{1/2} = 11$ min, and their subsequent EC/β^+ decay to ^{192}Hg [70]. The actual ground state is 2^- . Looking at the ^{192}Tl level scheme, 8^- is of prime interest since the rotational bands are based on it. One can look at the neighbouring nuclei in order to deduce possible configuration of Band 1. Filling the Nilsson diagram, ^{192}Tl has the same Fermi level of protons as ^{193}Tl in which the ground state band is strongly coupled and associated with $\pi h_{9/2}$ configuration and band head of $9/2^-$. On the other hand ^{191}Hg is a neighbouring isotope with the same Fermi level of neutrons as ^{192}Tl . Its ground state band is a decoupled band associated with $\nu i_{13/2}$ configuration [133] and band head of $13/2^+$. Therefore, if the unpaired proton and neutron in ^{192}Tl couple in the same way the band head spin will be given by $\sqrt{(9/2)^2 + (13/2)^2} \approx 8$, which is in good agreement with the experimental value. Thus, Band 1 can be associated with the $\pi h_{9/2} \otimes \nu i_{13/2}$ configuration.

When the nucleus rotates at higher frequency a pair of neutrons breaks and aligns along the rotational axis. In the case of ^{191}Hg three odd $i_{13/2}$ neutrons are aligned. Alignments for the three neutrons will be approximately $13/2$, $11/2$ and $9/2$. The roughly expected band head spin of the decoupled band in ^{191}Hg becomes $I = 13/2 + 11/2 + 9/2 = 33/2$. Coupling the unpaired proton to these three neutrons in the $\pi h_{9/2} \otimes \nu i_{13/2}^3$ configuration produces a band head spin of $\sqrt{(9/2)^2 + (33/2)^2} \approx 17$ with negative parity. Band 4 has a band head spin near the 16^- state. This band is associated with the $\pi h_{9/2} \otimes \nu i_{13/2}^3$ configuration.

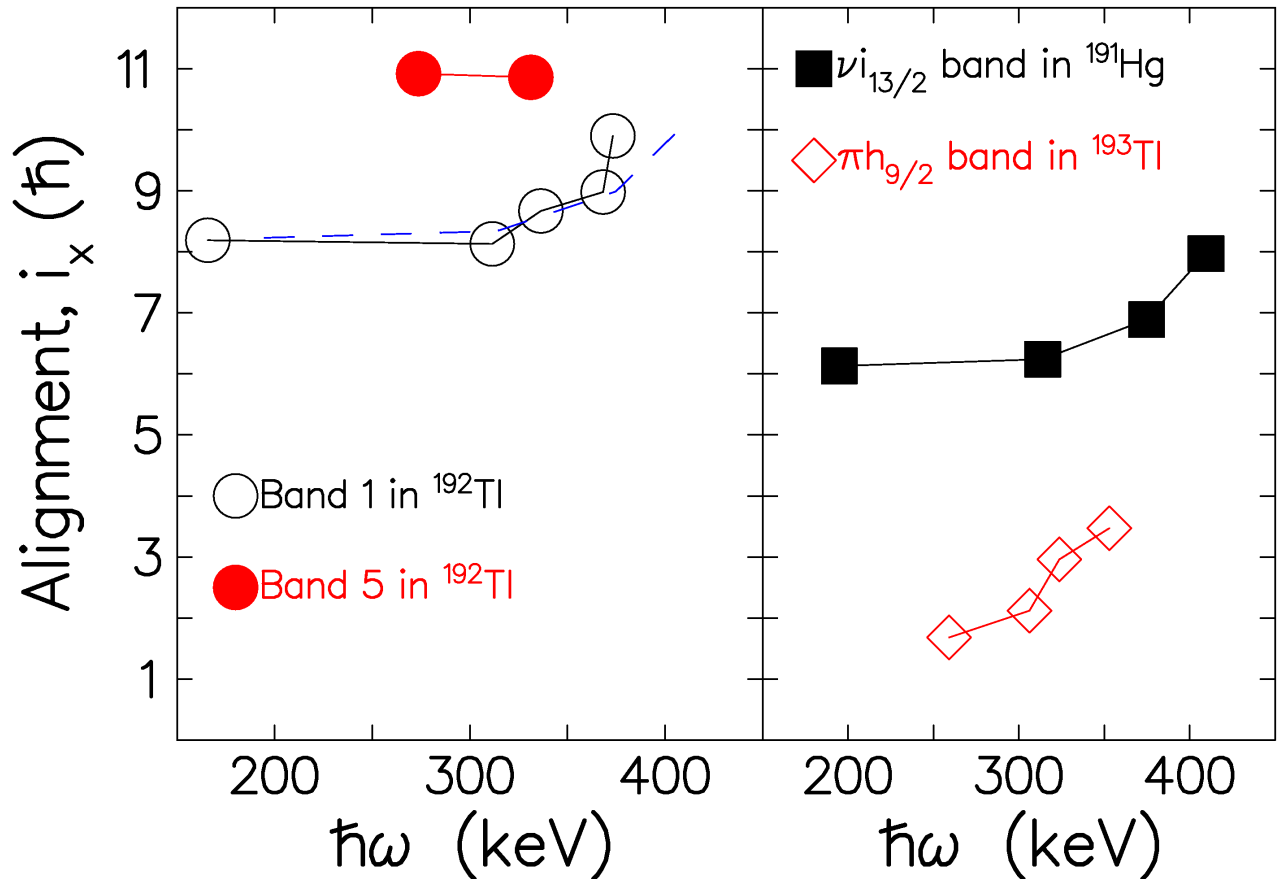


FIG. 4.20. Alignments of Bands 1 and 5 built on the $\pi h_{9/2} \otimes \nu i_{13/2}$ configuration in ^{192}Tl compared with those of the $\nu i_{13/2}$ band in the ^{191}Hg isotone and the $\pi h_{9/2}$ band in ^{193}Tl . Harris parameters of $J_0 = 8\hbar^2/\text{MeV}$ and $J_1 = 40\hbar^4/\text{MeV}^3$ were used. The dashed blue line indicates the alignment of the $\nu i_{13/2}$ band in ^{191}Hg increased by $2.1\hbar$, a value that corresponds to the approximate alignment of the odd $h_{9/2}$ proton.

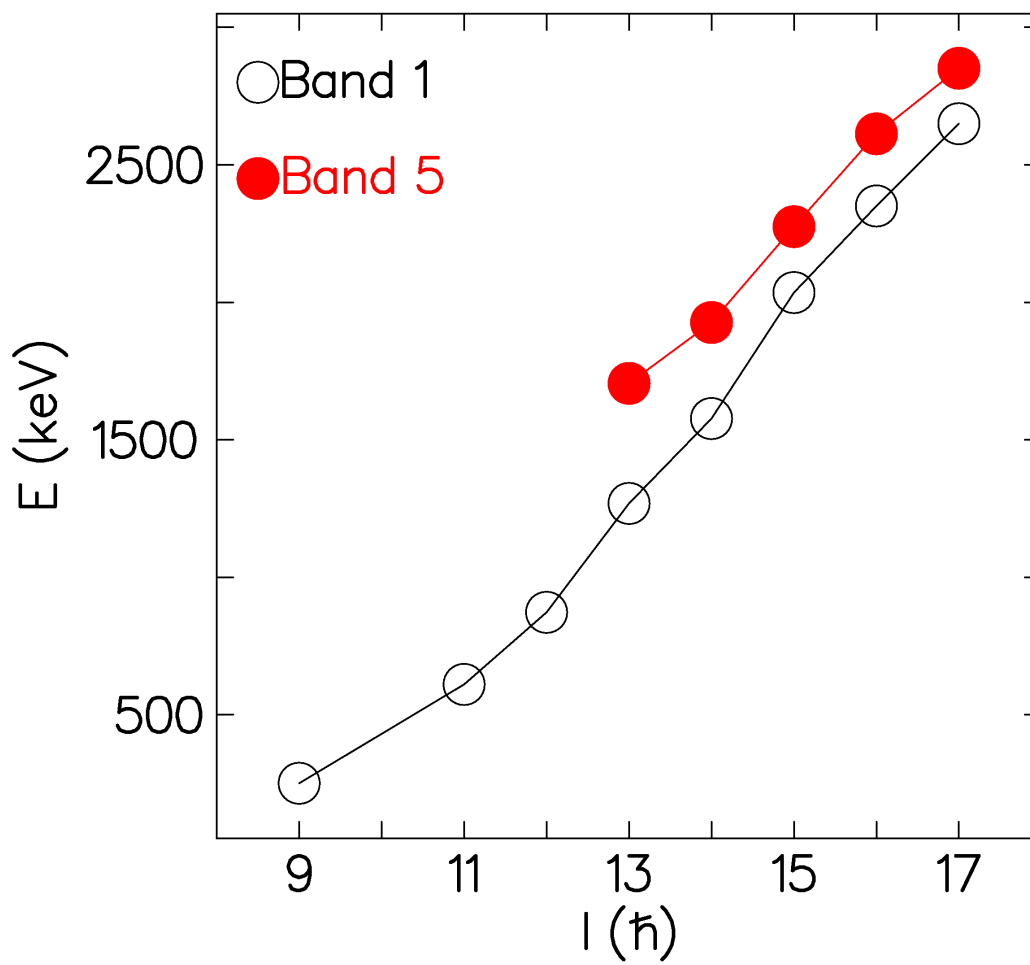


FIG. 4.21. Experimental excitation energies of Band 1 and 5 in ^{192}Tl

The positive parity sequence starts from the 13^+ state. This band involves three odd neutrons with one of them occupying a negative parity low j orbital, with $j = (3p_{1/2}, 2f_{5/2})$. The alignment of the three neutrons is probably $13/2 + 11/2 + 1/2 = 25/2$. The odd proton is coupled to the three neutrons. In this way the configuration becomes $\pi h_{9/2} \otimes \nu i_{13/2}^2 \nu j$. One can expect a band head spin given by $\sqrt{(9/2)^2 + (25/2)^2} \approx 13$ with positive parity. Thus, Band 2 is assigned the $\pi h_{9/2} \otimes \nu i_{13/2}^2 \nu j$ configuration.

4.8 Possible multiplet of chiral bands in ^{193}Tl

Since the theoretical introduction of chiral symmetry in nuclei [2], extensive work both from experimental and theoretical point of view have been conducted to seek for further understanding of chirality in nuclei. So far a number of nuclei have been suggested as chiral candidates, but no one shows perfect degeneracy in the chiral partner bands. These bands show similar properties, but the level of similarity differs from one nucleus to another.

Usually in order to identify whether a nucleus presents chiral symmetry, a suitable configuration should be involved, the nucleus should have triaxial shape and it must exhibit a pair of bands with near-degenerate properties. Prior to this work, Band 2 was suggested to have a configuration $\pi h_{9/2} \otimes \nu i_{13/2}^2$ which is suitable for chiral symmetry. An interesting point is that after our coincidence analysis three bands (Bands 2, 3 and 5) were found to exhibit somewhat similar properties and to correspond to the same $\pi h_{9/2} \otimes \nu i_{13/2}^2$ configuration. So it is possible that a multiplet of bands exists in ^{193}Tl in a similar way as the three bands found in ^{194}Tl . Band 2, 3 and 5 of ^{193}Tl are shown in Fig. 4.22. Figures 4.17, 4.18 and 4.19 display a comparison of the properties of Bands 2, 3 and 5, i.e.:

- (i) Bands 3 and 5 have similar alignments, while the alignment of Bands 2 is somewhat lower;
- (ii) The three bands have similar $B(M1)/B(E2)$ reduced transition probability ratios;
- (iii) The relative excitation energies are as low as $\Delta E = 151$ keV between Bands 3 and 5 at $I \sim 29/2^-$ and $\Delta E = 188$ keV at $I = 39/2^-$ for Bands 2 and 3, while Bands 2 and 5 cross each other. Candidate chiral bands that cross each other are of particular interest. Should two bands with the same parity cross, a specific phenomenon should be present, presumably a symmetry that prevents them from interacting with each other and repulsing

each other. Thus the three negative parity bands in ^{193}Tl are a very interesting case of possible chiral symmetry. On the other hand due to the crossing and the change of the relative position of the three bands it is not possible to identify unambiguously which two of them form a chiral pair. We consider that it is possible that two chiral systems exist in ^{193}Tl , each of them consisting of two bands, but at present one of these bands remains unobserved. Alternatively two of these bands may form a chiral system, while the third, which corresponds to the same nucleon configuration might not be chiral. In the latter case however it remains unclear what may cause this difference. In the following the negative parity bands in ^{193}Tl are studied using theoretical calculations.

Calculations were carried out for ^{193}Tl using the Cranked Nilsson-Strutinsky codes. Potential energy surfaces as a function of spin were calculated and the minima indicate a moderately deformed ($\varepsilon_2 \sim 0.15$) shape (see Fig. 4.23). In particular at spin of $I=14.5$ we observe an absolute minimum for triaxiality of $\gamma \sim -45^\circ$. This triaxiality persists at higher spins and shows that a rotation around the intermediate axis is dominant in this spin range.

In addition, calculations for these bands were performed with the multi-particle rotor model. We have used the standard parameters for the Nilsson potential without residual interaction. A quadrupole deformation $\varepsilon_2 = 0.15$ and a non-axiality parameter $\gamma \sim -45^\circ$ corresponding to the absolute minimum of the potential energy as obtained with CNS codes were considered. The electromagnetic transition probabilities were calculated with the spin g-factor g_s for both proton and neutron set to 0.6. The core g-factor g_R was taken as 0.3.

The code does not describe well the excitation energies of the three negative parity bands in ^{193}Tl . The calculated bands show much lower relative excitation energies than the experimentally observed bands. It is expected that the lack of pairing in the model might be the cause of this discrepancy. However we are mostly interested whether the calculations would predict a 3 dimensional chiral geometry of the angular momenta and these are probably not influenced much by pairing.

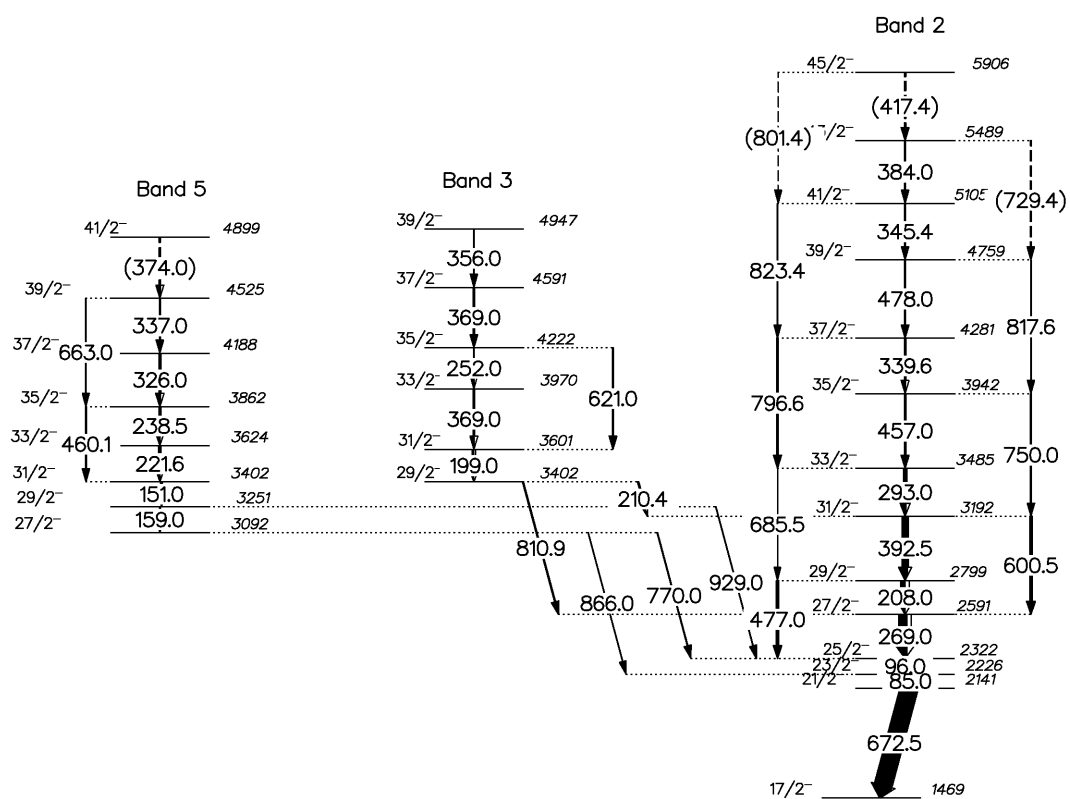


FIG. 4.22. Partial level scheme of ^{193}Tl showing the three bands with close-similarity.

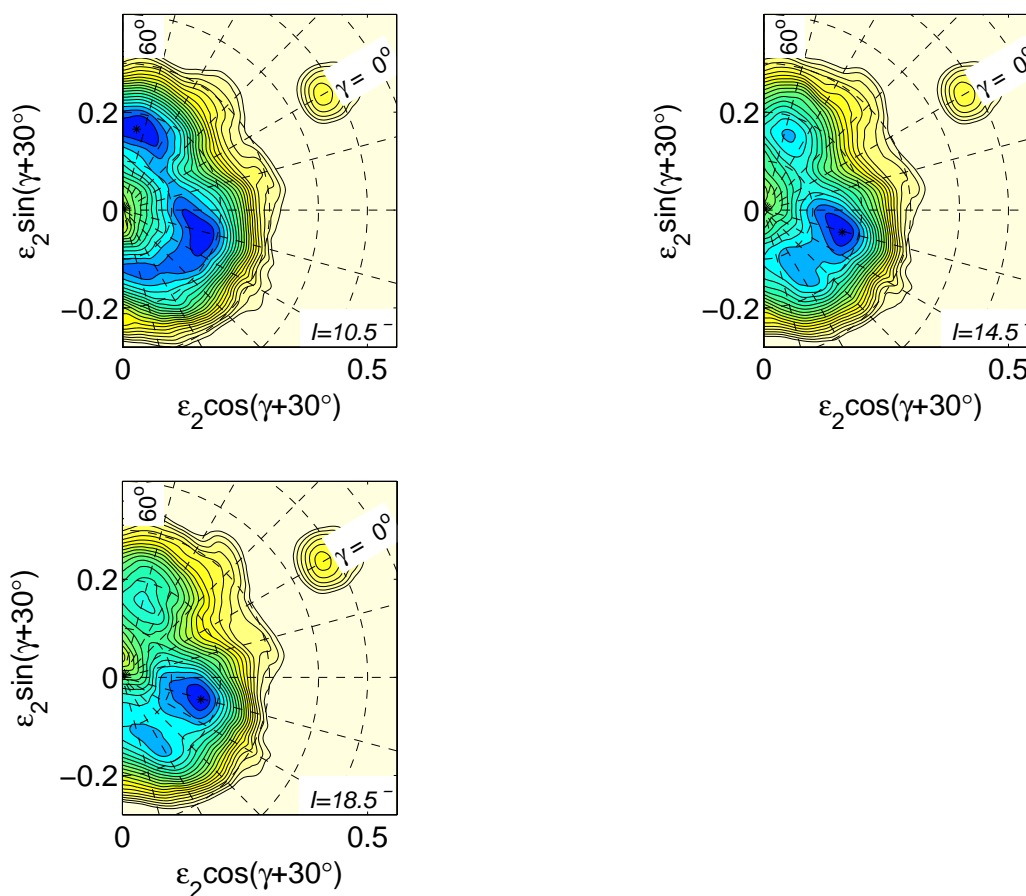


FIG. 4.23. Potential energy surfaces for the negative parity bands ^{193}Tl as a function of the nuclear deformation for three different values of the spin.

The calculated total angular momentum for ^{193}Tl is aplanar having large projections on all three nuclear axes (see Fig. 4.25 and Fig. 4.26). The angular momentum of the core has larger component along the intermediate axis. The major contribution from the proton angular momentum is observed along the short axis (x -axis), and from the neutron angular momentum along the long axis (z -axis). Thus, the observed aplanar system fulfills the requirement of chiral geometry and supports the existence of chiral symmetry in ^{193}Tl .

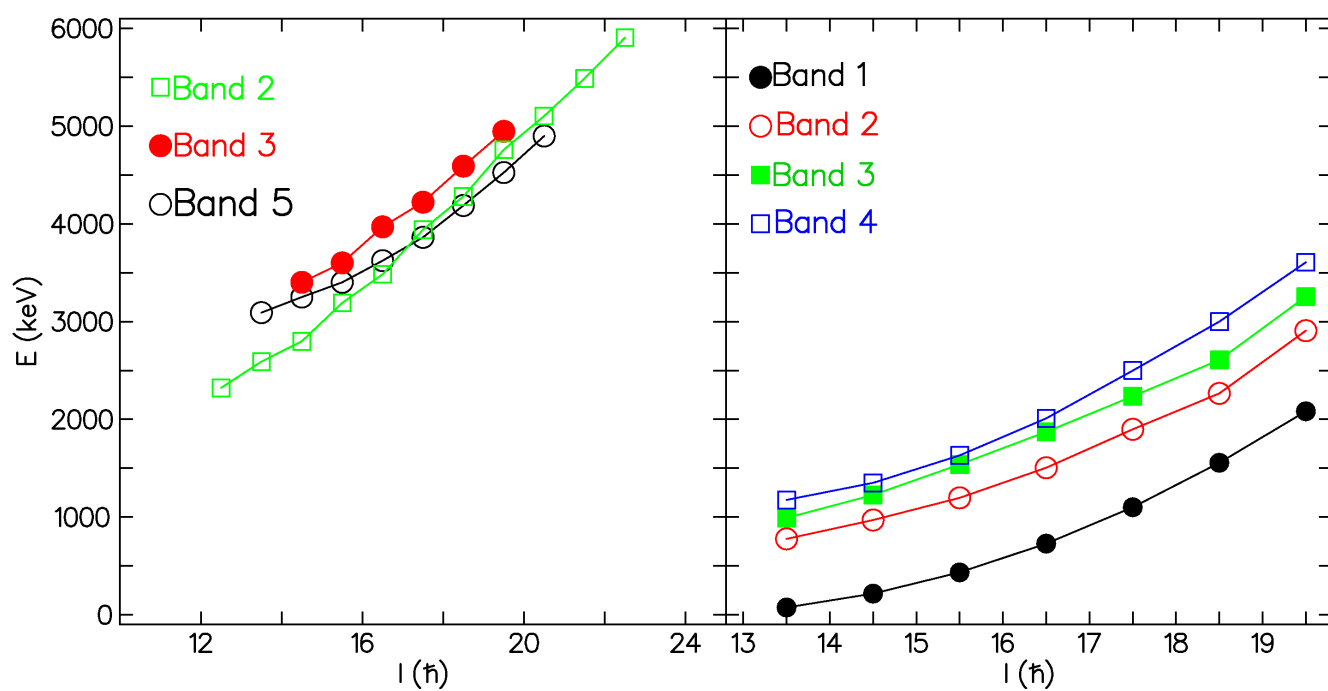


FIG. 4.24. Experimental (left panel) and theoretical (right panel) excitation energies in ^{193}Tl .

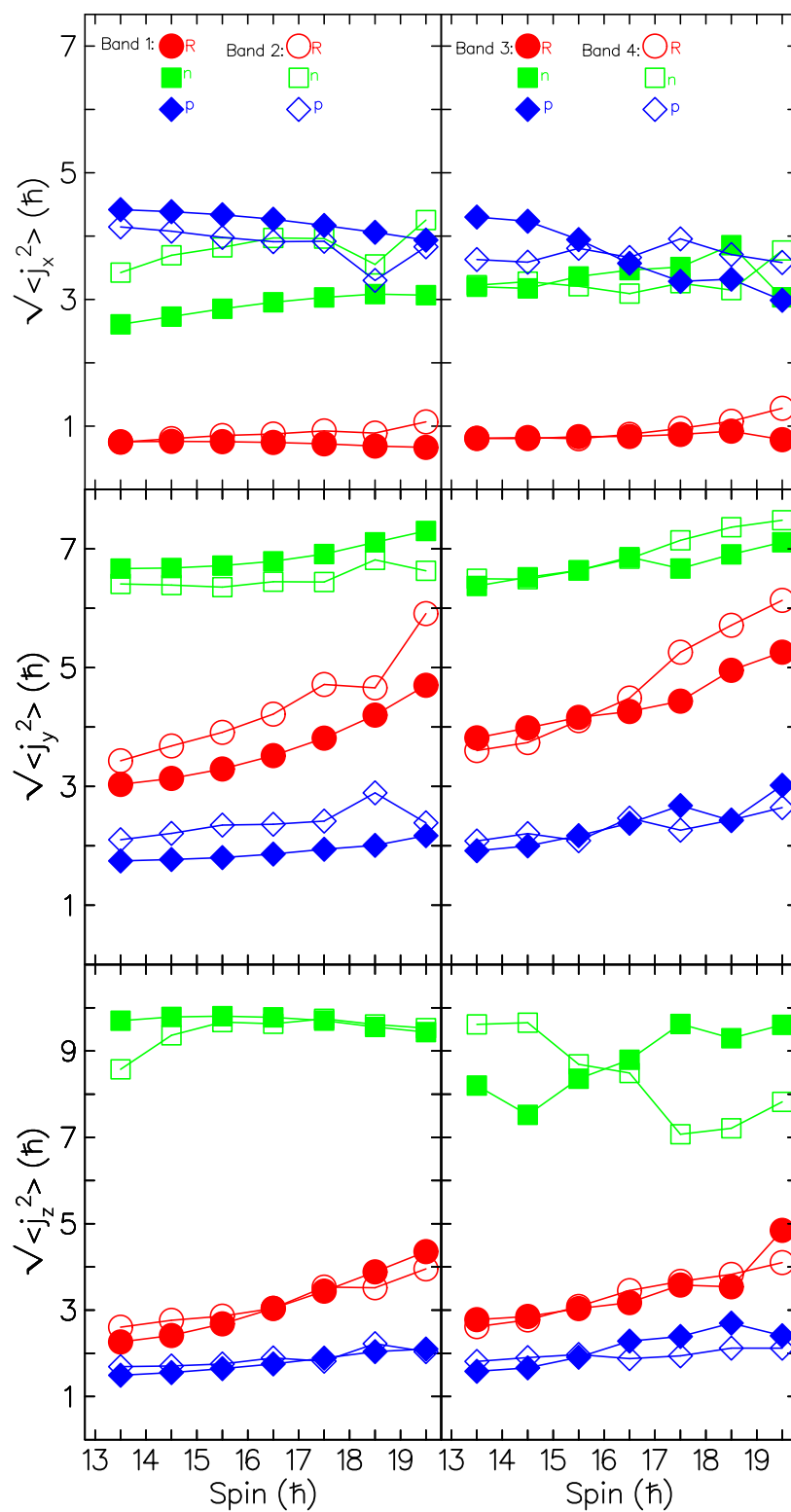


FIG. 4.25. Plot of the components for the angular momenta of the core (R), the protons (p) and the neutrons (n) in ^{193}Tl as produced with calculations using the MPR model.

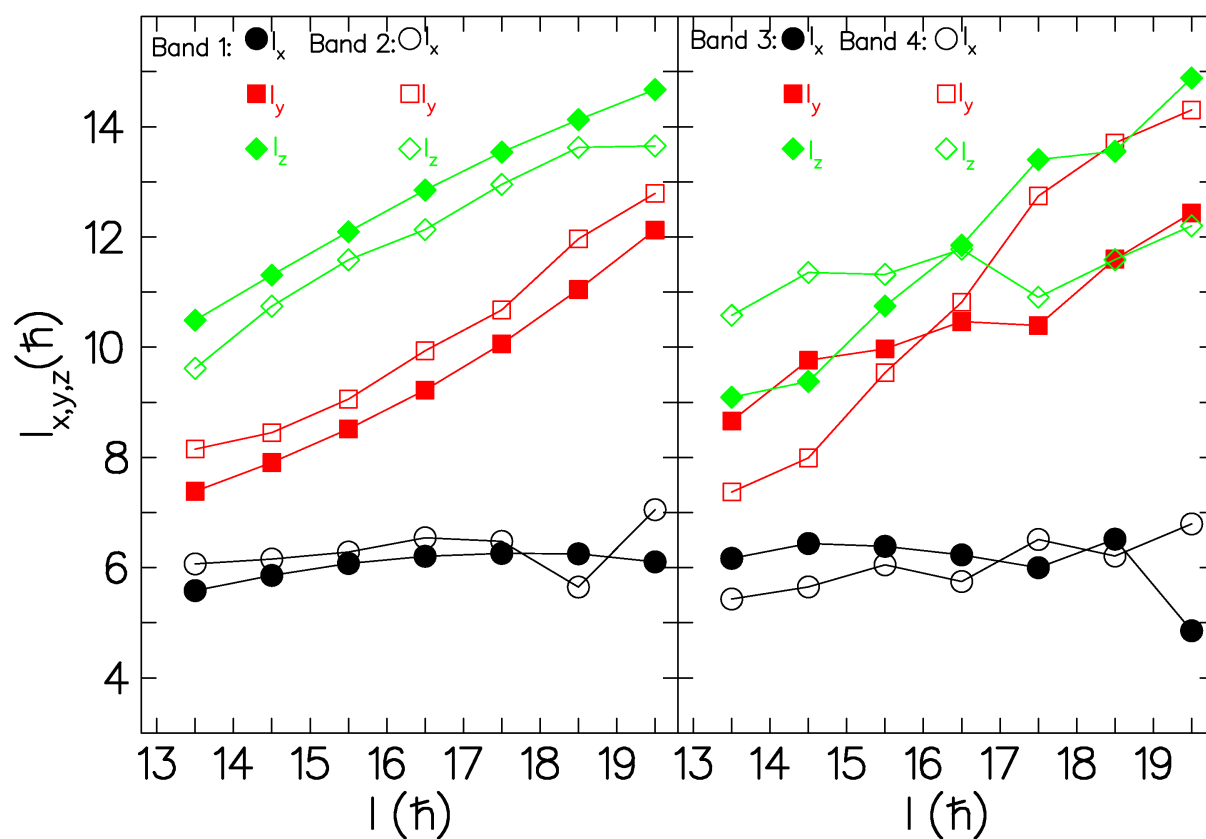


FIG. 4.26. Plot of the components for the total angular momentum in ^{193}Tl as produced with calculations using the MPR model.

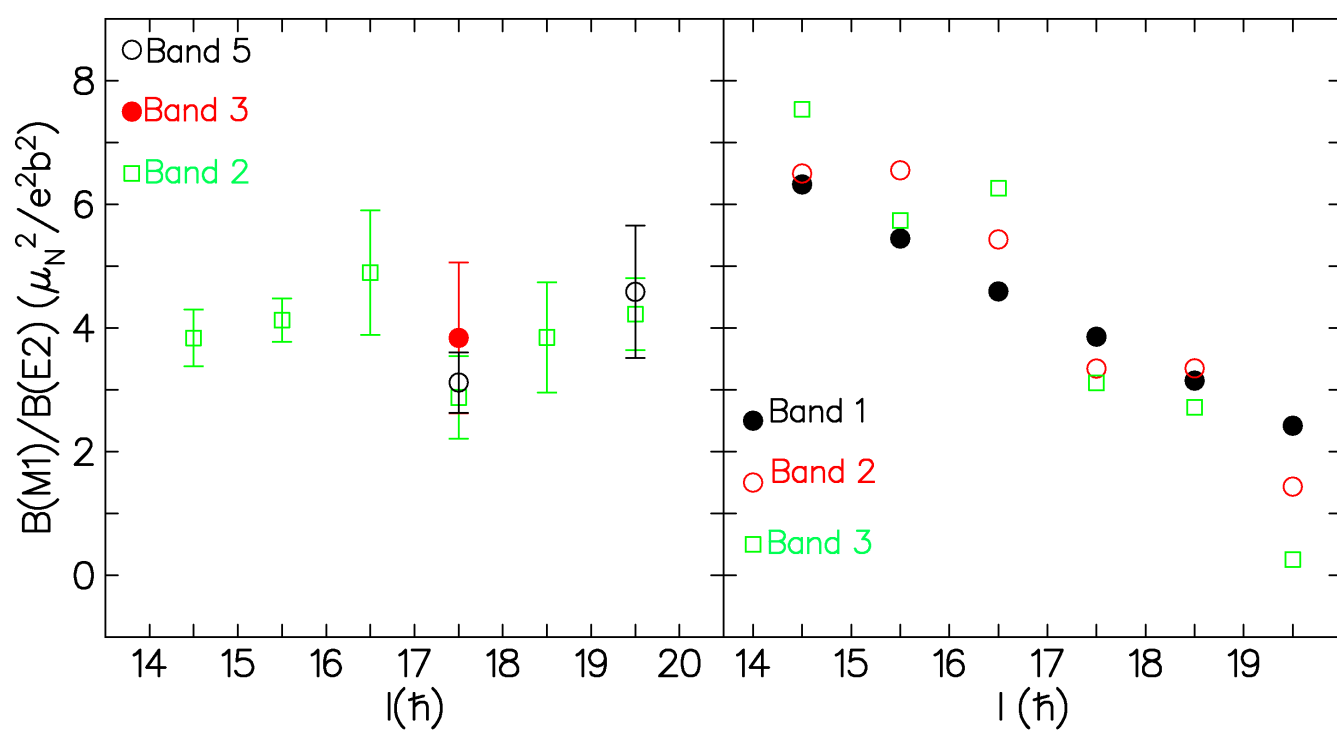


FIG. 4.27. Experimental (left panel) and theoretical (right panel) $B(M1)/B(E2)$ values of ^{193}Tl .

Apart from the excitation energies and the angular momenta, the reduced transition probability ratios $B(M1)/B(E2)$ in ^{193}Tl were calculated. The obtained $B(M1)/B(E2)$ values for the three bands are similar, as expected for chiral symmetry structure. However, in theory there is a gradual decreasing trend with spins which is different from the experimental $B(M1)/B(E2)$ values (see Fig. 4.27).

4.9 Chiral symmetry in ^{192}Tl

The yrast band (Band 1) in ^{192}Tl was associated with the $\pi h_{9/2} \otimes \nu i_{13/2}$ configuration, which is suitable for chiral symmetry. The valence proton lies in the lower part of the $\pi h_{9/2}$ subshell and the valence neutron lies in the higher part of the $i_{13/2}$ subshell. Thus, the valence proton (neutron) has particle (hole) nature as required to form an aplanar system in angular momentum space. A side band (Band 5) with the same negative parity was observed. The relative excitation energy is about 437 keV at $I = 13$ and becomes smaller at higher spins down to 263 keV at $I = 16$ (see Fig. 4.21). This band could be a chiral partner to Band 1. Indeed this pair has similarities with the bands in ^{198}Tl which were suggested as chiral candidates [131]. Theoretical calculations for these bands were performed using the CNS codes and the two-quasiparticle-plus-triaxial rotor model.

Calculations carried out for the $\pi h_{9/2} \otimes \nu i_{13/2}$ configuration in ^{192}Tl with the CNS codes show a moderately deformed ($\varepsilon_2 \sim 0.15$) shape. A local minimum with a triaxiality of $\gamma \sim -36^\circ$ was observed at the spins of 12^- and 14^- (see Fig. 4.28). This supports the existence of chiral symmetry in ^{192}Tl .

Calculations of the excitation energies and the angular momentum components were performed using the two-quasiparticle-plus-triaxial rotor model [134]. This model is relevant for 2 quasi-particle configurations. The TQPRM calculations were carried out using the codes called GAMPN, VPNDDELTA, ASYRMO and PROBAMO which are run one after the other [135]. In this work, standard parameters for the Nilsson potential [135, 136] and for the residual proton-neutron interaction (V_{pn}) were used. The proton-neutron interaction is expressed as

$$V_{pn} = \sqrt{8\pi^3} b^3 \delta(\vec{r}_p - \vec{r}_n) (u_0 - u_1 \sigma_p \cdot \sigma_n), \quad (4.2)$$

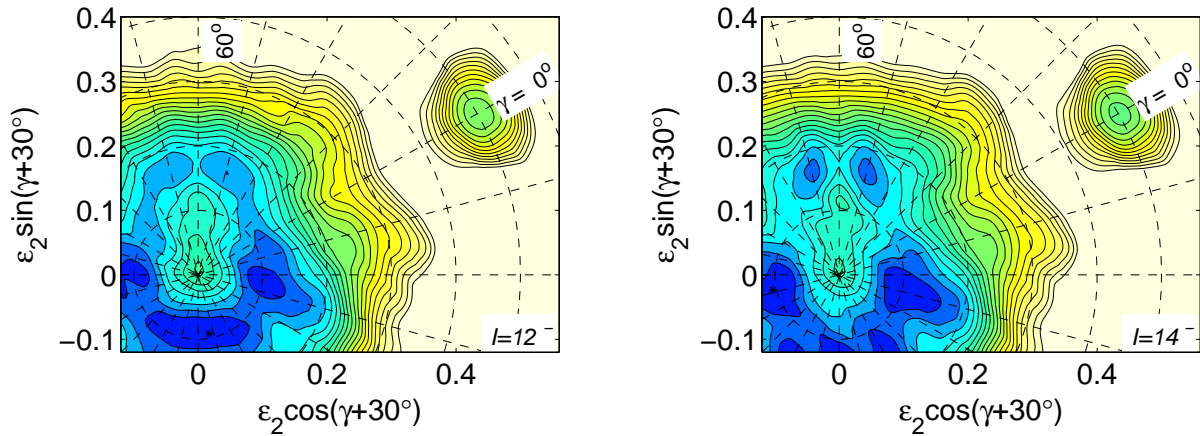


FIG. 4.28. Potential energy surface as a function of spin in ^{192}Tl illustrating the absolute minima with respect to the nuclear deformation.

where b is the oscillator length, u_0 and u_1 are the strength parameters, and σ is a Pauli spin matrix. The strength parameters for V_{pn} were set to $u_0 = -4.95$ MeV and $u_1 = -0.55$ MeV as previously used for $h_{9/2}$ proton and $i_{13/2}$ neutron in the 180 and 190 mass regions [137]. A variable moment of inertia (VMI) with Harris parameters of $J_0 = 8 \text{ MeV}^{-1} \hbar^2$ and $J_1 = 40 \text{ MeV}^{-3} \hbar^4$ were used. A quadrupole deformation $\varepsilon_2 = 0.15$ and a triaxiality parameter $\gamma \sim -36^\circ$ corresponding to the absolute minimum of the potential energy that was obtained with the CNS codes were considered. The spin g-factor g_s was taken as 70% of the spin g-factor for free nucleons, which are $g_{s,f}(p) = 5.59$ and $g_{s,f}(n) = -3.83$. The core g-factor g_R was taken as 0.3. The states in the two bands were selected based on the similarity in the distributions of the projections of the angular momenta, indicating that the states correspond to the same $\pi h_{9/2} \otimes \nu i_{13/2}$ configuration.

The calculated excitation energies of the two differ by less than 500 keV (see Fig. 4.29), but the two bands do not come closer at higher spins as observed experimentally. However, most importantly the calculated angular momenta (see Fig. 4.30 and Fig. 4.31), show an aplanar system which supports the presence of chiral symmetry in ^{192}Tl . The calculated total angular momentum of ^{192}Tl has large projections on all three nuclear axes. The angular momentum of the core has larger component along the intermediate axis, while the proton and neutron angular momenta are dominant along the short and long axes

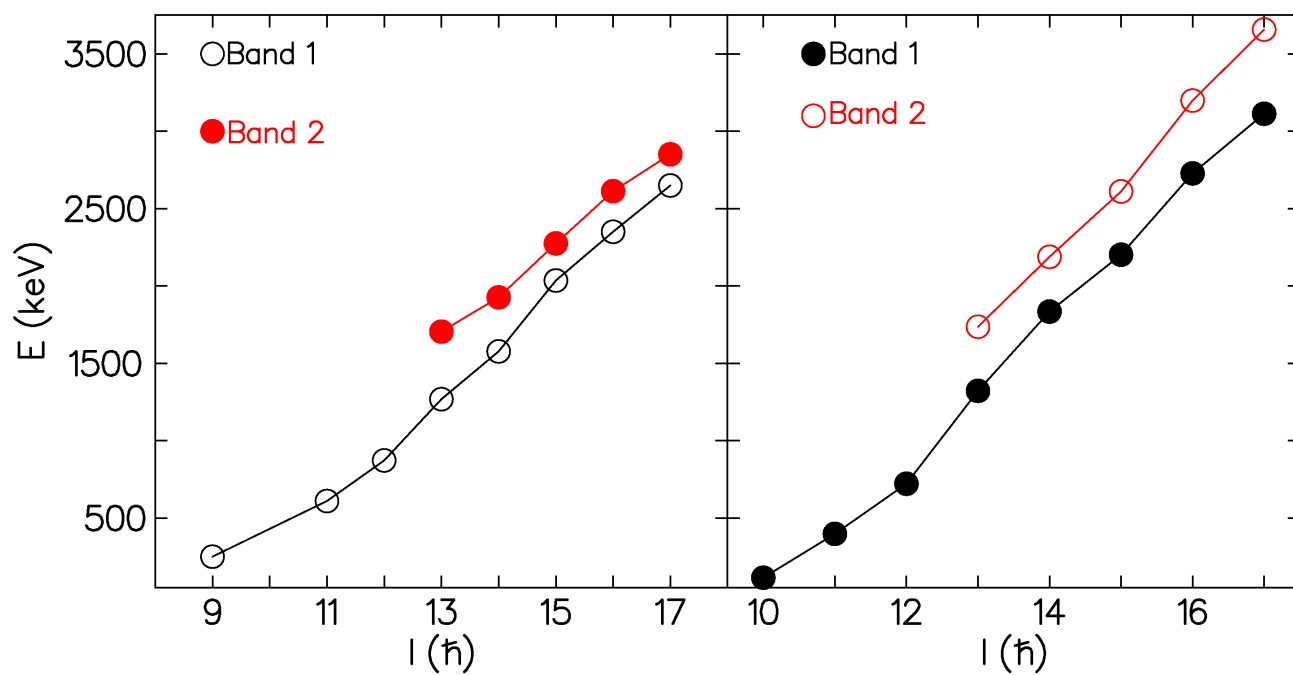


FIG. 4.29. Experimental (left panel) and theoretical (right panel) excitation energies in ^{192}Tl .

respectively. Thus, the total angular momentum is out of the planes defined by the major nuclear axes.

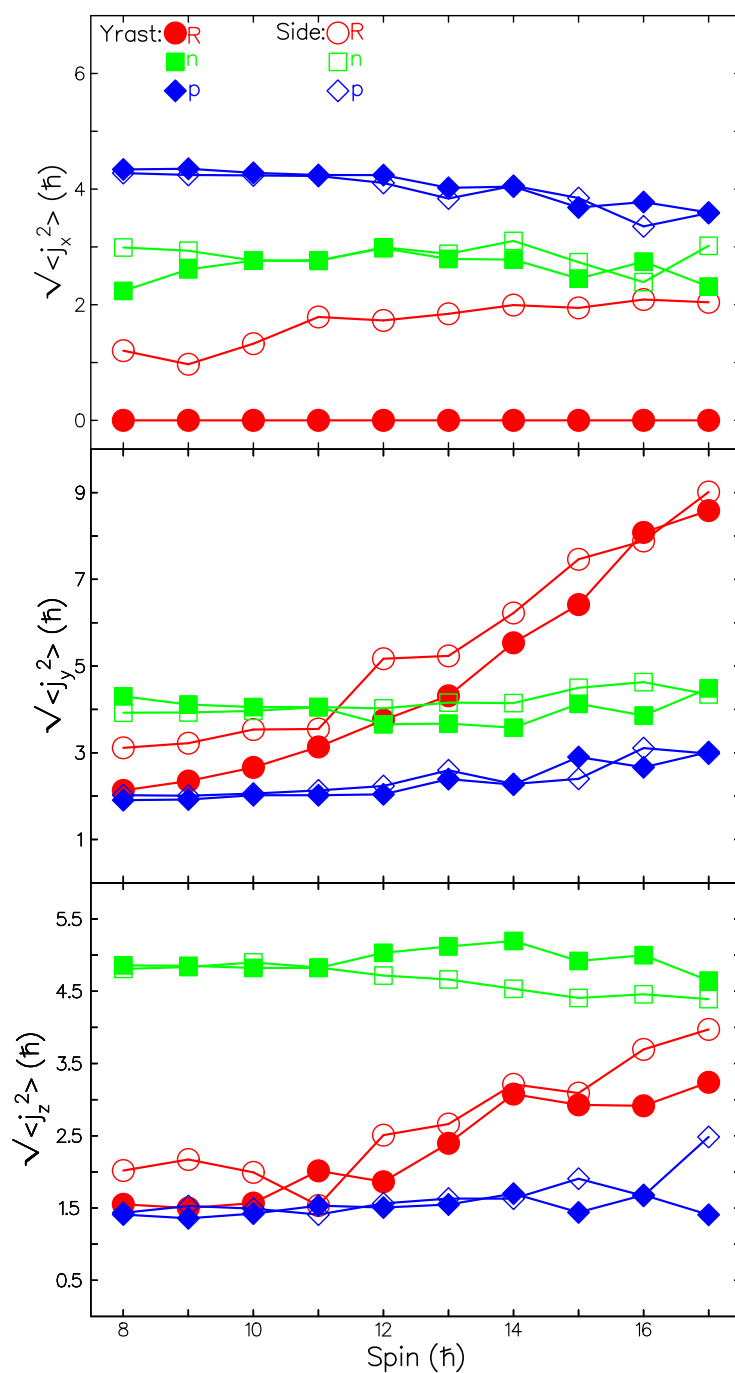


FIG. 4.30. Plot of the components for the angular momenta of the core (R), the protons (p) and the neutrons (n) in ^{192}Tl as produced with calculations using the TQPRM.

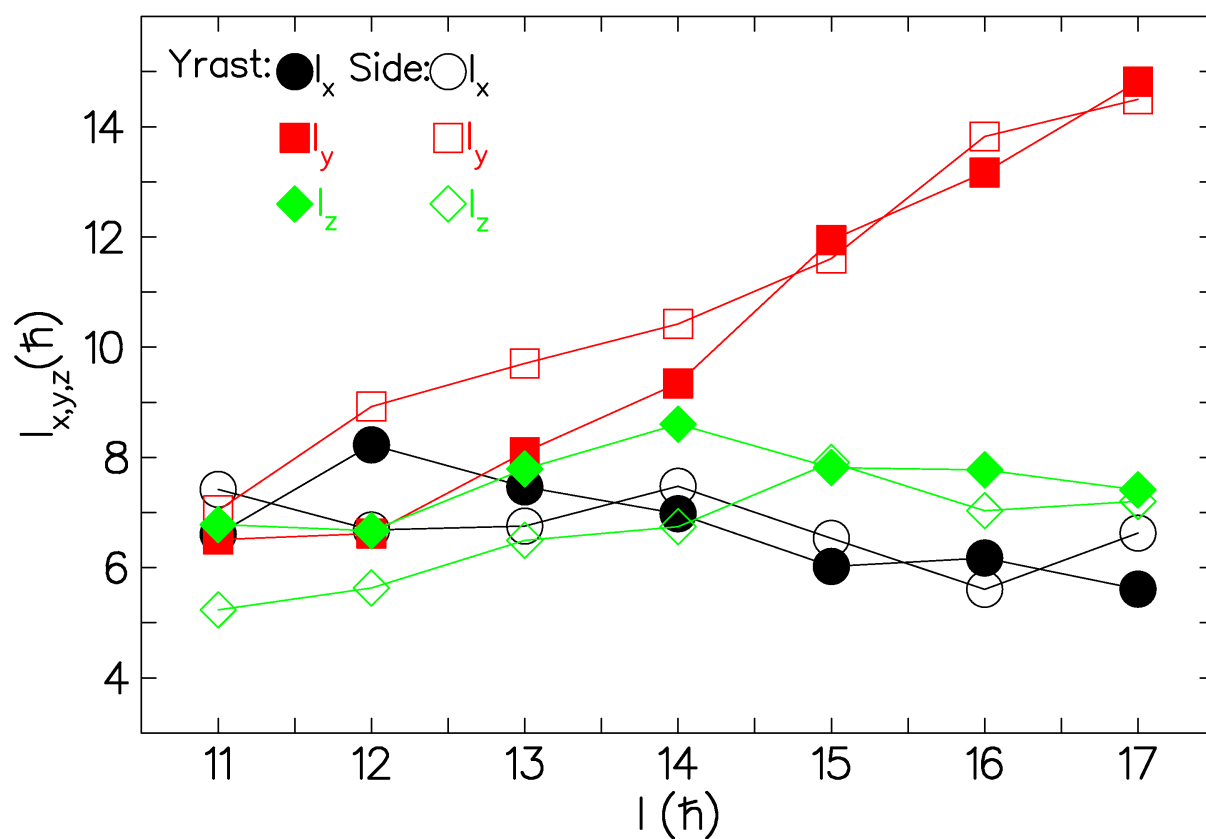


FIG. 4.31. Plot of the components for the total angular momentum in ^{192}Tl as produced with TQPRM calculations.

Chapter 5

Conclusions

γ -ray spectroscopy studies were performed in the $^{192,193}\text{Tl}$ isotopes. The previous level scheme of ^{193}Tl was considerably modified and extended. Twenty nine new transitions were added and the placement of one band and a few transitions was revised. The level scheme of ^{192}Tl was significantly extended with about 65 new transitions with respect to the previous publication [71]. Spins and parities were assigned to most of the new levels using the angular distribution ratio R_{AD} and the linear polarization anisotropy measurements. Most of the structures were described in terms of the associated nucleon configurations. Two negative parity bands in ^{192}Tl were associated with the $\pi h_{9/2} \otimes \nu i_{13/2}$ configuration and considered as candidates for chiral symmetry pair. Three negative parity bands in ^{193}Tl were associated with the $\pi h_{9/2} \otimes \nu i_{13/2}^2$ configuration. These bands show similarity in the excitation energies, and $B(M1)/B(E2)$ reduced transition probability ratios. Theoretical calculations were performed using the Cranked Nilsson-Strutinsky codes, and also the multi-particle rotor model for ^{193}Tl and the two-quasiparticle-plus-triaxial rotor model for ^{192}Tl . The observed properties of the negative parity bands and the theoretical results suggest that chiral symmetry might form in both $^{192,193}\text{Tl}$. In particular, the three negative parity bands in ^{193}Tl might represent a multiplet of chiral systems in ^{193}Tl .

It remains unclear how to pair these bands of ^{193}Tl , but independently on the exact choice, the bands show close similarity. For instance Bands 2 and 3 have relative excitation energy of 409 keV at $I = 31/2$ which decreases to 188 keV at $I = 39/2$. This can be compared with the relative excitation energy of some of the best chiral candidates to date.

Relative alignments and $\Delta B(M1)/B(E2)$ values for Bands 2 and 3 are also small and comparable with those in some of the best chiral doublet bands, which have $\Delta I \leq 2\hbar$ and $\Delta B(M1)/B(E2) \leq 6 (\mu_N^2/e^2b^2)$. The relative alignment for Bands 2 and 3 in ^{193}Tl varies between 1.3 to 2.4 \hbar , while their $B(M1)/B(E2)$ at $35/2^-$ are the same within the error bars. Close-similarity is found in Bands 2 and 5 too. The two bands get closer and cross each other. Their maximum relative excitation energy is 210 keV. Their alignments differ by about 2.5 \hbar and their $B(M1)/B(E2)$ values at $33/2^-$ and $39/2^-$ are the same within error bars. Near-degeneracy is also found in Bands 3 and 5. Their relative excitation energy varies between 147 keV and 223 keV. Their relative alignment reaches a maximum value of $\sim 2\hbar$ and becomes as small as 0.2 \hbar , while their $B(M1)/B(E2)$ values at $35/2^-$ are approximately equal within error bars. Therefore the three negative parity bands in ^{193}Tl may be classified among the best chiral doublet bands.

It is thus possible that the two chiral systems develop in ^{193}Tl , each giving rise to two partner bands. Then a question arises why a fourth negative parity band was not observed. One should note, however, that Bands 3 and 5 are weakly populated. Particularly Band 5 consists of only a few transitions and just one E2 cross over was observed. Thus if the 4th band is at a slightly higher excitation energy and thus even weaker, it is not surprising that it was not observed in our data. To search for it one probably needs a factor of 10 larger statistics. If the GAMKA array is built at iThemba LABS there will be an excellent chance to find this band.

The ^{192}Tl nucleus is another reasonably good chiral candidate. Similarities were found in two negative parity bands, Bands 1 and 5, of ^{192}Tl . Their relative excitation energy is about 437 keV at $I = 13\hbar$ and decreases at higher spins down to 263 keV at $I = 16\hbar$. Their alignments differ by about 2.5 \hbar .

Thus, the two nuclei, ^{193}Tl and ^{192}Tl , are two additional chiral candidates in the $A \sim 190$ mass region, with ^{193}Tl being among the best chiral case known to date. Furthermore it is possible that a multiplet of chiral systems develops in this nucleus.

Bibliography

- [1] J. Gal, *Helvetica Chimica Acta* **96**, 1617 (2013).
- [2] S. Frauendorf and J. Meng, *Nucl. Phys. A* **617**, 131 (1997).
- [3] S. Frauendorf, *Mod. Phys.* **73**, No. 2, 463 (2001).
- [4] W. Shouyu, *WSPC Proceedings* (2012).
- [5] P. Balabanski *et al.*, *Phys. Rev. C* **70**, 044305 (2004).
- [6] R. A. Bark *et al.*, *Nucl. Phys. A* **691**, 577 (2001).
- [7] D. J. Hartley *et al.*, *Phys. Rev. C* **64**, 031304 (2001).
- [8] A. A. Hecht *et al.*, *Phys. Rev. C* **63**, 051302 (2001).
- [9] A. A. Hecht *et al.*, *Phys. Rev. C* **68**, 054310 (2003).
- [10] P. Joshi *et al.*, *Phys. Lett. B* **595**, 135 (2004).
- [11] P. Joshi *et al.*, *J. Phys. G: Nucl. Part. Phys.* **31**, S1895 (2005).
- [12] P. Joshi *et al.*, *Eur. Phys. J. A* **24**, 23 (2005).
- [13] P. Joshi *et al.*, *Phys. Rev. Lett.* **98**, 102501 (2007).
- [14] T. Koike *et al.*, *Phys. Rev. C* **63**, 061304(R) (2001).
- [15] T. Koike *et al.*, *Phys. Rev. C* **67**, 044319 (2003).
- [16] E. A. Lawrie *et al.*, *Phys. Rev. C* **78**, 021305 (2008).

-
- [17] E. A. Lawrie *et al.*, Eur. Phys. J. A. **45**, 39 (2010).
- [18] Y. X. Luo *et al.*, Phys. Lett. B. **670**, 307 (2009).
- [19] Y. X. Luo *et al.*, Erratum Phys. Lett. B. **691**, 285 (2010).
- [20] P. L. Masiteng *et al.*, Acta Phys. Pol. B **40**, 657 (2009).
- [21] E. Mergel *et al.*, Eur. Phys. J. A **15**, 417 (2002).
- [22] C. B. Moon, T. Komatsubara, and K. Furuno, Nucl. Phys. A. **674**, 343 (2000).
- [23] C. B. Moon, T. Komatsubara, and K. Furuno, Nucl. Phys. A. **678**, 457 (2000).
- [24] C. M. Petrache *et al.*, Phys. Rev. C **65**, 054324 (2002).
- [25] C. M. Petrache *et al.*, Nucl. Phys. A **106**, 597 (1996).
- [26] G. Rainovski *et al.*, J. Phys. G: Nucl. Part. Phys. **29**, 2763 (2003).
- [27] G. Rainovski *et al.*, Phys. Rev. C **68**, 024318 (2003).
- [28] A. J. Simons *et al.*, J. Phys. G: Nucl. Part. Phys. **31**, 541 (2005).
- [29] K. Starosta *et al.*, Phys. Rev. C **65**, 044328 (2002).
- [30] J. Timar *et al.*, Phys. Lett. B **598**, 178 (2004).
- [31] J. Timar *et al.*, Phys. Rev. C **76**, 024307 (2007).
- [32] C. Vaman *et al.*, Phys. Rev. Lett. **92**, 032501 (2004).
- [33] S. Wang *et al.*, Phys. Rev. C **74**, 017302 (2006).
- [34] J. Yong-Nam *et al.*, J. Phys. G: Nucl. Part. Phys. **31**, B1 (2005).
- [35] S. Zhu *et al.*, Phys. Rev. Lett. **91**, 132501 (2003).
- [36] S. Zhu *et al.*, Eur. Phys. J. A **25**, s01, 459 (2005).
- [37] E. A. Lawrie and O. Shirinda, Phys. Lett. B **689**, 66 (2010).

-
- [38] T. Koike *et al.*, in FNS2002, Berkeley, CA, 2002, AIP Conf. Proc. edited by P. Fallon, R. Clark (AIP, Melville, NY, 2003) **No. 656**, p. 160 (2002).
- [39] C. Vaman *et al.*, Phys. Lett. **92**, 032501 (2004).
- [40] P. Joshi *et al.*, Phys. Rev. Lett. **98**, 102501 (2007).
- [41] O. Shirinda and E. A. Lawrie, Eur. Phys. J. A **48** (2012).
- [42] O. Shirinda, *PhD Thesis* (University of the Western Cape, 2011).
- [43] T. Koike, K. Starosta, and I. Hamamoto, Phys. Rev. Lett. **93**, 171502 (2004).
- [44] S. Q. Zhang *et al.*, Phys. Rev. C **75**, 44307.6 (2007).
- [45] D. Tonev *et al.*, PRL **112**, 052501 (2014).
- [46] E. Lieder *et al.*, PRL **112**, 202502 (2014).
- [47] Z. Yun *et al.*, CHIN. PHYS. LETT. **31**, 062101 (2014).
- [48] T. Suzuki *et al.*, Phys. Rev. C **78**, 031302 (2008).
- [49] E. Grodner *et al.*, Mod. Phys. E **14**, 347 (2005).
- [50] L. L. Wang *et al.*, Chin. Phys. C **33**, Supplement 1, 173 (2009).
- [51] E. Grodner *et al.*, Phys. Rev. Lett. **97**, 172501 (2006).
- [52] E. Grodner *et al.*, Int. J. Mod. Phys. E **15**, 548 (2006).
- [53] D. Tonev *et al.*, Phys. Lett. **96**, 052501 (2006).
- [54] D. Tonev *et al.*, Phys. Rev. C **76**, 044313 (2007).
- [55] S. Mukhopadhyay *et al.*, Phys. Rev. Lett. **99**, 172501 (2007).
- [56] S. Mukhopadhyay *et al.*, Phys. Rev. C **78**, 034311 (2008).
- [57] P. L. Masiteng *et al.*, Phys. Lett. B **719**, 83 (2013).
- [58] P. L. Masiteng, *PhD Thesis* (University of the Western Cape, 2014).

-
- [59] S. Wang, Y. Liu, T. Komatsubara, Y. Ma, and Y. Zhanga, *Phys. Rev. C* **74**, 017302 (2006).
- [60] T. Koike, K. Starosta, C. J. Chiara, D. B. Fossan, and D. Y. LaFosse, *Phys. Rev. C* **67**, 044319 (2003).
- [61] J. Meng *et al.*, *Phys. Rev. C* **73**, 037303 (2006).
- [62] J. Peng *et al.*, *Phys. Rev. C* **77**, 024309 (2008).
- [63] J. Yao *et al.*, *Phys. Rev. C* **79**, 067302 (2009).
- [64] J. Li *et al.*, *Phys. Rev. C* **83**, 037301 (2009).
- [65] A. Ayangeakaa *et al.*, *PRL* **110**, 172504 (2013).
- [66] I. Kuti *et al.*, *PRL* **113**, 032501 (2014).
- [67] P. L. Masiteng *et al.*, *Eur. Phys. J. A* **50**, 119 (2014).
- [68] E. A. Lawrie *et al.*, *Phys. Rev. C* **78**, 021305(R) (2008).
- [69] E. A. Lawrie *et al.*, *Eur. Phys. J. A* **45**, 39 (2010).
- [70] W. Reviol *et al.*, *Nucl. Phys. A* **548**, 331 (1992).
- [71] A. J. Kreiner *et al.*, *Phys. Rev. C* **21**, 3 (1980).
- [72] J. Ndayishimye *et al.*, SAIP2013 Conf. Proc., **P. 302** (2013).
- [73] J. Easton, *MSc Thesis* (University of Western Cape, 2011).
- [74] A. Bohr *et al.*, *Vid. Selsk.* **26**, 14 (1952).
- [75] A. Bohr *et al.*, *Vid. Selsk.* **27**, 16 (1953).
- [76] A. Faessler and W. Greiner, *Z. Phys.* **168**, 425 (1962).
- [77] A. Faessler and W. Greiner, *Nucl. Phys.* **59**, 177 (1964).
- [78] A. Faessler, W. Greiner, and R. K. Sheline, *Nucl. Phys.* **80**, 417 (1965).
- [79] A. Faessler, W. Greiner, and R. K. Sheline, *Nucl. Phys.* **62**, 241 (1965).

-
- [80] A. Faessler, W. Greiner, and R. K. Sheline, Nucl. Phys. **70**, 33 (1965).
- [81] D. L. Hill and J. A. Wheeler, Phys. Rev. **89**, 1102 (1953).
- [82] G. Anderson *et al.*, Nucl. Phys. **A268**, 205 (1976).
- [83] S. Nilsson, Phys. Rev. **99**, 1615 (1955).
- [84] S. Nilsson, Mat. Fys. Medd. Dan. Vid. Selsk **29**, 16 (1955).
- [85] A. Bohr and B. Mottelson, *Nuclear Structure, Volume 2: Nuclear Deformations* (World Scientific, London, 1975).
- [86] D. R. Inglis, Phys. Rev. **96**, 1059 (1954).
- [87] D. R. Inglis, Phys. Rev. **97**, 701 (1955).
- [88] I. Ragnarsson and S. G. Nilsson, *Shapes and Shells in Nuclear Structure* (Lunds University, Sweden, 2005).
- [89] A. Bohr and B. Mottelson, *Nuclear Structure, Vol. II* (Benjamin, Reading, MA, 1975).
- [90] S. Harris, Phys. Rev. **138**, B509 (1965).
- [91] T. Bengts-Son and I. Ragnarsson, Nucl. Phys. A. **436**, 14 (1985).
- [92] B. G. Carlsson and I. Ragnarsson, Phys. Rev. C. **74**, 011302(R) (2006).
- [93] I. Ragnarsson and B. G. Carlsson, CNS Manual (2010).
- [94] A. Bohr and B. Mottelson, Nuclear Structure **Vol. 2**, 9 (1975).
- [95] S. G. Nilsson and I. Ragnarsson, *Shapes and shells in nuclear structure* (Cambridge Univ. Press, 26, 1995).
- [96] Z. Szymanski, *Fast Nuclear Rotation* (Clarendon Press, Oxford, 26, 1983).
- [97] B. G. Carlsson and I. Ragnarsson, Phys. Rev. C **74**, 044310 (2006).
- [98] R. Bock, *Heavy Ion Collisions, Volume 2* (North Holland Publishing Company, 1980).

-
- [99] *GammaSphere Online Booklet*, ([nucalf.Physics.fsu.edu/riley/gamma/](http://nucalf.physics.fsu.edu/riley/gamma/)) .
- [100] P. Regan, *Post Graduate Nuclear Experimental Techniques (4NET) Course Notes* (Guildford, GU2 7XH, UK, 2003).
- [101] A. Gavron, Phys. Rev. C **21**, 230 (1979).
- [102] J. H. Hubbel and S. M. Seltzer, *Attenuation of photons* (Physical Measurements Laboratory, 1996).
- [103] P. A. Pipidis, *PhD Thesis* (Florida State University, 2006).
- [104] S. Krane, *Introductory Nuclear Physics* (John Wiley and Sons, 1988).
- [105] H. Kramer *et al.*, IEEE Trans. Nucl. Sc. **22**, 149 (1975).
- [106] P. M. Jones *et al.*, Nucl. Instr. and Meth. in Phys. Res. A **362**, 556 (1995).
- [107] W. H. Trzaska, Nucl. Instr. and Meth. in Phys. Res. A **223**, 230 (1990).
- [108] *EXO GAM detectors* (<http://pro.ganil-spiral2.eu/laboratory/detectors/exogam/exogam-detectorstern> Cape, 2006, page 30 and 40 fig 70, 2006).
- [109] C. Beausang *et al.*, Nucl. Instr. and Meth. A **313**, 37 (1992).
- [110] R. Newman *et al.*, Proceeding of Balkan School on Nucl. Phys. (1998).
- [111] J. L. Conradie, *PhD Thesis* (University of Stellenbosch, 1992).
- [112] *Application Note AN2508. CAEN Digital Pulse Height Analyser, a digital approach to Radiation Spectroscopy* (www.caen.it, 2011).
- [113] W. Leo, Springer-Verlag Berlin Heidelberg, **P. 62** (1987, 1994).
- [114] *Pulse processing and analyses* (http://www.dnp.fmph.uniba.sk/~kollar/je_w/el3.htm#6).
- [115] *PIXIE-16 Manuals, version 1.40* (<http://www.xia.com>, 2009).
- [116] R. Grzywacz, Nucl. Instr. and Meth. B **204**, 649 (2003).
- [117] D. Radford, Nucl. Instr. and Meth. A **361**, 297 (1995).

-
- [118] G. Duchêne *et al.*, Nucl. Inst. and Meth. A **432**, 90 (1999).
- [119] N. Drakos, *Studies of excited nuclear states by using the $\gamma - \gamma$ coincidence technique* (<http://www.nuclear.kth.se/courses/lab/latex/gammagamma/gammagamma.html>, 1996).
- [120] T. Yamazaki, Nuclear Data, Section A **3**, 1 (1967).
- [121] T. Kibédi *et al.*, Nucl. Instr. and Meth. A **589**, 202 (2008).
- [122] M. Emeric and A. Sonzogni, *NNDC* (Brookhaven National Laboratory).
- [123] R. S. Hager and E. C. Seltzer, Nucl. Data Tables **A4**, 1 (1968).
- [124] E. Gueorguieva *et al.*, Phys. Res. A **474**, 132 (2001).
- [125] E. Gueorguieva *et al.*, iThemba LABS Annual Report (2003).
- [126] F. Newton *et al.*, Nucl. Phys. A **236**, 225 (1974).
- [127] W. R. Leo, *Techniques for Nuclear and Particle Physics Experiments*, P. 96 (Springer-Verlag, 1992).
- [128] R. M. Diamond and F. S. Stephens, Nucl. Phys. **45**, 632 (1963).
- [129] X. Chengying *et al.*, Science in China Ser. G Physics, Mechanics and Astronomy **48**, 442 (2005).
- [130] A. J. Kreiner *et al.*, Nucl. Phys. A **308**, 147 (1978).
- [131] E. A. Lawrie *et al.*, Acta Physica Polonica B **38**, 4 (2007).
- [132] H. Hübel *et al.*, Nucl. Phys. A **453**, 316 (1986).
- [133] S. Slem *et al.*, Phys. Rev. C **70**, 014303 (2004).
- [134] P. Semmes and I. Ragnarsson, AIP Conf. Proc. **259**, P. 566 (1992).
- [135] S. G. Nilsson, Nucl. Phys. A **436**, 14 (1985).
- [136] T. Bengtsson and I. Ragnarsson, Nucl. Phys. A **436**, 14 (1985).
- [137] R. A. Bark *et al.*, Phys. Lett. B **406**, 193 (1997).